

UNIVERSITY OF OKLAHOMA

GRADUATE COLLEGE

APPLICATION OF PASSIVE SEISMIC INTERFEROMETRY
FOR LOCAL AND SHALLOW IMAGING

A DISSERTATION

SUBMITTED TO THE GRADUATE FACULTY

in partial fulfillment of the requirements for the

Degree of

DOCTOR OF PHILOSOPHY

by

DEEPANKAR SATYAVRAT DANGWAL

Norman, Oklahoma

2023

APPLICATION OF PASSIVE SEISMIC INTERFEROMETRY

FOR LOCAL AND SHALLOW IMAGING

A DISSERTATION APPROVED FOR THE

SCHOOL OF GEOSCIENCES

BY THE COMMITTEE CONSISTING OF

Dr. Junle Jiang, Chair

Dr. Xiaowei Chen, Co-Chair

Dr. Deepak Devegowda

Dr. Heather Bedle

Dr. Michael Behm

Chapter 2 was previously published as:

Deepankar, D., & Behm, M. (2021). Interferometric body-wave retrieval from ambient noise after polarization filtering: Application to shallow reflectivity imaging. *Geophysics*, 86(6), Q47–Q58. <https://doi.org/10.1190/geo2020-0768.1> ©

Society of Exploration Geophysicists 2021

All other content © Copyright by DEEPANKAR DANGWAL 2023

All rights reserved.

TABLE OF CONTENTS

Table of Contents	iv
List of Figures	viii
Acknowledgements	xxi
Abstract of the dissertation	xxiii
1 Introduction	1
1.1 Seismic interferometry	1
1.2 Passive seismic interferometric workflow and assumptions ...	2
1.3 Local scale applications of interferometry	7
1.4 Overview of the dissertation	9
1.5 Structure of the dissertation	11
Bibliography	13
2 Interferometric body-wave retrieval from ambient noise after polarization filtering: application to shallow reflectivity imaging	20
2.1 Abstract	20
2.2 Introduction	21
2.3 Study area and data	24
2.4 Methods	30

2.4.1 Data pre-selection using an existing earthquake catalog	30
2.4.2 Data pre-selection using polarization filtering	31
2.4.3 Pre-processing	36
2.4.4 Autocorrelation (AC)	37
2.5 Results and discussion	38
2.6 Conclusions	51
2.7 Appendix	53
2.7.1 Kinematics of AC applied to sub-vertical incident source data	53
Bibliography	58
3 Passive reflectivity imaging and near-surface Vp/Vs ratio estimation after S-wave polarization filtering	67
3.1 Abstract	67
3.2 Introduction	68
3.3 Study area and data	71
3.4 Method	73
3.4.1 S-wave preselection using polarization filtering	73
3.4.2 Preprocessing and autocorrelation	78
3.5 Results and discussion	78
3.5.1 Polarity of S-wave reflection retrieved by AC	78

3.5.2 Interpretation of structural reflections	82
3.5.3 P-reflectivity and Vp/Vs estimation	88
3.6 Conclusions	90
Bibliography	92
4 Imaging a paleovalley with passive seismic methods: Evidence for glacial carving of Unaweep Canyon (Colorado, US)	100
4.1 Abstract	100
4.2 Introduction	101
4.3 Geologic setting	102
4.4 Deployment and Data	105
4.5 Methods	106
4.5.1 Teleseismic AC	106
4.5.2 Ambient noise seismic interferometry (SI) and 2D Vs Inversion	110
4.6 Results and Discussion	115
4.7 Conclusions	119
4.8 Supplementary materials.....	120
4.8.1 Introduction	120
Bibliography	123

5	High-resolution imaging of the shallow subsurface and relationship with site responses using co-located Nodal and DAS arrays near Enid, Oklahoma	133
5.1	Abstract	133
5.2	Introduction	134
5.3	Data	137
5.4	Methods	140
5.4.1	Ambient noise interferometry	140
5.4.2	H/V spectral analysis	144
5.5	Result and discussions	145
5.5.1	Near-surface structural mode	145
5.5.2	Site amplification correlated with sub-surface structure	147
5.6	Conclusions	150
	Bibliography	152
6	Conclusions	161
6.1	Summary of results	162
6.2	Future work	163

LIST OF FIGURES

- Figure 1.1: (a) Sources S and S' generating rightward and leftward 3
propagating uncorrelated noise x_S and $x_{S'}$. (b) x_A is the
noise recorded at receiver A. (c) x_B is the noise recorded
at receiver B. (d) Crosscorrelation $x_B(t) \otimes x_A(t)$ of the
noise recording. The illustration is modified from
Wapenaar et al., 2010a.
- Figure 1.2: EGF retrieved by global interferometry showing Rayleigh 6
wave and other body wave phases (modified from Haned
et al., 2016)
- Figure 2.1: Map of Wellington field with local seismic array (white 26
circles) and drilled well KGS 2-32 (gray circles). White
box marks the extent of available active seismic data, with
an inline and a crossline passing through the well location
shown in Figure 10. Inset shows the location of
Wellington in the continental USA
- Figure 2.2: Map of Oklahoma (a) showing earthquake events (black 28
dots) from a regional seismic catalog
(<https://www.ou.edu/ogs/research/earthquakes/catalogs>)
for the recording period (2014 – 2018). Concentric circles

represent distance from Wellington array in kilometers.

Histograms of hypocentral parameters: depth (b), epicentral distance from array (c) and azimuth of epicenter in relation to array (d).

Figure 2.3: Vertical component beamforming analysis for ambient noise dataset event (a – d) and a catalog dataset event (e – h) extracted from the same ambient noise event. Each polar plot represents beamforming power (maximum: red, minimum: blue) and its apparent velocity (radial axis in km/s) and back azimuth at unique frequencies. 29

Figure 2.4: Application of polarization filtering to 3C ambient noise dataset recording during a) a local earthquake event also listed in the catalog. Origin time: 11/15/2015 09:45:31, Depth: 5.1 km, Magnitude: 4, Epicentral distance: 150 km, Azimuth: 231.75°. b) An event not listed in the regional catalog. Dashed box represents the trough feature corresponding to sharp decline of incidence angle (between direction of maximum polarization and vertical) of P-wave energy. Dotted line represents a local maximum in linearity corresponding to P-wave arrival. The first solid line indicates P-wave first arrivals based on 35

incidence trough and linearity maximum features that are used to extract a P-wave dominant event. The second solid line indicates S-wave first arrival based on a STA/LTA picker.

Figure 2.5: Flowchart summarizing data pre-selection methodologies 38 applied to the ambient noise dataset to create the catalog and polarization datasets, and subsequent implementation of single-station (AC) and station-pair (CC; crosscoherence) interferometry.

Figure 2.6: Comparison of vertical component interferometry for 40 ambient noise dataset (a – c), catalog dataset (d – f) and polarization dataset (g – i) band passed in different frequency bands: 5 – 10 Hz (a, d, g), 1 – 10 Hz (b, e, h), 1 – 5 Hz (c, f, i). Overlaid are linear moveouts of 1500 m/s (dashed line) and 6500 m/s (solid line). Hyperbolic moveouts in (a, d, g) are calculated for a velocity of 3700 m/s and depths ranging from LeCompton to Kansas City formations.

Figure 2.7: Comparison of vertical component AC stacks for ambient 41 noise dataset (a – c), catalog dataset (d – f) and polarization dataset (g – i) band passed in different

frequency bands: 5 – 10 Hz (a, d, g), 1 – 10 Hz (b, e, h), 1 – 5 Hz (c, f, i)

Figure 2.8: Comparison of Z component (a – c), North-South component (d – f) and East-West component (g – i) polarization dataset AC stacks band passed in different frequency bands: 5 – 10 Hz (a, d, g), 1 – 10 Hz (b, e, h), 1 – 5 Hz (c, f, i). 43

Figure 2.9: Synthetic modeling of waveforms (horizontal (H) and vertical (Z) components) for events in 120 and 190 km distance, respectively, after passing basement and a low-velocity sedimentary layer of 1 km thickness. P: direct P-wave; Ps: S-wave converted from P-wave impinging on the sediment-basement boundary. PpP: free-surface multiple. Note the projection of P-wave amplitudes at the horizontal component and of S-wave amplitudes at the vertical component, and the variation in PpP arrival times due to the varying epicentral distance. 45

Figure 2.10: Comparison of time-lapse vertical component AC stacks for ambient noise dataset (a, b), catalog dataset (c, d) and polarization dataset (f, g) band passed in 5 – 10 Hz range for stations 03 (a, c, f) and 11 (b, d, g). (e) Variation of 47

number of earthquakes (blue) and median epicentral distance (red, km) for catalog dataset. (h) Variation of number of selected events (blue) and median incidence angle at the array (green, °) for the polarization dataset.

Figure 2.11: Comparison of well log and well log derived data with AC stack and active seismic stacks. Well log data includes (a) bulk density log, (b) sonic log from KGS 2-32 well. Derived well log data includes (c) acoustic impedance, (d) acoustic reflectivity and synthetic traces using (e) 5 Hz Ricker wavelet and (f) 10 Hz Ricker wavelet. Polarization AC stack (g) is band passed in 5 – 10 Hz range and eigenimage reconstructed using top 20% eigenvalues. Active-seismic data used for comparison along (h) IL 43 and (i) XL 32 (Figure 2.1). 50

Figure A2.12: (a) Direct P ray paths and (b) surface incidence angles at epicentral range 100 – 290 km for a sub-basement source at 5 km depth. (c) Vp model showing sedimentary-basement interface at 1 km depth, (d) ray paths for P, PpP, Ps phases arriving at epicentral distances 100 km, 200 km, 290 km (black inverted triangles). 54

Figure A2.13: (a) Depth to TWT converted velocity model showing the 55
sedimentary-basement interface. (b) Polarity reversed
synthetic traces at epicentral distances 100 – 290 km and
their corresponding (c) polarity reversed AC. Stacks
represent the mean trace. Annotated P, Ps, PpP arrival
times are the mean arrival times for each phase over the
epicenter range.

Figure 3.1: (a) Map of Oklahoma showing earthquake events 72
(colored by hypocentral depth) from a regional seismic
catalog for the recording period (2014 – 2018).
Concentric circles represent distance in kilometers from
the Wellington oil field. (b) Map of with the local seismic
stations (white triangles) used in this study and drilled
wells KGS 2-32 and KG 1-28 (red circles).

Figure 3.2: An example of S-wave polarization filtering applied to (a 77
– c) 3C recordings. (d) Calculated polarization-incidence
angles for the three eigen vectors. (e) Spectrogram of the
seismic recording overlaid with the computed S-wave
metric parameter discussed in Method section. Gray lines
represent the time window selected by STA/LTA applied
to the S-wave metric.

- Figure 3.3: (a) A two layer Vs model with an impedance boundary at 1 km depth. S-wave raypaths showing direct arriving (S) and free surface reflection (SbS) phases. 79
- Figure 3.4: (a) The two layer Vs model shown in Figure 3 down to 50 km depth. (b) Direct S-wave raypaths emanating from a sub-basement source (red star). (c) Calculated raypath incidence angles for the direct S-wave arrivals at epicentral distances 100 – 290 km. 81
- Figure 3.5: Complex reflectivity computed from Zoeppritz equations for a P-wave reflection at (a) the free surface and at (b) an impedance boundary in a 2-layer model. Similarly for an S-wave at (a) the free surface and at (b) an impedance boundary. Solid lines (blue, red) represent the magnitude (modulus) of the complex reflection coefficient. Dashed lines (blue, red) represent the phase of the complex reflection coefficient. 82

Figure 3.6: Comparison of the AC stacks computed from the (a – c) 84
ambient noise dataset and the (d – f) S-wave preselection
dataset at all three components.

Figure 3.7: (a) sonic log, (b) shear-wave log, (c) computed elastic 87
impedance log from KGS 1-32 well. Well logs are
compared with AC stacks computed from S-wave
preselection dataset. AC stacks are band passed in 1 – 5
Hz and eigenimage reconstructed to enhance lateral
continuity of retrieved phases on (d) vertical component,
(e) north-south component, (f) east-west component.

Figure 3.8: V_p/V_s estimated at all station using the KC-top using the 90
S-wave reflection time retrieved on (a) Z-component, (b)
N-component, (c) E-component AC stacks. Uncertainties
in the V_p/V_s estimates are shown by error bars. Solid red
line represents the average V_p/V_s for all stations. (d)
Comparison of well log derived V_p/V_s ratio (black) and
the average V_p/V_s ratio estimated on the N-component
(red). Dotted red lines represent the minimum and
maximum error bounds of the estimate.

- Figure 4.1: (a) Digital elevation model of Unaweep Canyon with overlaid geological map. Inset on the top-right shows the location of Unaweep Canyon on the Uncompahgre Plateau and Colorado Plateau. Box with dotted edges shows the location of Figure 4.1b. (b) Satellite map of the study area with elevation contours. Green line indicates the active seismic profile (2017). Blue line indicates the passive seismic profile (2020). Cyan crosses mark the location of wells - UDR-1A (2022), Massey (2004 – 2006). Red dashed line is the approximately mapped interface of the basement outcrop and the sedimentary fill. The three stars along the passive profile give the location of the virtual source gathers shown in Figure 4.3. 103
- Figure 4.2: (a-c) Individual AC response of 3 teleseismic events. (d) Stacked AC response of 10-teleseismic events used in the study. No post-AC signal processing has been applied. 109
- Figure 4.3: (a-c) F-K filtered VSGs with virtual sources located at 3 receiver locations marked with the same-colored stars in Figure 4.1b. (d-f) Stacked Rayleigh wave dispersion curves for bin locations corresponding to the same 3 receiver locations. 113

Figure 4.4: (a) Time-to-depth converted AC stack overlaid with V_s 114
model obtained from inversion of Rayleigh wave
dispersion curves. (b) Time-to-depth converted PSTM
active seismic stack overlaid with V_s model inverted from
Rayleigh waves recorded during active seismic
acquisition. Dashed green line: Interpreted sedimentary-
basement interface. Solid black line: Trajectory of UDR-
1A well. Solid purple line: Intersection of the N-S active
profile and the W-E passive profile. Cyan cross: Elevation
at which basement interface is interpreted from UDR-1A
cores and logs.

Figure S4.5: Time-to-depth converted PSTM stack of active seismic 121
profile acquired in 2017 (Patterson et al., 2021). Inset
shows the depth-aligned borehole P-wave sonic log from
well UDR-1A well that is integrated into the velocity
model used for time-to-depth conversion. Above the start
of the log (elevation 1715 m), the velocity model is based
on geologic well information and tomographic velocity
models (Behm et al. 2019). Red dashed line: Interpreted
basement interface. Solid black line: Well trajectory.
Cyan cross: basement top elevation interpreted from well

cores and logs. Purple line: Intersection of the active and passive seismic profiles.

- Figure S4.6: (a) Location of 10 teleseismic events used in this study. 121
(b) 3-component spectrograms and waveforms for a 6.8 magnitude event. Origin time 2020/09/01 04:09:28 UTC. Latitude: 27.97 S; Longitude: 71.30 W. Red dashed line: P-wave first arrival time. Green dashed line: 50 s time segments selected for coda wave autocorrelation.
- Figure S4.7: AC stack of ballistic teleseismic P-waves. The stack has 122
been low passed at 2 Hz and is normalized for display.
- Figure S4.8: (a-c) Raw full-offset virtual source gathers at 3 receiver 122
locations marked with the same-colored stars in Figure 4.1b.
- Figure 5.1: (a) Map of Oklahoma showing earthquake epicenters 138
(red) and faults (green). Inset shows the location of Oklahoma (black edges) in the continental United States. White box indicates the location on Figure 5.1b. (b) Map showing the Enid deployment consisting of nodes (red and blue triangles) and DAS optical fiber (magenta and cyan lines).

- Figure 5.2: (a) Map view of the overlapping eastern node and DAS 140
 deployments. Blue and yellow star indicates the location
 of node 4001 and 4017 respectively. Comparison of (b)
 north component, (c) east component node recordings and
 (d) DAS recordings for the M2.3 local earthquake.
- Figure 5.3: Comparison of (a, b) node and (c, d) DAS VSGs for 143
 virtual sources at (a) node 4001 and co-located (c) DAS
 channel 662. Similarly (b) node 4017 and co-located (d)
 DAS channel 5262. The locations are indicated with blue
 and yellow stars in Figure 5.2.
- Figure 5.4: Horizontal-to-vertical spectral ratio (HVSr) calculated 145
 for the nodal array
- Figure 5.5: Vs model obtained from inversion of Rayleigh wave 147
 dispersion curves. The same Vs model showing the (a)
 upper 100 m and (b) upper 30 m. In Figure 5.5b, the
 wiggle plot is the depth-converted HVSr.
- Figure 5.6: (a) Map view of the deployments (refer Figure 5.2a) 150
 overlaid with surface geology map (USGS; Heran et al.,
 2003). Qt: Quaternary Terrace Deposits; Pk: Permian
 Kingsman Siltstone; Pfa: Permian Fairmont Shale; Pg:
 Permian Garber Sandstone. (b) Plot showing the variation

of Vs30 (red), frequency-to-depth converted HVSR peak (black), and DAS site amplification (blue) along the profile.

Acknowledgements

Graduate student life can be an intimidating and grueling journey. This journey could not have been possible without the amazing people who were the source of positivity and strength when I most needed it.

I would first like to thank my advisor, Dr. Michael Behm, for accepting me as PhD student and for his guidance throughout this journey. Weekly meetings with him across geographies and time-zones have been a constant in my life during the last 5 years. I am grateful for his patient advising style and a stress-free environment to conduct research at my own pace. Working with him, I had opportunities to participate in several field campaigns that exposed me to multiple geophysical methods beyond the focus of my research work. Such opportunities have helped me gain experience in the complete geophysical process (from planning to interpretation).

I would like to extend my gratitude to Dr. Xiaowei Chen, for co-advising my research during the last 3 years. Handling multiple projects in parallel has always been challenging for me. I am thankful for her encouragement and patience while I worked on three separate projects during this period. While working with Dr. Chen, I visited the Seismological Laboratory at Caltech for a semester to work on the distributed acoustic sensing method. I am grateful for this opportunity to

work on an upcoming technology at one of the best research institutions in the country.

My sincere thanks to the members of my advisory committee - Dr. Junle Jiang, Dr. Heather Bedle and Dr. Deepak Devegowda for their comments and suggestions which helped in structuring and improving this dissertation. I thank Dr. Gerilyn Soreghan for her enthusiasm and insightful discussions during our interactions on the UnawEEP project. The research presented here was funded by the McCoy Research Fund and the National Science Foundation for which I am deeply grateful.

I am grateful for the friends I made at the department – Alex, Collin, Folarin, Pamela, Pranshu, Raymond, Yan, and Zhuobo – who made life more enjoyable both inside and outside the department. I was lucky to have the most wonderful housemates – Ashutosh, Autumn, Nachiket, and Sanchay – who made Norman feel like home, especially during the pandemic isolation. A special thanks to my old friends – Chinmoy, Dhruv, Dishant, Nandish and Ujjwal – for being my counselors, and confidants.

I express my deepest gratitude to my parents and family for their ceaseless love and support that has always inspired me. I thank Shipra, for her patience and for showing me kindness and love. Lastly, I dedicate this work to my grandparents who left us before they could see me graduate.

Abstract of the dissertation

Exploratory imaging of the shallow crust is motivated by – (i) the presence of exploitable natural resources, (ii) its influence on seismicity and associated hazards, and (iii) the insights it can provide into the evolution of geological landforms. Keeping in mind these motivations, I use passive seismic interferometry to image the shallow crustal structures. Conventional exploration seismology focuses on local scale imaging using active-source methods (e.g., dynamite, air guns, vibro-seis). In contrast, passive seismic interferometry offers the possibility to use universally available noise sources (both natural and anthropogenic) for subsurface imaging. This approach does not require a spatially and temporally confined seismic source and is thus a cost-effective alternative in logistically challenging environments (e.g., polar ice sheets, exo-planets, etc.). Further, the use of ambient noise as a seismic source minimizes the adverse environmental impact of explosive source experiments in sensitive ecological zones.

Ambient noise methods generally utilize low-frequency diffuse noise fields (e.g., microseisms) for global scale imaging of deep earth structures. Application of these methods at shallow scales is challenged by the scarcity of high-frequency ambient noise sources in local settings. Areas away from anthropological activity have very weak noise sources of sufficiently high frequencies. Although, in urban environments some high-frequency sources are available (e.g., traffic, industrial

noise), but these are usually confined to a narrow azimuth. Moreover, local noise sources predominantly produce surface waves which have limited vertical and horizontal resolution to be able to image the shallow subsurface.

In this dissertation, I focus on the applications of passive seismic interferometry for high-resolution imaging of the shallow subsurface (<1 km depth) by attempting to overcome the challenges and limitations mentioned above. Three diverse application scenarios are presented to demonstrate the versatility of the interferometric methods. These include – (i) Passive P- and S-wave reflectivity imaging in an oil field (Wellington, Kansas) setting using reservoir monitoring data; (ii) Passive seismic imaging of a buried alpine valley (Unaweep, Colorado) to test the hypothesis of Paleozoic glaciation; (iii) Passive seismic imaging for seismic hazard assessment in an urban environment (Enid, Oklahoma).

Reflectivity imaging using passive seismic interferometry is generally challenged by the dominance of surface-waves in ambient noise recordings. To overcome this limitation, I develop and implement single-station polarization filters to automatically extract body waves (P- and S-waves) from continuous ambient noise. The extracted waves are then subjected to interferometric processing to retrieve subsurface reflections. This methodology is suitable for sparse and irregular seismic networks such as the previously mentioned reservoir monitoring

array. In another application, similar results are achieved by using a teleseismic catalog to extract the P-wave coda.

Road-side deployments in the alpine valley and the urban environment mentioned above make linear array geometry feasible. I take advantage of the linear geometry to interferometrically retrieve surface waves propagating along the array which are then inverted to obtain a shear-velocity profile. I compliment the shear-velocity models with results from other passive seismic methods – e.g., structural reflectivity from teleseismic coda-wave autocorrelation, or layer thickness from horizontal-to-vertical spectral ratio analysis.

The main results presented in this dissertation includes the retrieval of shallow (< 1 km) structural reflections and the estimation of seismic speed ratio (V_p/V_s) at the Wellington Oil field. This is significant since very few studies have reported the retrieval of S-wave reflectivity using passive seismic methods. In the Unaweep canyon, I image the buried valley floor. The undulating sedimentary-basement interface revealed by the passive imaging suggests the glacial genesis of the canyon. In the Enid study, the high lateral resolution near surface model is well correlated with the site amplification data derived from distributed acoustic sensing. In an urban environment, such experiments are relevant for town-planning and can be used to assess the seismic hazard at sub-kilometer scales.

Chapter 1

Introduction

1.1 Seismic interferometry

The objective of seismic interferometry is to obtain the empirical Green's function (EGF) response by computing the cross-correlation (or cross-coherency) of the recordings at a pair of receivers. The EGF defines the wave propagation at one of the receivers in response to a virtual source at the other receiver location. Although the feasibility of interferometry to derive geological information has been known for over half a century (Aki, 1957; Claerbout, 1968), several researchers have contributed to its development in the early 2000s (e.g., Lobkis and Weaver, 2001; Campillo and Paul, 2003; Schuster et al., 2004; Wapenaar et al., 2004; Snieder, 2004a; Bensen et al., 2007; Wapenaar et al., 2010a, b). Seismic interferometry has been applied to image the earth's subsurface for a variety of objectives and at a wide range of scales. At continental and global scales this includes tomographic models which have helped understand crustal and mantle processes (e.g., Lin et al., 2008, 2009; Ekstrom et al., 2009; Ritzwoller et al., 2011; Haned, 2016).

1.2 Passive seismic interferometric workflow and assumptions

As mentioned earlier, interferometry estimates the seismic response between a pair of receivers (A, B) by correlating the noise recordings (x_A , x_B) within a common time window (Figure 1.1). The crosscorrelation function or the interferogram,

$$g_{A,B}(t) = x_B(t) \otimes x_A(t) \quad (1)$$

approximates the EGF (seismic response) between virtual source A and virtual receiver B. In equation (1) \otimes denotes correlation. The results correlation (Figure 1.1d) shows spikes in both positive (causal) and negative (acausal) time lags. This implies the existence of a symmetric noise field with noise approaching the receivers from both directions.

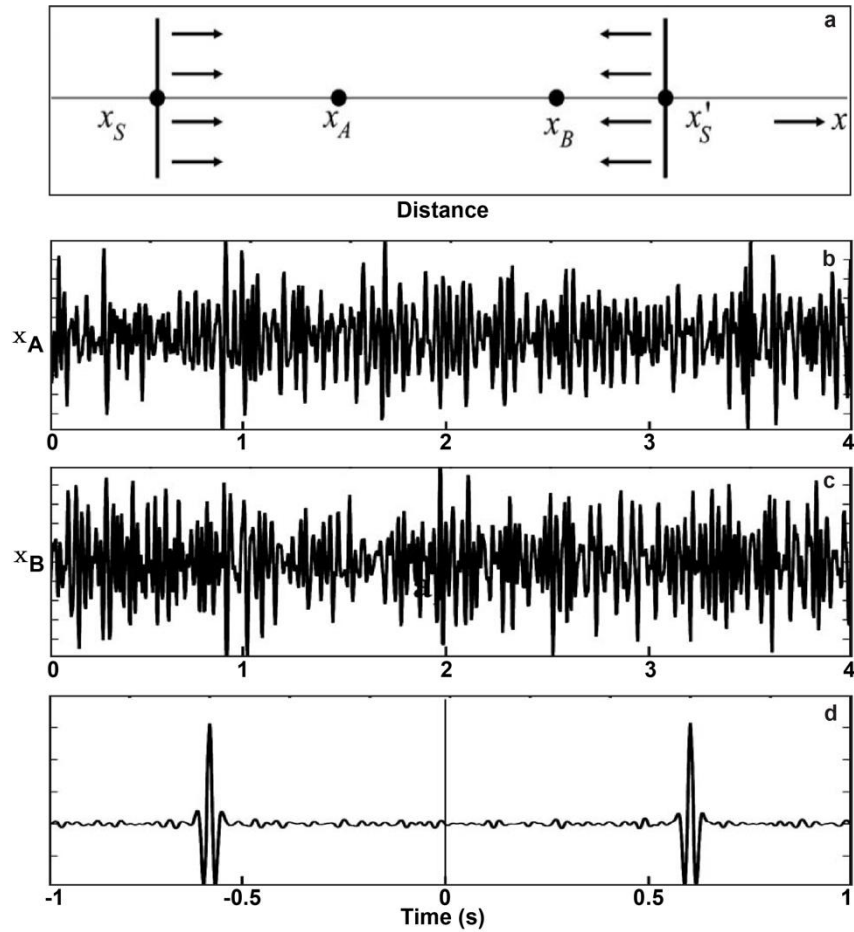


Figure 1.1. (a) Sources S and S' generating rightward and leftward propagating uncorrelated noise x_S and x'_S . (b) x_A is the noise recorded at receiver A. (c) x_B is the noise recorded at receiver B. (d) Crosscorrelation $x_B(t) \otimes x_A(t)$ of the noise recording. The illustration is modified from Wapenaar et al., 2010a.

A Fourier domain formulation of the equation (1) as multiplication of complex conjugate spectral amplitudes is also possible,

$$G_{A,B}(f) = X_B(f) \overline{X_A(f)}, \quad (2)$$

where the overbar denotes the complex conjugate. Both the temporal and spectral domain expressions of EGF are influenced by the temporally changing power spectra of the noise sources. This result is a time varying EGF. A spectrally normalizing version of equation (2) referred to as crosscoherency (Aki, 1957; Prieto et al., 2009; Wapenaar et al., 2010b),

$$G_{A,B}(f) = \frac{x_B(f) \overline{x_A(f)}}{|x_B(f)| |x_A(f)| + \epsilon^2}, \quad (3)$$

results in a time consistent EGF. Here, spectral normalization minimizes the influence of noise power spectra variations. In equation (3) a regularization factor (ϵ ; white noise) is used to stabilize the normalization.

An advantage of the interferometric approach is that the temporal and spatial locations of the noise sources is not important. However, the EGF estimation is subject to several assumptions (e.g., information about instrument response, attenuation factor, diffuse noise field). Out of these the availability of diffuse noise field is most critical for EGF estimation. Hodgson (1996) described a diffuse field as necessarily having - (i) random wave phases of equally partitioned energy, (ii) azimuthal isotropy and (iii) spatial homogeneity. This implies that for any two arbitrary point in the medium, one can be assumed to be a source while the other a receiver. Essentially opening up the possibility of interferometric Green's function retrieval as demonstrated by Weaver and Lobkis (2001) using a diffuse ultrasonic

noise field. However, several authors (e.g., Mulargia, 2012; Snieder, 2004) have shown that the real-world seismic wavefield is not truly diffuse. Snieder (2004) proposed and demonstrated a relaxation to the diffuse field constraint in the form of the stationary phase principle. Which states that the major contribution to the Green's function comes from sources that produce raypaths that are parallel before arriving at the receivers. For a pair of receivers, the stationary phase zone is the region along the outward extension of the line joining the receivers (Wapenaar et al., 2010a). Sources outside the stationary phase zone interfere destructively resulting in minimal contribution to the Green's function. Figure 1.1 shows an ideal 1D scenario where the noise sources occupy the station phase zone.

In the real-world scenario, noise sources of variable strength are distributed unevenly around the receivers. Nonetheless, at global scale the noise field is usually uniform, and the diffuse field assumption is easily enforced (Figure 1.2). This is done by normalizing the noise recordings from sources of variable strengths and stacking the interferograms to enhance the contribution from the stationary phase zone. However, at local scale the noise source distribution is highly heterogeneous. For example, anthropogenic sources like industrial operations and traffic are localized both spatially and temporally. In such cases normalization and stacking are not sufficient for retrieving the EGF.

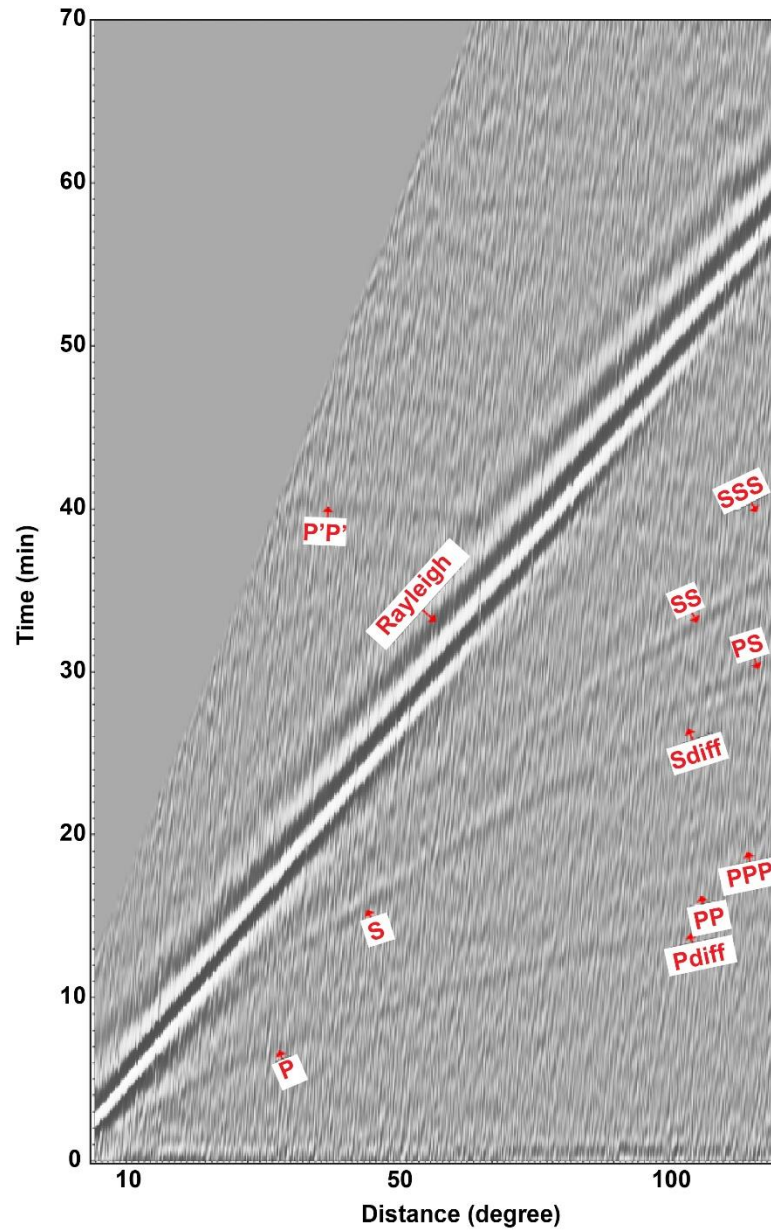


Figure 1.2. EGF retrieved by global interferometry showing Rayleigh wave and other body wave phases (modified from Haned et al., 2016).

1.3 Local scale applications of interferometry

While application of seismic interferometry to active-source data has been implemented at local exploration scale (e.g., Bakulin and Calvert, 2006; Carriere and Gerstoft, 2013), the use of passively recorded ambient noise is tempting as it offers a cost-effective alternative to active-source acquisitions. Several studies (e.g., Weaver and Lobkis, 2001; Snieder, 2004; Wapenaar et al., 2010a) have demonstrated the effectiveness of stacking the interferograms to improve the quality of the recovered Green's function. Considering the long duration of passive recordings which are required for effective implementation of stacking, the development of nodal seismic sensors that can record for long durations (months to years) has also contributed to the success of local and regional scale interferometry. However, these applications are usually limited to retrieval of surface waves (e.g., Behm et al., 2014; Wang et al., 2019; Jia and Clayton, 2021; Cheng et al., 2021) and comparably few studies successfully retrieve body waves (e.g., Draganov et al., 2007, 2009; Nakata et al., 2011). This is largely because recordings at surface station are dominated by surface waves in a wide frequency band - e.g., low frequency earth microseisms to high frequency anthropogenic sources (traffic, industrial noise, etc.). Moreover, based on the stationary phase principle, the interferometric retrieval of body wave reflections will require steeply arriving body waves. Such steep arrivals are rare at local scale except in regions with high

seismicity. Some researchers have extracted body waves from passive recordings at dense seismic networks by taking advantage of array-based processing techniques (e.g., Roux et al., 2005; Draganov et al., 2013; Almagro Vidal et al., 2014; Nakata et al., 2014, 2015; Cheraghi et al., 2017). However, small local seismic networks are generally restricted in offset and/or azimuthal extent limiting the application of such methodologies.

The overall motivation for this dissertation is to explore ways to make local scale interferometry possible given the highly non-diffuse nature of ambient noise and the scarcity of body waves in these settings. This is done by broadly two strategies – (i) selecting temporal windows of seismic energy that satisfy the stationary phase assumption (e.g., steeply incident body waves); (ii) carefully planning the deployment to confine the known sources of noise to the stationary phase zone. In this dissertation, I present applications of passive seismic interferometry at local deployments for high-resolution shallow subsurface (depths < 1 km) imaging in three diverse scenarios. All three scenarios deal with small arrays of sensors ranging from 15 to 120 in number. Apart from the overall objective, each application scenario also has an individual objective which is briefly introduced in the following section. These exploratory objectives which include – (i) reservoir scale reflectivity imaging, (ii) understanding the evolution of buried basement structure of a canyon, (iii) shear velocity modeling for urban seismic

hazard assessment, may be of interest to researchers beyond the passive seismic community.

1.4 Overview of the dissertation

In Chapter 2 and 3, considering the sparse geometry of a local monitoring network at a producing oil field, I develop single-station processing filters to extract body-waves from continuous ambient noise recordings. Particle motion induced by body waves (longitudinal P-waves, transverse S-waves) are distinct from surface waves. The polarization state of the particle motion during wave arrival at a 3-component (3C) seismic sensor is quantified in terms of attributes – linearity (Jurkevics, 1988) and incidence angle (Vidale, 1986) – which are used to selectively extract P- or S-waves. Single station interferometry (Autocorrelation) is then applied to the selected body waves to retrieve zero-offset reflection response of the subsurface structure. The frequency band of the body-wave data (< 10 Hz) allows the imaging of two prominent reflectors in the shallow sedimentary structure (< 1 km deep) which is also validated from well logs and active-source seismic data. The retrieval of both P- and S-wave reflectivity permits the estimation of the velocity ratio (V_p/V_s) which is reported by only a few passive seismic studies (e.g., Pham and Tklacic, 2018; Behm et al., 2019; Sergeant et al., 2020). Validation of the interferometrically-derived V_p/V_s estimates with the wells logs indicates the possibility of similar applications to study phenomena that influence V_p/V_s ratio.

These may include monitoring of icesheets and glaciers melting, and fluid injection/extract in geothermal reservoirs.

In Chapter 4, I demonstrate the application of passive seismic imaging to validate the hypothesis of Paleozoic glacial evolution of an alpine canyon in Colorado. The shape of the basement of a canyon is indicative of the causative geological processes (fluvial vs. glacial carving). To image the basement of Unaweep Canyon, passive seismic data are recorded at a linear array of 120 3C sensors along a 5-km long section of the canyon. Considering the scarcity of body waves in the dataset largely dominated by anthropogenic surface waves, I extract the body- waves from teleseismic signals. Autocorrelation is then applied to P-wave coda arrivals from 10 teleseismic events to illuminate the buried sedimentary-basement interface in the canyon. Additionally, I take advantage of the local high frequency ambient noise from traffic and operations at a near-by open-pit quarry for cross-correlation interferometry. The interferometrically retrieved dispersive surface waves are inverted to obtain a shear-wave velocity (V_s) and thickness model of the sedimentary fill overlying the basement. I interpret these results from two independent methodologies along with well and active-source data to show an undulating valley floor (200 – 500 m depth) with overdeepened features, supporting the hypothesis of glacial carving of Unaweep Canyon. This study also demonstrates the capability of short term (1 month) passive seismic deployments for imaging shallow targets at high-resolution.

In Chapter 5, I use passive seismic methods to image the near-surface structures in a sub-urban environment with the objective of assessing the seismic hazard at high lateral resolution (kilometer-scale). 1-month of continuous passive recordings at a ~20 km long 3C nodal geophone array are used to interferometrically retrieve surface waves which are then inverted to a Vs model of the subsurface. The frequency band (1 – 5 Hz) of the cultural noise in the area helps in imaging the sub-surface structure down to ~300 m depth. Additionally, horizontal-to-vertical spectral ratio (HVSR) is computed for the 3C recordings to further constrain the near-surface low-velocity layer. Combined interpretation of the HVSR and Vs models results in a robust estimation of the near-surface (< 100 m) structure which is then compared with a known site amplification model. The high lateral resolution site amplification model is calculated using a local earthquake recorded on a distributed acoustic sensing (DAS) array co-located with node array. Spatial correlation between the near-surface structure and site amplification validates the sensitivity of earthquake ground motion to near-surface structure.

1.5 Structure of the dissertation

This dissertation consists of 4 chapters, two of which are reformatted versions of published and submitted manuscripts and the other two are in preparation for submission. The chapters are as follows:

Chapter 2: Interferometric body-wave retrieval from ambient noise after polarization filtering: application to shallow reflectivity imaging.

Published: Dangwal, D., & Behm, M. (2021). Interferometric body-wave retrieval from ambient noise after polarization filtering: Application to shallow reflectivity imaging. *Geophysics*, 86(6).

Chapter 3: Passive reflectivity imaging and near-surface V_p/V_s ratio estimation after S-wave polarization filtering.

In preparation for submission: SSA Seismological Research Letters

Chapter 4: Imaging a paleovalley with passive seismic methods: Evidence for glacial carving of Unaweep Canyon (Colorado, US).

Submitted and under review: SSA The Seismic Record

Chapter 5: High-resolution imaging of the shallow subsurface and relationship with site responses using co-located Nodal and DAS arrays near Enid, Oklahoma.

In preparation for submission.

Bibliography

Aki, K. (1957). Space and Time Spectra of Stationary Stochastic Waves, with Special Reference to Microtremors. *Bulletin of the Earthquake Research Institute*, 35, 415–457.

Almagro Vidal, C., Draganov, D., van der Neut, J., Drijkoningen, G., & Wapenaar, K. (2014). Retrieval of reflections from ambient noise using illumination diagnosis. *Geophysical Journal International*, 198(3), 1572–1584. <https://doi.org/10.1093/gji/ggu164>.

Bakulin, A., & Calvert, R. (2006). The virtual source method: Theory and case study. *Geophysics*, 71(4). <https://doi.org/10.1190/1.2216190>

Behm, M., Cheng, F., Patterson, A., & Soreghan, G. S. (2019). Passive processing of active nodal seismic data: Estimation of VP.VS ratios to characterize structure and hydrology of an alpine valley infill. *Solid Earth*, 10(4), 1337–1354. <https://doi.org/10.5194/se-10-1337-2019>

Bensen, G. D., Ritzwoller, M. H., Barmin, M. P., Levshin, A. L., Lin, F., Moschetti, M. P., Shapiro, N. M., & Yang, Y. (2007). Processing seismic ambient noise data to obtain reliable broad-band surface wave dispersion measurements.

Geophysical Journal International, 169(3), 1239–1260.
<https://doi.org/10.1111/j.1365-246X.2007.03374.x>

Campillo, M., & Paul, A. (2003). Long range correlations in the diffuse seismic coda. *Science*, 299(5606), 547–549.
<https://doi.org/10.1126/science.1078551>

Carrière, O., & Gerstoft, P. (2013). Deep-water subsurface imaging using obs interferometry. *Geophysics*, 78(2), Q15–Q24.
<https://doi.org/10.1190/geo2012-0241.1>

Cheng, F., Xia, J., Ajo-Franklin, J. B., Behm, M., Zhou, C., Dai, T., Xi, C., Pang, J., & Zhou, C. (2021). High-Resolution Ambient Noise Imaging of Geothermal Reservoir Using 3C Dense Seismic Nodal Array and Ultra-Short Observation. *Journal of Geophysical Research: Solid Earth*, 126(8).
<https://doi.org/10.1029/2021JB021827>

Cheraghi, S., White, D. J., Draganov, D., Bellefleur, G., Craven, J. A., & Roberts, B. (2017). Passive seismic reflection interferometry: A case study from the aquistore CO2 storage site, Saskatchewan, Canada. *Geophysics*, 82(3), B79–B93. <https://doi.org/10.1190/GEO2016-0370.1>

Claerbout, J. F. (1968). Synthesis of a layered medium from its acoustic transmission response. *Geophysics*, 33(2), 264–269. <https://doi.org/10.1190/1.1439927>

Draganov, D., Campman, X., Thorbecke, J., Verdel, A., & Wapenaar, K. (2009). Reflection images from ambient seismic noise. *Geophysics*, 74(5). <https://doi.org/10.1190/1.3193529>

Draganov, D., Campman, X., Thorbecke, J., Verdel, A., & Wapenaar, K. (2013). Seismic exploration-scale velocities and structure from ambient seismic noise (>1 Hz). *Journal of Geophysical Research: Solid Earth*, 118(8), 4345–4360. <https://doi.org/10.1002/jgrb.50339>

Draganov, D. S., Wapenaar, K., Mulder, W., Singer, J., & Verdel, A. (2007). Retrieval of reflections from seismic background-noise measurements. *Geophysical Research Letters*, 34(4). <https://doi.org/10.1029/2006GL028735>

Ekström, G., Abers, G. A., & Webb, S. C. (2009). Determination of surface-wave phase velocities across USArray from noise and Aki's spectral formulation. *Geophysical Research Letters*, 36(18). <https://doi.org/10.1029/2009GL039131>

Haned, A., Stutzmann, E., Schimmel, M., Kiselev, S., Davaille, A., & Yelles-Chaouche, A. (2016). Global tomography using seismic hum. *Geophysical Journal International*, 204(2), 1222–1236. <https://doi.org/10.1093/gji/ggv516>

Jia, Z., & Clayton, R. W. (2021). Determination of Near Surface Shear-Wave Velocities in the Central Los Angeles Basin with Dense Arrays. *Journal of Geophysical Research: Solid Earth*, 126(5). <https://doi.org/10.1029/2020JB021369>

Jurkevics, A. (1988). Polarization analysis of three-component array data. *Bulletin of the Seismological Society of America*, 78(5), 1725–1743.

Lin, F. C., Moschetti, M. P., & Ritzwoller, M. H. (2008). Surface wave tomography of the western United States from ambient seismic noise: Rayleigh and Love wave phase velocity maps. *Geophysical Journal International*, 173(1), 281–298. <https://doi.org/10.1111/j.1365-246X.2008.03720.x>

Lin, F. C., Ritzwoller, M. H., & Snieder, R. (2009). Eikonal tomography: Surface wave tomography by phase front tracking across a regional broad-band seismic array. *Geophysical Journal International*, 177(3), 1091–1110. <https://doi.org/10.1111/j.1365-246X.2009.04105.x>

Lobkis, O. I., & Weaver, R. L. (2001). On the emergence of the Green's function in the correlations of a diffuse field. *The Journal of the Acoustical Society of America*, 110(6), 3011–3017. <https://doi.org/10.1121/1.1417528>

Mulargia F., 2012, The seismic noise wavefield is not diffuse: *The Journal of the Acoustical Society of America*, 131, 2853.

Nakata, N., Chang, J. P., Lawrence, J. F., & Boué, P. (2015). Body wave extraction and tomography at Long Beach, California, with ambient-noise interferometry. *Journal of Geophysical Research: Solid Earth*, 120(2), 1159–1173. <https://doi.org/10.1002/2015JB011870>

Nakata, N., Snieder, R., & Behm, M. (2014). Body-wave interferometry using regional earthquakes with multidimensional deconvolution after wavefield decomposition at free surface. *Geophysical Journal International*, 199(2), 1125–1137. <https://doi.org/10.1093/gji/ggu316>

Nakata, N., Snieder, R., Tsuji, T., Lerner, K., & Matsuoka, T. (2011). Shear wave imaging from traffic noise using seismic interferometry by cross-coherence. *Geophysics*, 76(6). <https://doi.org/10.1190/geo2010-0188.1>

Phạm, T. S., & Tkalčić, H. (2018). Antarctic Ice Properties Revealed From Teleseismic P Wave Coda Autocorrelation. *Journal of Geophysical Research: Solid Earth*, 123(9), 7896–7912. <https://doi.org/10.1029/2018JB016115>

Ritzwoller, M. H., Lin, F. C., & Shen, W. (2011). Ambient noise tomography with a large seismic array. *Comptes Rendus - Geoscience*, 343(8–9), 558–570. <https://doi.org/10.1016/j.crte.2011.03.007>

Roux, P., Sabra, K. G., Gerstoft, P., Kuperman, W. A., & Fehler, M. C. (2005). P-waves from cross-correlation of seismic noise. *Geophysical Research Letters*, 32(19), 1–4. <https://doi.org/10.1029/2005GL023803>

Sergeant, A., Chmiel, M., Lindner, F., Walter, F., Roux, P., Chaput, J., Gimbert, F., & Mordret, A. (2020). On the Green's function emergence from interferometry of seismic wave fields generated in high-melt glaciers: Implications for passive imaging and monitoring. *Cryosphere*, 14(3), 1139–1171. <https://doi.org/10.5194/tc-14-1139-2020>

Snieder, R. (2004). Extracting the Green's function from the correlation of coda waves: A derivation based on stationary phase. *Physical Review E - Statistical Physics, Plasmas, Fluids, and Related Interdisciplinary Topics*, 69(4), 8. <https://doi.org/10.1103/PhysRevE.69.046610>

Vidale, J. E. (1986). Complex polarization analysis of particle motion. *Bulletin of the Seismological Society of America*, 76(5), 1393–1405.

Wang, Y., Lin, F. C., & Ward, K. M. (2019). Ambient noise tomography across the Cascadia subduction zone using dense linear seismic arrays and double beamforming. *Geophysical Journal International*, 217(3), 1668–1680. <https://doi.org/10.1093/gji/ggz109>

Wapenaar, K. (2004). Retrieving the elastodynamic Green's function of an arbitrary inhomogeneous medium by cross correlation. *Physical Review Letters*, 93(25). <https://doi.org/10.1103/PhysRevLett.93.254301>

Wapenaar, K., Draganov, D., Snieder, R., Campman, X., & Verdel, A. (2010). Tutorial on seismic interferometry: Part 1 - Basic principles and applications. *Geophysics*, 75(5). <https://doi.org/10.1190/1.3457445>

Wapenaar, K., Slob, E., Snieder, R., & Curtis, A. (2010). Tutorial on seismic interferometry: Part 2 - Underlying theory and new advances. *Geophysics*, 75(5). <https://doi.org/10.1190/1.3463440>

Weaver, R. L., & Lobkis, O. I. (2001). Ultrasonics without a source: Thermal fluctuation correlations at mhz frequencies. *Physical Review Letters*, 87(13). <https://doi.org/10.1103/PhysRevLett.87.134301>.

Chapter 2

Interferometric body-wave retrieval from ambient noise after polarization filtering: application to shallow reflectivity imaging

2.1 Abstract

Interferometric retrieval of body-waves from ambient noise recorded at surface stations is usually challenged by the dominance of surface-wave energy, in particular in settings dominated by anthropogenic activities (e.g., natural resource exploitation, traffic, infrastructure construction). As a consequence, ambient noise imaging of shallow structures such as sedimentary layers remains a difficult task for sparse and irregularly distributed receiver networks. We demonstrate how polarization filtering can be used to automatically extract steeply inclined P-waves from continuous 3-component recordings and in turn improves passive body-wave imaging. Being a single-station approach, the technique does not rely on a dense receiver array and is therefore well suited for data collected during surveillance

monitoring for tasks such as reservoir hydraulic stimulation, CO₂ sequestration, and wastewater disposal injection. We apply the method on a continuous dataset acquired in the Wellington oilfield (Kansas, US), where local and regional seismicity, and other forms of ambient noise provide an abundant source of both surface and body-wave energy recorded at 15 short-period receivers. We use autocorrelation to derive the shallow (< 1 km) reflectivity structure below the receiver array and validate our workflow and results with well logs and active seismic data. Raytracing analysis and waveform modeling indicates that converted shear-waves need to be taken into account for realistic ambient noise body-wave source distributions, as they can be projected on the vertical component and might lead to misinterpretation of the P-wave reflectivity structure. Overall, our study suggests that polarization filtering significantly improves passive body-wave imaging on both autocorrelation and interstation crosscorrelation. It reduces the impact of time-varying noise source distributions and is therefore also potentially useful for time-lapse ambient noise interferometry.

2.2 Introduction

In the recent years, ambient seismic noise interferometry has become popular for subsurface imaging and monitoring because of minimal environmental impact and cost-effectiveness (Nakata et.al 2019). The method does not depend on controlled sources (e.g., dynamite, air guns, vibro-seis) with known origin location

and timing, but instead relies on the ubiquitous nature of different types of natural and anthropogenic seismic noise (e.g., ocean-wave induced micro-seisms, earthquakes, traffic) to generate seismic energy. A potentially broad frequency spectrum makes ambient noise interferometry feasible in a wide range of geographical and environmental settings.

The last two decades saw many applications of interferometric surface-wave retrieval on global and regional scales (e.g., Shapiro and Campillo, 2004; Bensen et al., 2007). Surface-wave interferometry is also applied on local scales (e.g., Behm et al., 2014; Hannemann et al., 2014; Chang et al., 2016; Martins et al., 2019) where however the creation of high-resolution subsurface models can be challenged by several limitations: (i) scarcity of high-frequency (> 5 Hz) ambient noise; (ii) insufficient noise-source density and azimuthal coverage to satisfy the stationary-phase assumption (Wapenaar et al., 2010b); (iii) incapability of sparse station networks to be used for spatial velocity analysis techniques; (iv) limited vertical and horizontal resolution of the surface-wave inversion approach. The last point suggests usage of body-waves, which however are less likely to be recovered from ambient noise recorded at surface stations (Forghani and Snieder, 2010).

Nonetheless, over the past decade body-wave interferometry has shown to be successful by taking advantage of borehole geophone deployment or subsurface recording environments such as mines or buried receivers (Boullenger et al., 2015;

Olivier et al., 2015; Behm, 2017; Dales et al., 2017; Zhou and Paulssen, 2017; Cheng et al., 2018). Interferometric retrieval of body-waves from surface recordings usually requires a larger number of receivers to apply array-based and other pre-processing methods to enhance body-wave energy. On a global scale, mapping of deep earth reflectivity structure is successful for large-N arrays (Boué et al., 2013; Lin et al., 2013; Ruigrok, 2014). On local scales, several studies introduced array-based methods for body-wave interferometry. Roux et al. (2005), used beamforming to determine the azimuthal distribution of high-velocity body-wave source, and then crosscorrelate recordings at station pairs that lie along the propagation direction to obtain body-wave rich interferograms. Nakata et al. (2011), demonstrated the presence of shear-wave reflections on virtual source gathers by crosscoherence interferometry of transverse component recordings. Other studies have used F-K transform (Draganov et al., 2013), multidimensional deconvolution for dense array with regular geometry (Nakata et al., 2014) and tau-p transform (Almagro Vidal et al., 2014; Cheraghi et al., 2017) to emphasize body-wave arrivals. At local scale the advantage of large-N arrays was also shown by Nakata et al. (2015), who derived a high-resolution subsurface velocity model of Long Beach, California based on body-wave extraction from an ultra-dense network of 2500 receivers.

Due to logistical and economic constraints, regular and dense deployments are not always possible. To overcome those geometrical requirements for body-

wave interferometry of surface recordings, Polychronopoulou et al. (2020), proposed a single-station approach using a short-time-average/long-time-average (STA/LTA) to identify and select body-wave dominant energy from local micro-earthquakes prior to reflection interferometry. In our study, we suggest a single-station approach based on polarization analysis of 3-component (3C) surface recordings to extract body-waves from continuous ambient noise. We demonstrate the feasibility of the approach by vertical component autocorrelation (Claerbout, 1968) to estimate the P-wave reflectivity response for the shallow ($< 1\text{km}$) subsurface. We validate our workflow by comparing the results with a body-wave rich dataset from a known earthquake catalog and by numerical modeling of receiver-side reflections and conversions. Furthermore, we relate our results to active seismic data and to a well log.

2.3 Study area and data

The Wellington oil field (Figure 2.1), part of the US Midcontinent oil province, is located in south-central Kansas, US. The sedimentary sequence comprises interlayered carbonate and clastics (Montgomery et al., 1998). The producing reservoir is a Mississippian age cherty dolomite overlaid by low porosity and permeability chert conglomerates, and a shale of Lower-Pennsylvanian age Cherokee group caps the reservoir (Watney et al., 2001). Another important unit in this sequence is the Arbuckle Group composed of Lower Ordovician and Upper

Cambrian dolomitized carbonates (Franseen and Byrnes, 2012). The Arbuckle group has been used for wastewater injection because of its high porosity due to dolomitization and fracturing. It is also a potential candidate for CO₂ sequestration purposes (Carr et al., 2005).

The Wellington oil field has produced over 20 MMBO since its discovery in 1929 (chasm.kgs.ku.edu) and had shifted to secondary (waterflood) production in 1957. In 2016, the reservoir was undergoing final stage of secondary recovery when a pilot CO₂ injection and sequestration was initiated to test the efficiency of a tertiary recovery method in improving production. An injection well KGS 2-32 (Figure 2.1) was drilled in March 2015 and was converted to a water injection well later (Holubnyak et.al, 2017).

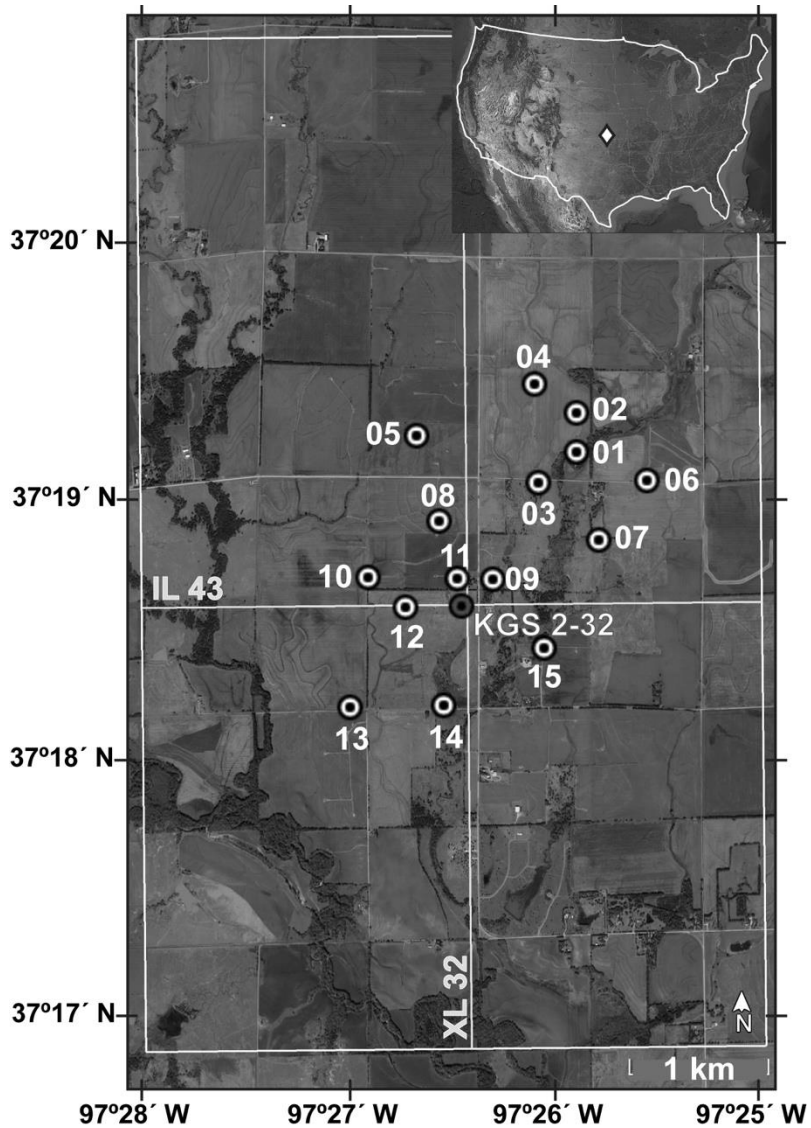


Figure 2.1: Map of Wellington field with local seismic array (white circles) and drilled well KGS 2-32 (gray circles). White box marks the extent of available active seismic data, with an inline and a crossline passing through the well location shown in Figure 10. Inset shows the location of Wellington in the continental USA.

A local seismic array (network code ZA; Watney, 2014) has been operated by the Kansas Geological Survey since 2014 to monitor induced seismicity associated with the injection (Figure 2.1). The array consists of 15 Sercel L-22 3C short-period sensors with corner frequency of 2 Hz, recording at 200 samples per second. The array was deployed in a scattered geometry over a $\sim 5 \text{ km}^2$ area with mean interstation distance of $\sim 600 \text{ m}$. For our study, we use 29,640 hours of data recorded between July 2014 and March 2018, referred to as ‘ambient noise dataset’ in the following.

Injection-induced seismicity in Oklahoma (Ellsworth, 2013; Keranen et al., 2014) is a major source of seismic body-wave energy arriving at the Wellington array. In this study, we use a regional catalog of seismicity in Oklahoma (Figure 2.2) to select body-wave events from the continuous dataset and to benchmark the feasibility of a proposed polarization-based event selection approach. Beamforming responses (Riahi et al., 2013) for the continuous dataset (Figure 2.3 a-d) show a scattered azimuthal distribution of noise sources with varying apparent horizontal velocity. This is due to the large number of anthropogenic sources in the vicinity (traffic, town of Wellington) and the presence of some non-stationary sources within the array boundary (production facilities and machinery). In contrast, beamforming response for selected catalog events (Figure 2.3 e-h) show clear back azimuth and high apparent horizontal velocity corresponding to steeply incident body waves at the array.

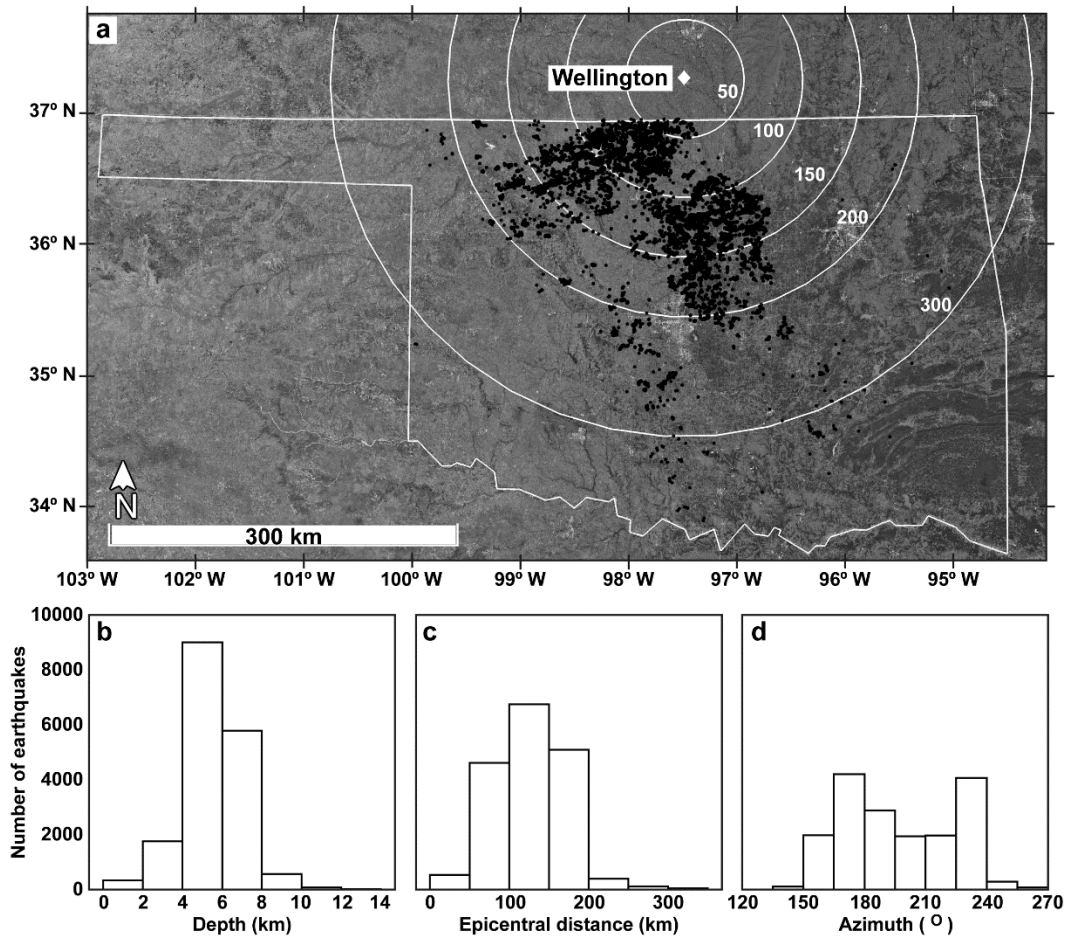


Figure 2.2: Map of Oklahoma (a) showing earthquake events (black dots) from a regional seismic catalog (<https://www.ou.edu/ogs/research/earthquakes/catalogs>) for the recording period (2014 – 2018). Concentric circles represent distance from Wellington array in kilometers. Histograms of hypocentral parameters: depth (b), epicentral distance from array (c) and azimuth of epicenter in relation to array (d).

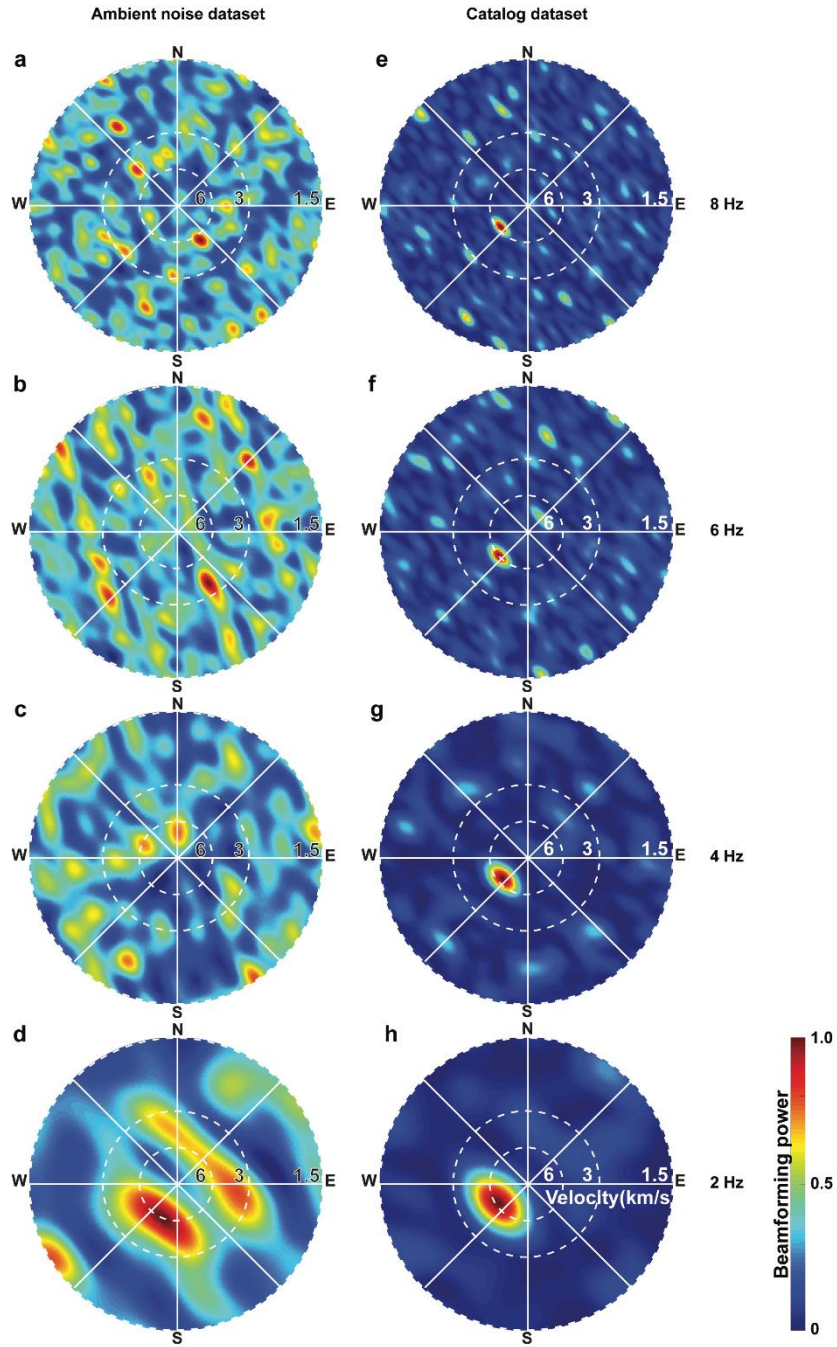


Figure 2.3: Vertical component beamforming analysis for ambient noise dataset event (a – d) and a catalog dataset event (e – h) extracted from the same ambient noise event. Each polar plot represents beamforming power (maximum: red,

minimum: blue) and its apparent velocity (radial axis in km/s) and back azimuth at unique frequencies.

2.4 Methods

Our goal is to improve interferometric body-wave retrieval at a sparse station network through automated pre-selection of data. We use two pre-selection criteria (earthquake catalog information, polarization filtering) and compare the results to interferometry without data pre-selection. We apply both interstation interferometry and single-station interferometry (autocorrelation), with the latter approach focusing on retrieval of the vertical P-wave reflectivity structure.

2.4.1 Data pre-selection using an existing earthquake catalog

To approximate data windows dominated by sub-vertical incidence P-wave energy, we use a catalog of 17,615 earthquake events (Figure 2.2) of magnitude greater than 2 with epicenters in Oklahoma (www.ou.edu/ogs/research/earthquakes/catalogs). Forward raytracing based on a recently derived crustal velocity model of Oklahoma (Ratre and Behm, 2021) suggests that the vast majority of the earthquake arrivals are diving waves travelling through the basement-crust and arriving at the array with steep incident angles (Appendix A). At large offset ranges, post-critical PmP (Moho reflections) and Pn

(mantle refractions) phases are also potential sources of seismic energy, although they are generally less well pronounced in the region (Ratre and Behm, 2021). We approximate the P-wave arrival time at the Wellington array by assuming a linear move-out with a constant velocity of 7000 m/s. Using a constant velocity higher than the actual crustal velocities (5800 – 6300 m/s) results in an earlier arrival time prediction, thereby ensuring that the P-wave arrival is included in the extracted window given the uncertainties in event localization and origin time estimation. Finally, a P-wave event is extracted from the ambient noise dataset using a 10-s window starting at the estimated arrival time calculated for the velocity of 7000 m/s. The fixed 10-s window is suitable for avoiding S-wave arrivals for epicentral distances >93 km, assuming diving wave trajectory and V_p/V_s ratio of 1.75. The resulting set of all 3C 10-s windows (ca. 44 hours of data) is referred to as ‘catalog dataset’ in the following. This approach, however, does not allow for accurate control over the incidence angle of selected P-waves.

2.4.2 Data pre-selection using polarization filtering

Ideally, a vertical P-wave reflectivity response can only be obtained from P-wave coda if the seismic energy is vertically incident at the receivers. Given the epicentral distance range of the earthquakes in the catalog dataset (Figure 2.2), the majority of these events represent both diving waves through the crust (P_g) as well as reflections (P_mP) from the Moho. Raytracing modeling for diving waves using

a recently established crustal velocity model (Ratre and Behm, 2021) suggests incidence angles lower than 30° for offsets > 100 km (Appendix A). This angle represents an upper boundary, as the model does not take the strong velocity contrasts in the sedimentary section into account, and thus smaller incidence angles for Pg and PmP phases will also be present.

P-wave energy with sufficiently small incidence angles might be directly identified through polarization filtering of the continuous data. Following Baillard et al. (2014), we use the polarization of the particle motion to differentiate between body-waves (linearly polarized) and surface-waves (polarized in a plane), and subsequently extract windows of low incidence angle for linearly polarized energy on all 3 components.

First, a 3x3 covariance matrix

$$C = \frac{1}{K} \begin{pmatrix} \sum_{i=1}^K N_i N_i & \sum_{i=1}^K N_i E_i & \sum_{i=1}^K N_i Z_i \\ \sum_{i=1}^K E_i N_i & \sum_{i=1}^K E_i E_i & \sum_{i=1}^K E_i Z_i \\ \sum_{i=1}^K Z_i N_i & \sum_{i=1}^K Z_i E_i & \sum_{i=1}^K Z_i Z_i \end{pmatrix} \quad (1)$$

is calculated for the 3C data within a 5-s long sliding time window. In equation 1, K is the number of samples within the time window, and Z , N , E are the waveform amplitudes recorded on the three orthogonal components (vertical, north, east). A 5-s time window was chosen as a trade-off between computation cost, considering

ca. 40 months of continuous data, and the ability to estimate variations in polarization at a high temporal resolution.

Next, using the ordered eigenvalues ($\lambda_1 \geq \lambda_2 \geq \lambda_3$) and corresponding eigenvectors ($\mathbf{V}_1, \mathbf{V}_2, \mathbf{V}_3$) of the covariance matrix, two polarization parameters were calculated. (i) Linearity defined as,

$$Linearity = 1 - \left(\frac{\lambda_2 + \lambda_3}{2\lambda_1} \right), \quad (2)$$

is based on degree of rectilinearity formulation of Jurkevics (1988). Linearity values close to 1 imply linear polarization of seismic energy or body-waves, while values close to 0 imply unpolarized seismic energy. A P-wave arrival results in increase of linearity values, but it never approaches 1 because of superimposed scattered and converted waves. (ii) Incidence (dip of the direction of maximum polarization) defined as,

$$Incidence = 90^\circ - \tan^{-1} \left(\frac{V_{1,Z}}{\sqrt{V_{1,E}^2 + V_{1,N}^2}} \right), \quad (3)$$

based on Vidale (1986). In equation 3, $V_{1,Z}$, $V_{1,N}$, $V_{1,E}$ are the components of \mathbf{V}_1 eigenvector. Incidence is the angle between the direction of maximum polarization and the vertical. For body-waves vertically arriving at a station, incidence is 0° for a P-wave (longitudinal), and 90° for an S-wave (transverse).

Figure 2.4 (a, b) shows the linearity and incidence angle calculated for two time windows that also include earthquakes. The first example (Figure 2.4a) includes a known earthquake from the regional catalog, and the second example (Figure 2.4b) shows an event not listed in the catalog but detected through the polarization filter. The P-wave first arrival appears as a local maximum in the linearity time-series, while the P-wave coda can be identified as a distinct trough feature in the incidence angle time-series. We extract P-wave events from the ambient noise data by identifying these features with imposed cutoff of 20° on the mean incidence angle within the trough. The choice of this incidence angle is motivated by the aforementioned ray tracing analysis which provides an upper threshold for the expected P-wave energy in our data set. A conventional STA/LTA detection algorithm would pick both P- and S-waves first arrivals, while the polarization filter highlights the steep incidence P-wave arrival only. Finally, 2566 unique P-wave events (ca. 7 hours of data) were identified using polarization filtering that constitute the 3C ‘polarization dataset’. This is a significantly smaller number than the events in the catalog, suggesting that events with small epicentral distances have incidence angles greater than 20° , or that P-wave arrivals are still superimposed with local surface-wave noise.

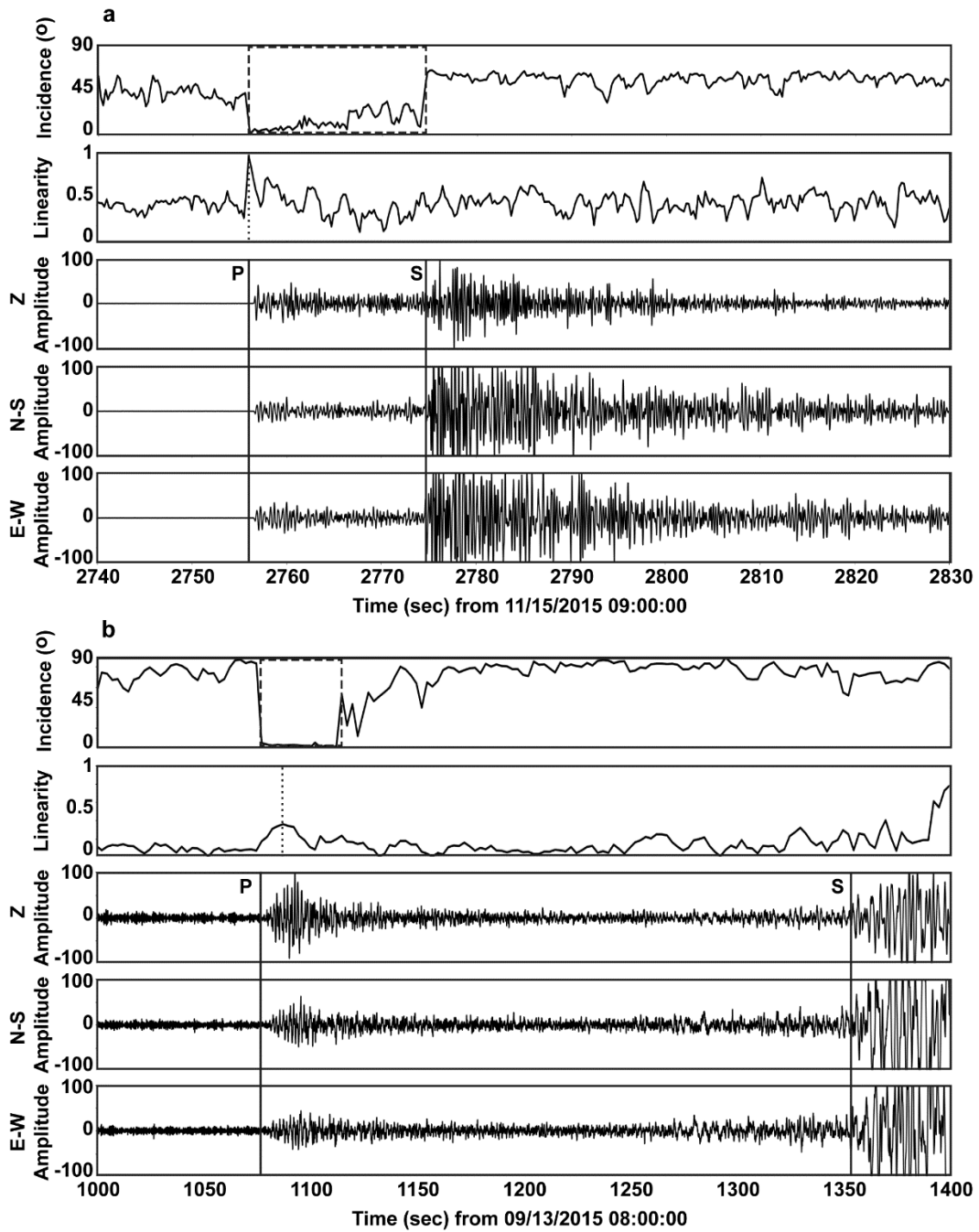


Figure 2.4: Application of polarization filtering to 3C ambient noise dataset recording during a) a local earthquake event also listed in the catalog. Origin time: 11/15/2015 09:45:31, Depth: 5.1 km, Magnitude: 4, Epicentral distance: 150 km,

Azimuth: 231.75° . b) An event not listed in the regional catalog. Dashed box represents the trough feature corresponding to sharp decline of incidence angle (between direction of maximum polarization and vertical) of P-wave energy. Dotted line represents a local maximum in linearity corresponding to P-wave arrival. The first solid line indicates P-wave first arrivals based on incidence trough and linearity maximum features that are used to extract a P-wave dominant event. The second solid line indicates S-wave first arrival based on a STA/LTA picker.

2.4.3 Pre-processing

Pre-processing applied to the datasets before application of interstation interferometry and autocorrelation includes: (i) Windowing – the ambient noise dataset was split in 6-hour long events. The catalog and polarization datasets were already created as discrete sets of events. (ii) De-trend. (iii) 1-10 Hz band pass filter. For this dataset frequencies beyond 10 Hz do not contribute to coherent interferograms and AC, while frequencies below 1 Hz do not suit the purpose of shallow imaging. (iv) Automatic gain control (AGC) with a window length of 0.2 s to compensate for varying strength of noise sources. This normalization approach was chosen after testing several methods such as 1-bit normalization and peak amplitude scaling. Spectral normalization (pre-whitening) was not applied since autocorrelation of spectrally whitened data would result in a zero-lag spike only, and in case of interstation interferometry, crosscoherence already includes spectral whitening.

2.4.4 Autocorrelation (AC)

AC is essentially seismic interferometry applied to data recorded at a single station. In the presence of near-vertical incident P-wave coda (direct and reflected arrivals) propagating in a horizontally layered earth, the AC response approximates the zero offset P-wave reflection response (Claerbout, 1968). Non-vertical incidence, however, will result in a kinematic error in reflectivity retrieval from AC (Appendix A). For steeper incidence angles (e.g., polarization dataset) the error magnitudes are reduced allowing for improved kinematic accuracy. AC has previously been used in a variety of scenarios, for imaging the Moho discontinuity (Ruigrok et al., 2011), lithosphere-asthenosphere-boundary (Kennett, 2015), lunar subsurface (Nishitsuji et al., 2016), shallow P-wave reflectivity (Saygin et al., 2017), and earthquake-induced changes in seismic velocity (Uemura et al., 2018).

We calculate the AC response for the three datasets (ambient noise, catalog dataset, polarization dataset). This was done by first autocorrelating each event in a dataset and then stacking all individual AC responses at a station to obtain the average AC response over the entire recording period. The AC response aims at imaging the receiver-side surface multiple, and to account for the reflection coefficient (-1) at the free surface, we reverse the polarity of the retrieved AC functions. The application of all processing steps is summarized in a flowchart in Figure 5.

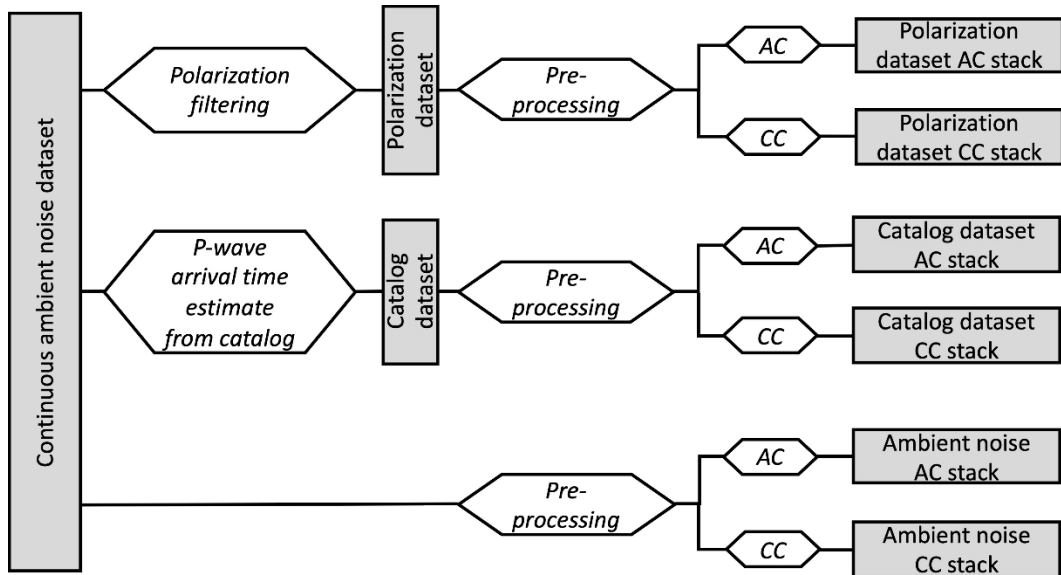


Figure 2.5: Flowchart summarizing data pre-selection methodologies applied to the ambient noise dataset to create the catalog and polarization datasets, and subsequent implementation of single-station (AC) and station-pair (CC; crosscoherence) interferometry.

2.5 Results and discussion

We apply station-pair interferometry and single-station AC to the three datasets to validate the polarization filter approach. Interferometric responses for the entire observation period were calculated for each station pair using crosscoherence (Aki, 1957; Prieto et al., 2009; Wapenaar et al., 2010a). Taking the small array aperture and the layer-cake geology into account, all individual interferograms were stacked in 100 m offset bins to obtain one representative virtual shot gather of the investigated area (Figure 2.6). The linear moveout of the

recovered phases is indicative of the dominant wave types in the respective datasets. The ambient noise dataset indicates a low linear moveout velocity (ca. 1500 m/s), corresponding to surface-waves in the low-frequency band (1 - 5 Hz), and does not show any evidence of high-velocity or high-frequency body-waves. The polarization dataset shows high linear velocity (ca. 6500 m/s) in both low (1 - 5 Hz) and high (5 - 10 Hz) frequency bands. This high apparent linear velocity is the result of selectively extracting steeply incident body-waves. The catalog dataset contains both body-waves and surface-waves, and surface-waves are still evident at low frequencies. This can be attributed to the catalog data pre-selection window and phase conversion phenomenon. Each catalog event contains pre-arrival ambient surface-waves as the window start time precedes the first arrival. Additionally, phase conversion of low incidence P-to-surface waves at the free surface can also generate low-amplitude Rayleigh waves. Overall, we observe that surface waves are confined to the low-frequency band and more prevalent in the ambient noise dataset. The polarization dataset is also interpreted for hyperbolic moveouts indicative of shallow reflections. However, these arrivals are weak, and their interpretation therefore is ambiguous. We attribute this to the sparse recording geometry which hampers phase correlation. Furthermore, the narrow range of incidence angles limits the offset range where interferometrically reconstructed reflections can be observed.

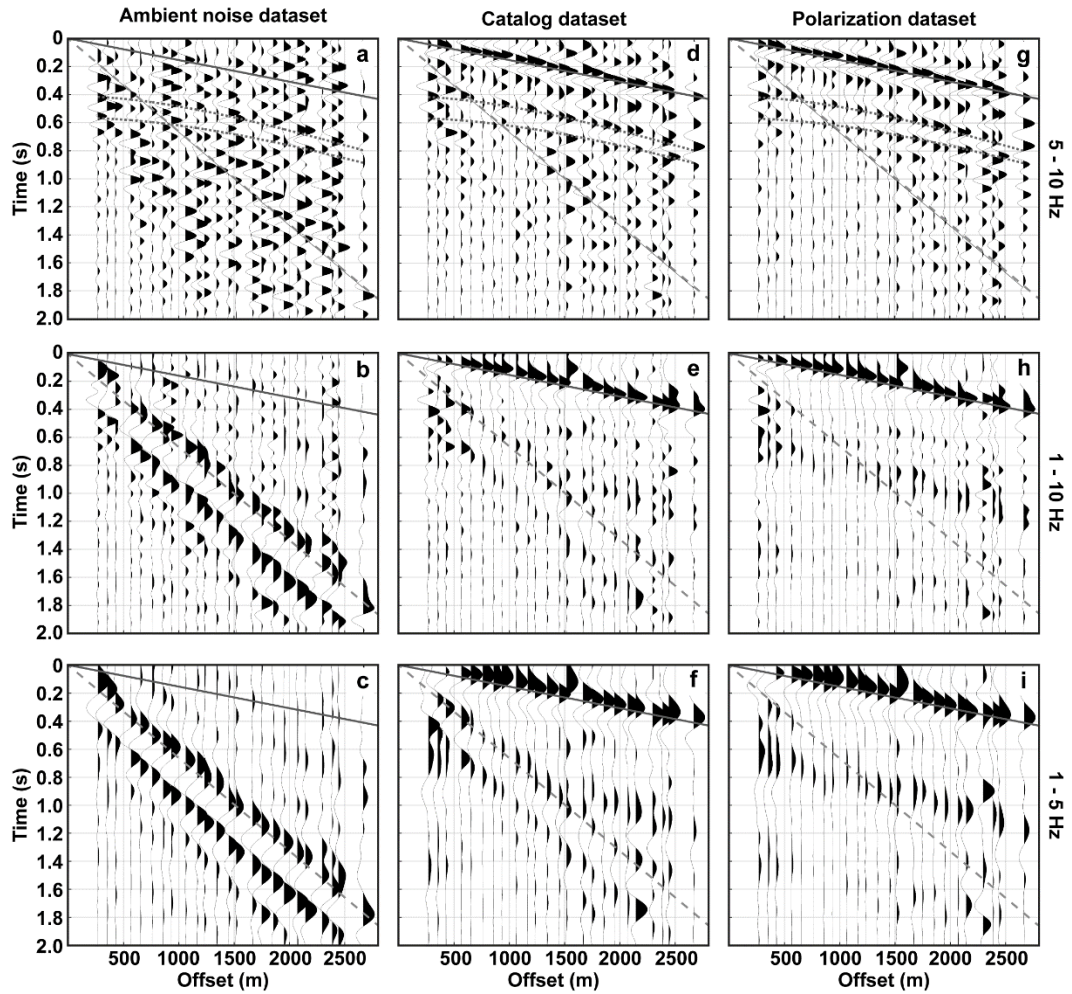


Figure 2.6: Comparison of vertical component interferometry for ambient noise dataset (a – c), catalog dataset (d – f) and polarization dataset (g – i) band passed in different frequency bands: 5 – 10 Hz (a, d, g), 1 – 10 Hz (b, e, h), 1 – 5 Hz (c, f, i). Overlaid are linear moveouts of 1500 m/s (dashed line) and 6500 m/s (solid line). Hyperbolic moveouts in (a, d, g) are calculated for a velocity of 3700 m/s and depths ranging from LeCompton to Kansas City formations.

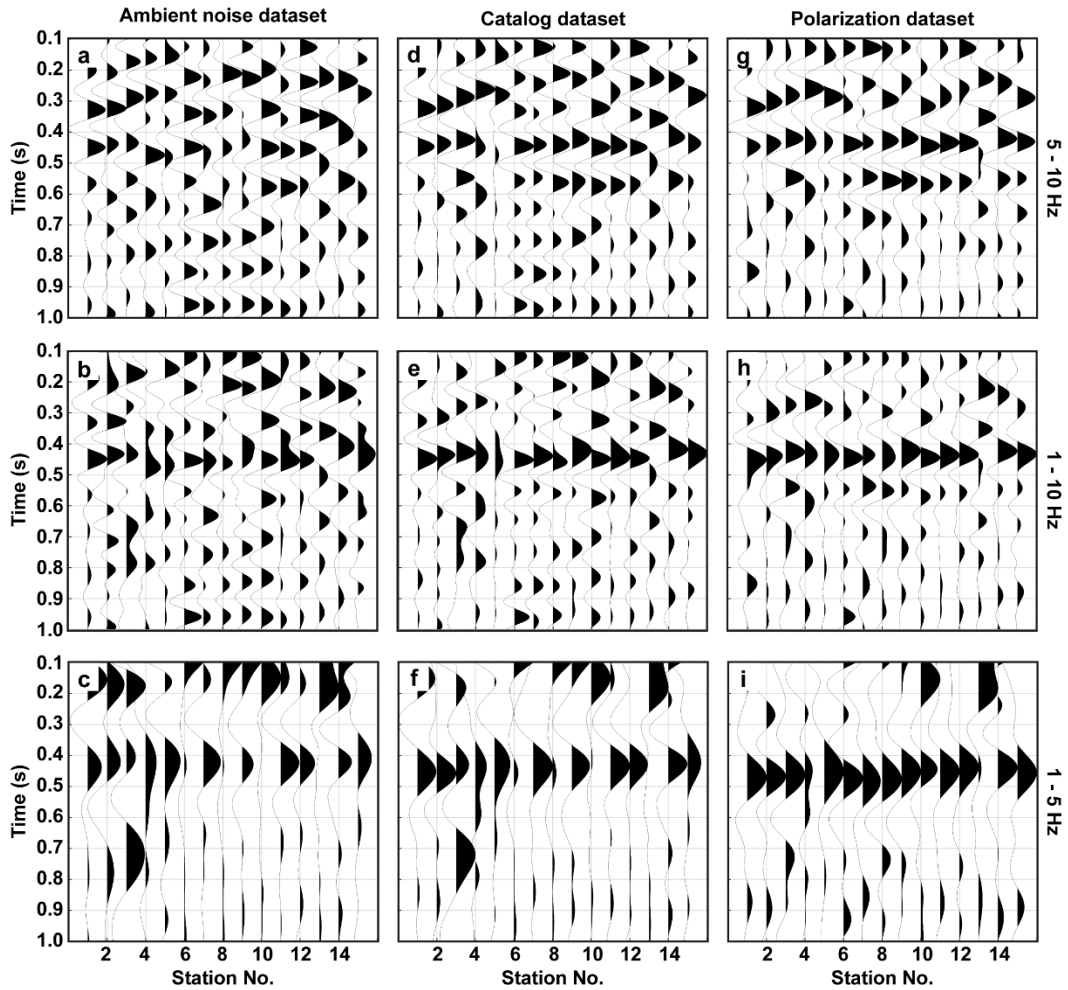


Figure 2.7: Comparison of vertical component AC stacks for ambient noise dataset (a – c), catalog dataset (d – f) and polarization dataset (g – i) band passed in different frequency bands: 5 – 10 Hz (a, d, g), 1 – 10 Hz (b, e, h), 1 – 5 Hz (c, f, i)

AC stacks of the three datasets were also band passed in the 1 - 5 Hz, 5 - 10 Hz and 1 - 10 Hz frequency ranges (Figure 2.7). The AC stacks were top muted at 0.1 s to suppress the zero-lag peak and its side lobes. The ambient noise AC stacks appear incoherent, especially in the frequency band of interest (5 - 10 Hz). A

consistent phase at ca. 0.43 s can be observed in all three frequency windows in the catalog and polarization datasets. However, the signal-to-noise ratio for this phase is enhanced in the polarization dataset. The catalog and polarization datasets show laterally continuous reflectors between 0.2 s and 0.6 s.

To validate the interpretation of the polarization AC results as subsurface reflectors, we perform AC for this dataset on the horizontal components (East-West, North-South) as well (Figure 2.8). We note that the distinct 0.43 s phase does not appear on the horizontal components, but instead we find laterally coherent phases at shallow times (< 0.3 s). We suggest that these shallow phases represent remnant surface-wave energy (Rayleigh and Love waves) as well as converted S-waves (see below). The 0.43 s phase observed on the vertical component is absent at the horizontal components. This strengthens the assumption that this phase represents a body-wave, as the vertical AC component should not include transverse Love waves while Rayleigh waves should show up on both the vertical and horizontal AC components.

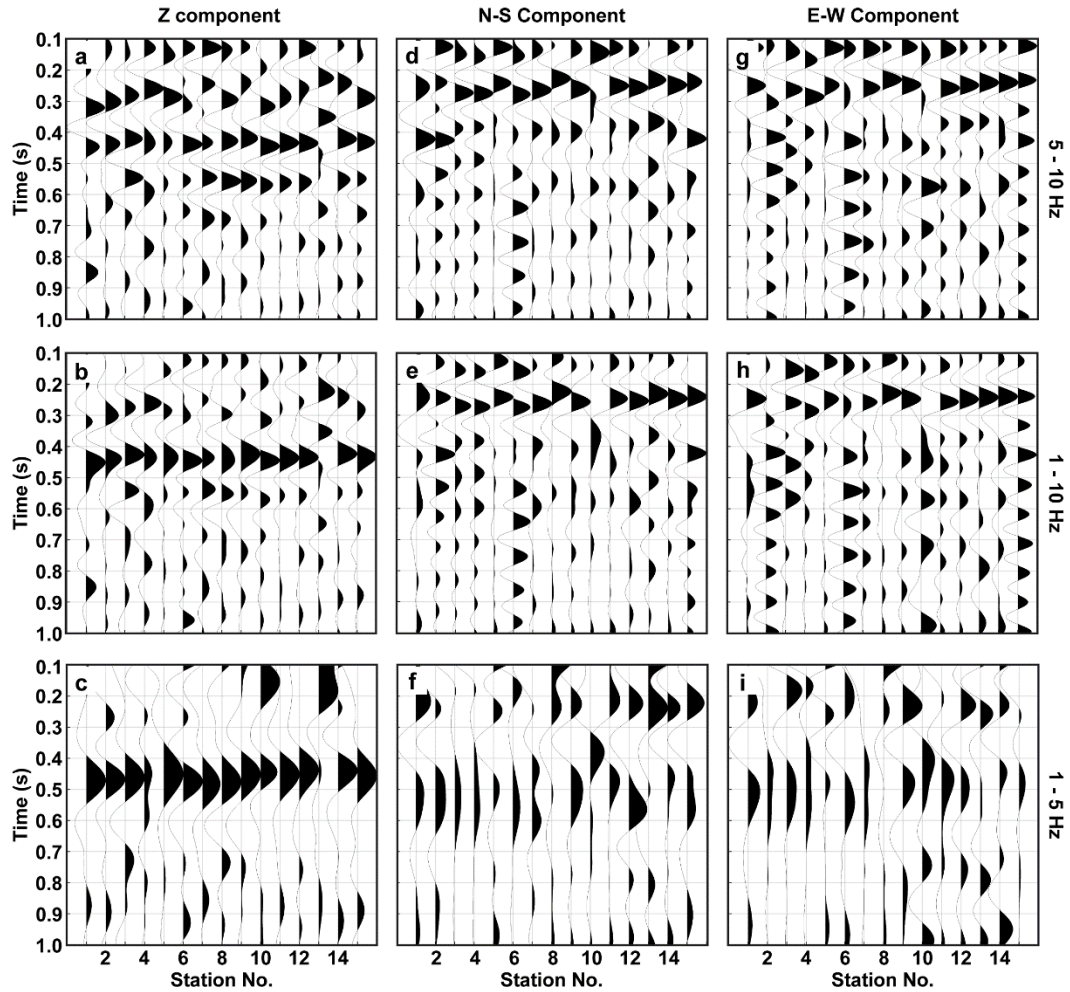


Figure 2.8: Comparison of Z component (a – c), North-South component (d – f) and East-West component (g – i) polarization dataset AC stacks band passed in different frequency bands: 5 – 10 Hz (a, d, g), 1 – 10 Hz (b, e, h), 1 – 5 Hz (c, f, i).

Non-vertical incidence of P-waves can lead to conversion of shear-waves at impedance boundaries which might project to the vertical component of the recording instrument. In order to investigate the magnitude of the potential

conversions and the crosstalk between horizontal and vertical components, we apply kinematic and dynamic ray tracing using the code ANRAY (Gajewski and Pšenčík, 1987; Figure 2.9). We assume a realistic crustal velocity model (Ratre and Behm, 2021) and an impedance contrast (crust-sediment transition) at 1 km depth. The sedimentary velocities are approximated by a gradient function representing an average Oklahoma basin structure (Darold et al., 2015). Assuming a range of epicentral distances and a source wavelet with a representative central frequency, we find that the converted shear-wave from the discontinuity at 1 km depth will arrive at ca. 0.3 s after the direct P-wave. Accordingly, converted waves from shallower discontinuities in the sedimentary section will arrive earlier. The non-vertical incidence also leads to significant amplitude projections of shear-waves on the vertical components and of P-waves on horizontal components. The shallow, laterally consistent phases at both horizontal and vertical component ACs therefore likely also include classical receiver functions.

Consequently, we refrain from interpreting shallow (< 0.3 s) phases on the vertical component in terms of P-wave subsurface structure and only consider phases after 0.3 s as receiver-side P-wave reflections. We exclude the possibility of a source-side surface reflection since we stack over a wide range of events with different source depths. The synthetic modeling further shows that the time delays between the P (direct) and PpP (free-surface multiple) phases vary with the epicentral distance due to the non-linear relationship between velocities and ray

paths. When stacking over events with different epicentral distances, we can therefore expect a loss of vertical resolution and lowering of apparent frequencies in the AC response. in the AC response.

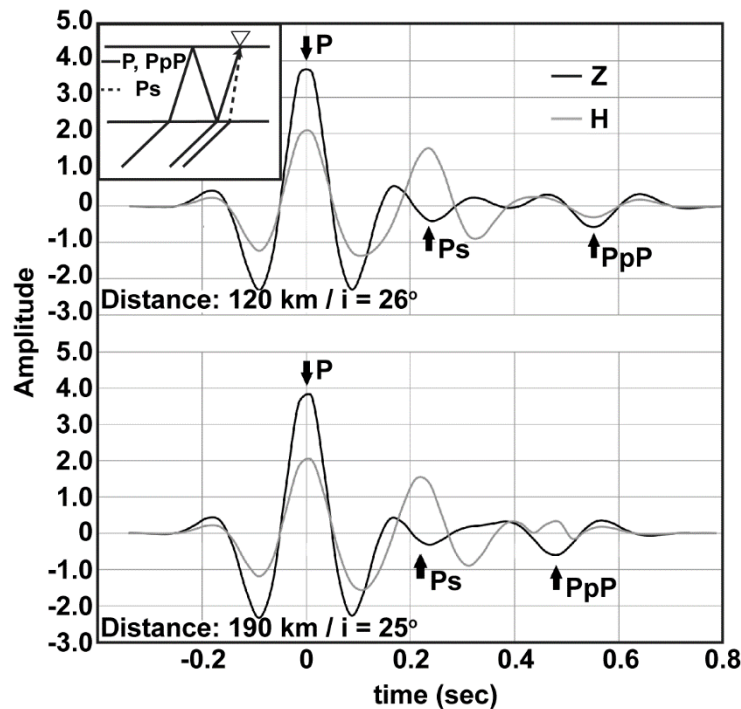


Figure 2.9: Synthetic modeling of waveforms (horizontal (H) and vertical (Z) components) for events in 120 and 190 km distance, respectively, after passing basement and a low-velocity sedimentary layer of 1 km thickness. P: direct P-wave; Ps: S-wave converted from P-wave impinging on the sediment-basement boundary. PpP: free-surface multiple. Note the projection of P-wave amplitudes at the horizontal component and of S-wave amplitudes at the vertical component, and the variation in PpP arrival times due to the varying epicentral distance.

Next, we look at temporal stability of AC responses for the 3 datasets over the acquisition period. This is done by creating time-lapse AC gathers at two

stations (03, 11) where each trace represents the average AC response for a period of 1 month (Figure 2.10). In the high-frequency band (5 - 10 Hz), the time lapse AC gathers for the ambient noise and catalog dataset vary both in terms of amplitude and time-lag peaks. This is likely the effect of azimuthal changes of superimposed surface-waves over the recording period. Additionally, in the catalog dataset, large variation in event epicentral distances (Figure 2.10 e) and no constraints on incidence angles also results in temporally variable AC stacks. In contrast, the time-lapse AC stacks for the polarization dataset are temporally stable because of the dominance of near-vertical P-waves even though the number of selected events per month (Figure 2.10 h) is low when compared to the catalog dataset. Time-lapse seismic interferometry is increasingly used for seismic monitoring (Sens-Schönfelder and Wegler, 2006; Behm, 2017; Zhou and Paulssen, 2020), where however in many cases the interpretation is challenged by the unknown temporal variation of the noise sources. The improved stability achieved through polarization filtering can be helpful to discern true from apparent medium changes.

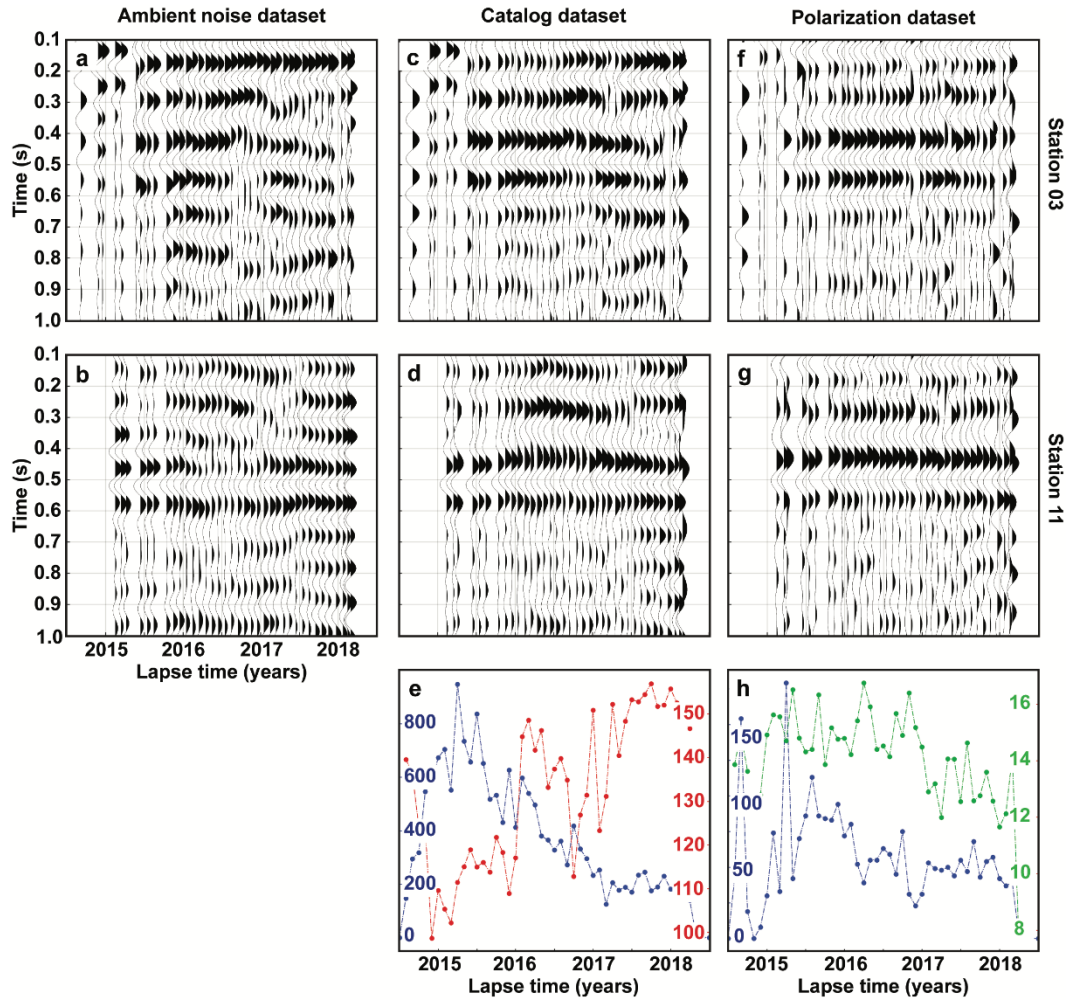


Figure 2.10: Comparison of time-lapse vertical component AC stacks for ambient noise dataset (a, b), catalog dataset (c, d) and polarization dataset (f, g) band passed in 5 – 10 Hz range for stations 03 (a, c, f) and 11 (b, d, g). (e) Variation of number of earthquakes (blue) and median epicentral distance (red, km) for catalog dataset. (h) Variation of number of selected events (blue) and median incidence angle at the array (green, °) for the polarization dataset.

Lastly, we compare the polarization dataset AC stack to other available data (Figure 2.11). Depth-to-time converted bulk density and sonic (P-wave) logs from

well KGS 2-32 (Figure 2.1) were used to construct time-domain acoustic impedance and reflectivity logs. Synthetic seismograms were generated by convolving the reflectivity logs with stationary Ricker wavelets of 5 and 10 Hz central frequency. The available active-source data (time converted depth migration) is band-pass filtered from 4 – 20 Hz. To enhance the resolution and lateral continuity of observed reflectors, the polarization AC stack of all stations underwent two post-processing steps. First, we applied a band-pass filter of 5 – 10 Hz. Secondly, we applied eigenimage reconstruction (Freire and Ulrych, 1988) to the filtered AC stack. Eigenimage reconstruction can be used to increase or minimize lateral coherency of a seismic wavefield, and by retaining the top 20% eigenvalues we aim for emphasizing the lateral continuity given the small aperture of the recording array.

The 0.43 s and 0.55 s coherent phases in the AC stack correspond to the impedance contrasts associated with the LeCompton and Kansas City (KC) top reflectors. Both these reflectors are prominent in the well-log-derived synthetic. However, the Kansas City top, which represents a strong impedance contrast in the well log data, cannot be clearly discerned in the active seismic stack. The deeper reflector (Mississippi top) that appear on the active seismic stack is not clearly observed on the AC stack. This may be related to insufficient resolution capability of the low-frequency passive-seismic data which is further aggravated by loss of high frequencies as surface-related reflections propagate into the deeper subsurface.

Furthermore, as illustrated by the ray tracing analysis, even a narrow range of incidence angles ($0^\circ - 20^\circ$) will degrade the vertical resolution due to smearing of the stacked AC function.

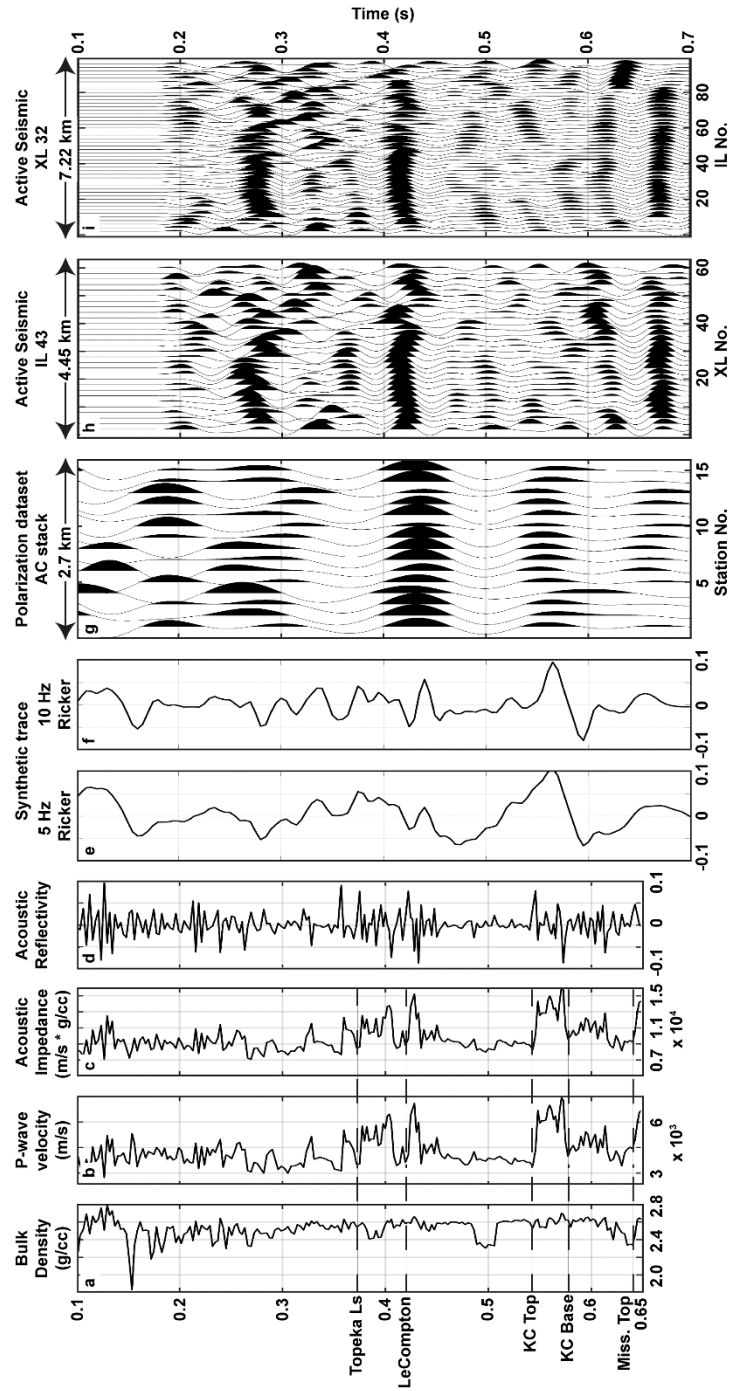


Figure 2.11: Comparison of well log and well log derived data with AC stack and active seismic stacks. Well log data includes (a) bulk density log, (b) sonic log from

KGS 2-32 well. Derived well log data includes (c) acoustic impedance, (d) acoustic reflectivity and synthetic traces using (e) 5 Hz Ricker wavelet and (f) 10 Hz Ricker wavelet. Polarization AC stack (g) is band passed in 5 – 10 Hz range and eigenimage reconstructed using top 20% eigenvalues. Active-seismic data used for comparison along (h) IL 43 and (i) XL 32 (Figure 2.1).

2.6 Conclusions

We applied polarization filtering to 3C recordings of continuous ambient noise to select body-waves based on linearity and incidence attributes. Being a single-station approach, the method is applicable to sparse and small arrays with irregular geometries. It is particularly suited for areas like Wellington where sufficient body-wave energy is present due to induced seismicity in Oklahoma. Although seismicity is not uniformly distributed over the recording period, we still observe temporally stable AC results for the polarization dataset. This suggests that a small amount of steeply incident body-wave events (7 hours compared to 29,640 hours of ambient noise) is sufficient to significantly improve reflectivity imaging.

In our study, polarization filtering and AC aiming at high resolution imaging is hampered by the limited frequency content of steeply incident ambient seismic energy. Apart from the local high-frequency noise from machinery, which does not contribute towards coherent AC, the ambient noise and induced seismicity appears of relatively low frequency (< 10 Hz). Nonetheless, the 5 – 10 Hz band is

able to resolve two prominent reflectors in the shallow sedimentary sequence. Other reflectors are too thin and/or have too low impedance contrast to be resolved.

Our analysis also shows that the incidence angle has significant impact on interferometric retrieval of reflected body-waves. A broad range of incidence results in varying time delays of the reflections for a given horizon and stacking over those different events will further lower the effective frequency. Non-vertical incidence further leads to crosstalk between horizontal and vertical amplitude components and the generation of converted shear-waves which in turn challenges interpretation of the shallowest horizons.

Polarization filtering can in particular be useful in absence of an earthquake catalog to automatically extract body-wave energy. Even with the availability of a catalog, the approach has its merits to either filter the catalog dataset into preferred incident angle ranges, or to augment the catalog by adding steeply incident global and regional events that might be missing in a local catalog. The method can be adapted to extract shear-waves by selecting large incidence angles, although the weaker expression of linearity for shear-waves might pose a challenge. Overall, our analysis suggests that polarization filtering significantly improves body-wave interferometry, and as such is a useful pre-processing tool for single-station AC or interstation interferometric imaging for sparse and irregular networks. The reduced

impact of temporal noise source variations suggests that the technique can also be helpful to strengthen the interpretation of time-lapse seismic interferometry.

2.7 Appendix

2.7.1 Kinematics of AC applied to sub-vertical incident source data

We use a two-layer (sedimentary and basement) model (Figure A2.12) to understand the kinematics of ray propagation from local and regional seismicity and its implication for reflectivity estimation from AC. The basement velocities are based on a recent crustal velocity model of Oklahoma (Ratre and Behm, 2021) which is characterized by a positive and smooth vertical velocity gradient, and the sedimentary velocities represent a smooth version of the average Oklahoma basin structure (Darold et al., 2015). The shallow basement-sedimentary interface is at 1 km depth.

We use ANRAY code (Gajewski and Pšenčík, 1987) to propagate rays in the model from a sub-basement source at 5 km depth to surface stations where direct P, basement reflected PpP and converted shear wave Ps phases are recorded (Figure A2.12). Synthetic data (waveforms) are calculated by convolving the ray tracing amplitudes with a 5 Hz minimum-phase wavelet. For the considered

geometry and velocity model, the direct P is a diving phase with incidence angle of $< 30^\circ$ in this range of the chosen epicentral distances (100 – 290 km).

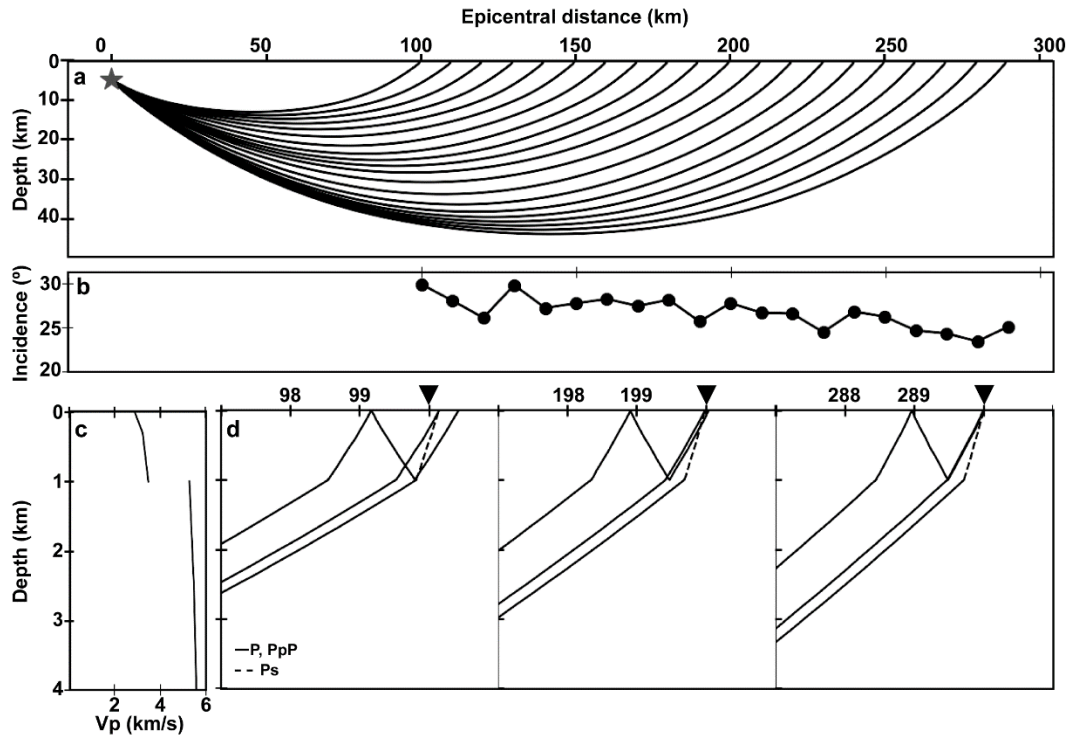


Figure A2.12: (a) Direct P ray paths and (b) surface incidence angles at epicentral range 100 – 290 km for a sub-basement source at 5 km depth. (c) V_p model showing sedimentary-basement interface at 1 km depth, (d) ray paths for P, PpP, Ps phases arriving at epicentral distances 100 km, 200 km, 290 km (black inverted triangles).

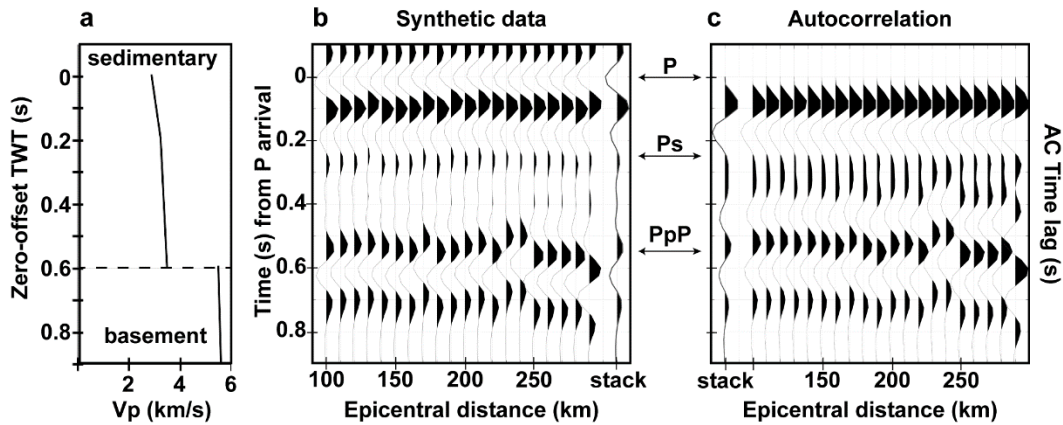


Figure A2.13: (a) Depth to TWT converted velocity model showing the sedimentary-basement interface. (b) Polarity reversed synthetic traces at epicentral distances 100 – 290 km and their corresponding (c) polarity reversed AC. Stacks represent the mean trace. Annotated P, Ps, PpP arrival times are the mean arrival times for each phase over the epicenter range.

The ACs of the synthetic data (Figure A2.13) represent the time lag of PpP and Ps phases in relation to the direct P phase. AC traces have been top muted to suppress the zero-lag peak; however, the side lobe at ca. 0.1 s still remains. To emphasize the PpP phase, both synthetic data and ACs are polarity reversed to account for the negative reflection coefficient at the free surface. The scatter in PpP arrival time over epicentral distance is attributed to the discrete step sizes of the numerical integration variables of the ray tracing system and resulting inaccuracies. Although the AC correctly retrieves the non-zero offset PpP reflection time, there is a -0.05 s error when compared with zero offset two-way-time for this velocity model (the zero-offset arrival comes a bit later). This kinematic error in AC

reflectivity is a consequence of non-vertical incidence, and can be explained by splitting the total travelttime lag between P and PpP phases into sedimentary and basement segments as

$$TT_{PpP, sed}^{\theta} - TT_{P, sed}^{\theta} = TWT_{sed}^0 + \epsilon_{sed}^{\theta}, \quad (\text{A-1})$$

$$TT_{PpP, base}^{\theta} - TT_{P, base}^{\theta} = 0 + \epsilon_{base}^{\theta}, \quad (\text{A-2})$$

where $TT_{PpP, sed}^{\theta}$, $TT_{P, sed}^{\theta}$ are the traveltimes for PpP and P phases in the sedimentary layer and arriving at the same free-surface location with θ incidence. $TT_{PpP, base}^{\theta}$, $TT_{P, base}^{\theta}$ are the traveltimes for PpP and P phases in the basement layer from source to the sedimentary-basement interface. TWT_{sed}^0 is the P-wave zero-offset two-way-time from the free-surface to the sedimentary-basement interface. The zero-offset TWT term for the basement is 0 as the model does not account for internal multiples in the basement. ϵ_{sed}^{θ} , ϵ_{base}^{θ} are sedimentary and basement contribution to the kinematic error in AC reflectivity, respectively.

Both error terms are 0 for vertical incidence. For non-vertical incidences, ϵ_{sed}^{θ} is positive as the PpP phase travels a longer path in the sedimentary layer than a vertically incident PpP. ϵ_{base}^{θ} is negative for non-vertical incidences as the P phase has a longer travel path in the basement to arrive at the same surface location

as the PpP (Figure A2.12 d). The total kinematic error in AC reflectivity associated with entire travel paths,

$$\epsilon_{total}^{\theta} = (TT_{PpP,total}^{\theta} - TT_{P,total}^{\theta}) - TWT^0, \quad (A-3)$$

can be obtained by adding and rearranging equations A-1 and A-2, where $TT_{PpP,total}^{\theta}$ and $TT_{P,total}^{\theta}$ are the traveltimes for PpP and P phases from the source to the same free-surface location, respectively. The total error being negative (-0.05 s) for the $< 30^{\circ}$ incidence case implies that $\epsilon_{base}^{\theta} < -\epsilon_{sed}^{\theta}$, i.e., the difference in basement traveltimes is over-compensated by the difference in sedimentary traveltimes. It is noted that those results should not be generalized, as wave propagation and ray tracing depend in a non-linear way on the velocity model. For the acquisition geometry, expected geology, and frequency range of the data we have chosen appropriate values for our case study. However, an inherent limitations of ray tracing is the requirement for a smooth velocity model which does not allow to introduce fine structures (e.g., thin intra-sedimentary layering with strong velocity contrasts) into the model.

Bibliography

Aki, K., 1957, Space and Time Spectra of Stationary Stochastic Waves, with Special Reference to Microtremors: Bulletin of the Earthquake Research Institute, 35, 415–457.

Almagro Vidal, C., D. Draganov, J. van der Neut, G. Drijkoningen, and K. Wapenaar, 2014, Retrieval of reflections from ambient noise using illumination diagnosis: Geophysical Journal International, 198, 1572–1584.

Baillard, C., W. C. Crawford, V. Ballu, C. Hibert, and A. Mangeney, 2014, An automatic kurtosis-based P-and S-phase picker designed for local seismic networks: Bulletin of the Seismological Society of America, 104, 394–409.

Behm, M., 2017, Feasibility of borehole ambient noise interferometry for permanent reservoir monitoring: Geophysical Prospecting, 65, 563–580.

Behm, M., G. M. Leahy, and R. Snieder, 2014, Retrieval of local surface wave velocities from traffic noise - an example from the La Barge basin (Wyoming): Geophysical Prospecting, 62, 223–243.

Bensen, G. D., M. H. Ritzwoller, M. P. Barmin, A. L. Levshin, F. Lin, M. P. Moschetti, N. M. Shapiro, and Y. Yang, 2007, Processing seismic ambient noise

data to obtain reliable broad-band surface wave dispersion measurements: *Geophysical Journal International*, 169, 1239–1260.

Boué, P., P. Poli, M. Campillo, H. Pedersen, X. Briand, and P. Roux, 2013, Teleseismic correlations of ambient seismic noise for deep global imaging of the Earth: *Geophysical Journal International*, 194, 844–848.

Boullenger, B., A. Verdel, B. Paap, J. Thorbecke, and D. Draganov, 2015, Studying CO₂ storage with ambient-noise seismic interferometry: A combined numerical feasibility study and field-data example for Ketzin, Germany: *Geophysics*, 80, no. 1, Q1–Q13.

Carr, T. R., D. F. Merriam, and J. D. Bartley, 2005, Use of relational databases to evaluate regional petroleum accumulation, groundwater flow, and CO₂ sequestration in Kansas: *American Association of Petroleum Geologists Bulletin*, 89, 1607–1627.

Chang, J. P., S. A. L. de Ridder, and B. L. Biondi, 2016, High-frequency Rayleigh-wave tomography using traffic noise from Long Beach, California: *Geophysics*, 81, no. 2, B1–B11.

Cheng, F., D. Draganov, J. Xia, Y. Hu, and J. Liu, 2018, Q-estimation using seismic interferometry from vertical well data: *Journal of Applied Geophysics*, 159, 16–22.

Cheraghi, S., D. J. White, D. Draganov, G. Bellefleur, J. A. Craven, and B. Roberts, 2017, Passive seismic reflection interferometry: A case study from the aquistore CO2 storage site, Saskatchewan, Canada: *Geophysics*, 82, no. 3, B79–B93.

Claerbout, J. F., 1968, Synthesis of a layered medium from its acoustic transmission response: *Geophysics*, 33, 264–269.

Dales, P., P. Audet, and G. Olivier, 2017, Seismic Interferometry Using Persistent Noise Sources for Temporal Subsurface Monitoring: *Geophysical Research Letters*, 44, 10,863-10,870.

Darold, A.P., A. A. Holland, J. K. Morris, and A. R. Gibson, 2015, Oklahoma Earthquake Summary Report 2014, Oklahoma Geological Survey, Open-File Report, OF1- 2015. <http://ogs.ou.edu/docs/openfile/OF1-2015.pdf>, accessed 5 October 2020

Draganov, D., X. Campman, J. Thorbecke, A. Verdel, and K. Wapenaar, 2013, Seismic exploration-scale velocities and structure from ambient seismic noise (>1 Hz): *Journal of Geophysical Research: Solid Earth*, 118, 4345–4360.

Ellsworth, W. L., 2013, Injection-induced earthquakes: *Science*, 341.

Forghani, F., and R. Snieder, 2010, Underestimation of body waves and feasibility of surface-wave reconstruction by seismic interferometry: *Leading Edge*, 29, 790–794.

Franseen, E. K., and A. P. Byrnes, 2012, Arbuckle group platform strata in Kansas: A synthesis, *in* AAPG Memoir, Vol. 98. American Association of Petroleum Geologists, 1031–1047.

Freire, S. L. M., and T. J. Ulrych, 1988, Application of singular value decomposition to vertical seismic profiling: *Geophysics*, 53, 778–785.

Gajewski, D., and I. Pšenčík, 1987, Computation of high-frequency seismic wavefields in 3-D laterally inhomogeneous anisotropic media, *Geophysical Journal International*, 71491(2), 383–411.

Hannemann, K., C. Papazachos, M. Ohrnberger, A. Savvaidis, M. Anthymidis, and A. M. Lontsi, 2014, Three-dimensional shallow structure from high-frequency ambient noise tomography: New results for the Mygdonia basin-Euroseistest area, northern Greece: *Journal of Geophysical Research: Solid Earth*, 119, 4979–4999.

Holubnyak, Y., W. Watney, J. Rush, M. Fazelalavi, and D. Wreath, 2017, Pilot Scale CO₂ EOR in Mississippian Carbonate Reservoir at Wellington Field in South-central Kansas: *Energy Procedia*, 114, 6989–6996.

Jurkevics, A., 1988, Polarization analysis of three-component array data: *Bulletin of the Seismological Society of America*, 78, 1725–1743.

Kennett, B. L. N., 2015, Lithosphere-asthenosphere P-wave reflectivity across Australia: *Earth and Planetary Science Letters*, 431, 225–235.

Keranen, K. M., M. Weingarten, G. A. Abers, B. A. Bekins, and S. Ge, 2014, Sharp increase in central Oklahoma seismicity since 2008 induced by massive wastewater injection: *Science*, 345, 448–451.

Lin, F. C., V. C. Tsai, B. Schmandt, Z. Duputel, and Z. Zhan, 2013, Extracting seismic core phases with array interferometry: *Geophysical Research Letters*, 40, 1049–1053.

Martins, J. E., E. Ruigrok, D. Draganov, A. Hooper, R. F. Hanssen, R. S. White, and H. Soosalu, 2019, Imaging Torfajökull's Magmatic Plumbing System with Seismic Interferometry and Phase Velocity Surface Wave Tomography: *Journal of Geophysical Research: Solid Earth*, 124, 2920–2940.

Montgomery, S. L., J. C. Mullarky, M. W. Longman, W. M. Colleary, and J. P. Rogers, 1998, Mississippian "Chat" Reservoirs, South Kansas: Low-Resistivity Pay in a Complex Chert Reservoir: *AAPG Bulletin*, 82, 187–205.

Nakata, N., L. Gualtieri, and A. Fichtner (Eds.), 2019, *Seismic Ambient Noise*: Cambridge University Press.

Nakata, N., R. Snieder, and M. Behm, 2014, Body-wave interferometry using regional earthquakes with multidimensional deconvolution after wavefield decomposition at free surface: *Geophysical Journal International*, 199, 1125–1137.

Nakata, N., J. P. Chang, J. F. Lawrence, and P. Boué, 2015, Body wave extraction and tomography at Long Beach, California, with ambient-noise interferometry: *Journal of Geophysical Research: Solid Earth*, 120, 1159–1173.

Nakata, N., R. Snieder, T. Tsuji, K. Larner, and T. Matsuoka, 2011, Shear wave imaging from traffic noise using seismic interferometry by cross-coherence: *Geophysics*, 76, no. 6, SA97-SA106.

Nishitsuji, Y., C. A. Rowe, K. Wapenaar, and D. Draganov, 2016, Reflection imaging of the Moon's interior using deep-moonquake seismic interferometry: *Journal of Geophysical Research E: Planets*, 121, 695–713.

Olivier, G., F. Brenguier, M. Campillo, R. Lynch, and P. Roux, 2015, Body-wave reconstruction from ambient seismic noise correlations in an underground mine: *Geophysics*, 80, no. 3, KS11–KS25.

Polychronopoulou, K., A. Lois, and D. Draganov, 2020, Body-wave passive seismic interferometry revisited: mining exploration using the body waves of local microearthquakes: *Geophysical Prospecting*, 68, 232–253.

Prieto, G. A., J. F. Lawrence, and G. C. Beroza, 2009, Anelastic Earth structure from the coherency of the ambient seismic field: *Journal of Geophysical Research: Solid Earth*, 114, B07303.

Ratre, P., and M. Behm, 2021, Imaging the deep crustal structure of central Oklahoma using stacking and inversion of local earthquake waveforms: *Journal of Geophysical Research: Solid Earth*, 126, e2020JB021368

Riahi, N., G. Bokelmann, P. Sala, and E. H. Saenger, 2013, Time-lapse analysis of ambient surface wave anisotropy: A three-component array study above an underground gas storage: *Journal of Geophysical Research: Solid Earth*, 118, 5339–5351.

Roux, P., K. G. Sabra, P. Gerstoft, W. A. Kuperman, and M. C. Fehler, 2005, P-waves from cross-correlation of seismic noise: *Geophysical Research Letters*, 32, 1–4.

Ruigrok, E., 2014, Receiver-pair seismic interferometry applied to body-wave USArray data: *Geophysical Journal International*, 198, 895–905.

Ruigrok, E., X. Campman, and K. Wapenaar, 2011, Extraction of P-wave reflections from microseisms: *Comptes Rendus - Geoscience*, 343, 512–525.

Saygin, E., P. R. Cummins, and D. Lumley, 2017, Retrieval of the P wave reflectivity response from autocorrelation of seismic noise: Jakarta Basin, Indonesia: *Geophysical Research Letters*, 44, 792–799.

Shapiro, N. M., and M. Campillo, 2004, Emergence of broadband Rayleigh waves from correlations of the ambient seismic noise: *Geophysical Research Letters*, 31, L07614.

Uemura, M., Y. Ito, K. Ohta, R. Hino, and M. Shinohara, 2018, Spatio-temporal changes in the seismic velocity induced by the 2011 Tohoku-Oki earthquake and slow slip event revealed from seismic interferometry, using ocean bottom seismometer's records: *Progress in Earth and Planetary Science*, 5, 87.

Vidale, J. E., 1986, Complex polarization analysis of particle motion: *Bulletin of the Seismological Society of America*, 76, 1393–1405.

Wapenaar, K., E. Slob, R. Snieder, and A. Curtis, 2010b, Tutorial on seismic interferometry: Part 2 - Underlying theory and new advances: *Geophysics*, 75, no. 5, 75A211-75A227.

Wapenaar, K., D. Draganov, R. Snieder, X. Campman, and A. Verdel, 2010a, Tutorial on seismic interferometry: Part 1 - Basic principles and applications: *Geophysics*, 75, no. 5, 75A195-75A209.

Watney, W. L., 2014, Wellington, Kansas CO2 Sequestration Monitoring, International Federation of Digital Seismograph Networks. https://doi.org/10.7914/SN/ZA_2014, accessed 5 October 2020

Watney, W. L., W. J. Guy, A. P. Byrnes, and A. Byrnes, 2001, Characterization of the Mississippian chat in south-central Kansas: *AAPG Bulletin*, 85, 85–113.

Zhou, W., and H. Paulssen, 2017, P and S Velocity Structure in the Groningen Gas Reservoir from Noise Interferometry: *Geophysical Research Letters*, 44, 11,785-11,791.

Zhou, W., and H. Paulssen, 2020, Compaction of the Groningen gas reservoir investigated with train noise: *Geophysical Journal International*, 223, 1327-1337.

Chapter 3

Passive reflectivity imaging and near-surface V_p/V_s estimation after S-wave polarization filtering

3.1 Abstract

Ambient noise interferometry applied to surface recordings predominantly results in retrieval of surface waves. Thereby making interferometric body wave retrieval by passive seismic recordings difficult. Although large-N arrays offer the advantage of using offset- and azimuth-based processing methods to isolate body waves, such arrays are not always available due to financial and logistical constraints. On the other hand, interferometric methods have been used to retrieve P-waves but very few studies have applied such methods for S-wave reflectivity imaging. Here, we use a single station polarization-based approach to detect S-waves for autocorrelation processing. The methodology is applied to a 3-component (3C) seismic monitoring dataset recorded at the Wellington oilfield

(Kansas, US). Autocorrelations of the retrieved S-wave dataset are interpreted for shallow (< 1 km) subsurface reflectivity. Additionally, we also utilize the P-wave reflectivity results from a previous study in the same area to estimate a V_p/V_s ratio of the shallow sedimentary column. The results are validated by comparison with log data measurements at a well. Our results suggest that data preselection prior to autocorrelation processing can enhance passive S-wave reflectivity imaging. Local seismic networks deployed for monitoring fluid injections and geothermal operation are usually sparse and irregular. This single station processing approach can find use with data recorded at such arrays. The methodology can find potential use in timelapse monitoring of fluid injection or extraction operations in reservoirs.

3.2 Introduction

Ambient noise interferometry is a well-established method at a wide range of scales from continental (e.g., Shapiro and Campillo, 2004; Bensen et al., 2007, Lin et al., 2008, Ekstrom, 2014; Haned et al., 2016) to local scales (Behm et al., 2014; Chang et al., 2016; Jia and Clayton, 2021). The technique has now been applied to image complex systems such as volcanic plumbing (Martins et al., 2019), geyser plumbing (Wu et al., 2021) and glacier flow (Sergeant et al., 2020). These applications generally retrieve surface wave energy. However, interferometric body-wave retrieval is still challenging due to dominance of surface-wave in ambient noise recordings. Several studies overcome this problem by using large-N

seismic networks (Draganov et al., 2009; Boué et al., 2013 – double beamforming; Lin et al., 2013 – core phases; Ruigrok, 2014; Nakata et al., 2015) that offer the possibility of using array-based processing. However, large deployments for the purpose of continuous ambient noise recording are rare. In such cases a single-station processing method, namely autocorrelation (AC), can be used to retrieve body waves reflected at subsurface structures.

Claerbout (1968) established that the zero-offset reflection response of a ‘layer cake’ earth can be approximated by the autocorrelation (AC) response of a near-vertically incident plane wave. Since then, ambient noise AC has been used to image deep crustal (Tibuleac and von Seggern, 2012; Kennet, 2015) and shallow structures (Saygin et al., 2017; Romero and Schimmel, 2018). However, the scarcity of vertically incident body waves in ambient noise recordings limits its use in AC imaging. This constraint can be overcome by selecting near-vertical body waves before AC processing. One approach uses teleseismic signals (Abe et al., 2007; Pham and Tkalcic, 2018; Wang et al., 2020) which have nearly vertical body wave arrivals from distant earthquakes. Another approach utilizes local or regional earthquakes in areas hosting high rates seismicity (e.g., mining, wastewater injection). Polychronopoulou et al. (2018) use near-vertical body wave arrivals from local microearthquakes. Dangwal and Behm (2021) use a polarization filter to extract near-vertical P-waves from continuous ambient noise recordings. Selecting near-vertically arriving body wave results in a body-wave rich dataset

much smaller in size than the continuous ambient noise recording which reduces the computational cost of AC.

Within the domain of body wave AC studies, the available literature generally focuses on P-wave retrieval, and only a few researchers successfully extract S-waves (e.g., Tibuleac and von Seggern, 2012; Pham and Tkalcic, 2018; Polychronopoulou et al., 2020). In this study, we develop a polarization-based S-wave preselection filter and subsequently compute AC for the selected steeply incident S-waves. Interpretation of S-wave reflectivity from AC is difficult because S-waves undergo an incident angle dependent phase rotation during reflection. We model the ray propagation to estimate the S-wave arrival incidence angle and the phase rotation before structural interpretation of the autocorrelograms. Additionally, we use the P-wave reflectivity results from Dangwal and Behm (2021) that apply a P-wave polarization filter to the same dataset. Using the P- and S-wave reflection time we estimate the ratio of the P- and S-wave velocities (V_p/V_s) in the shallow subsurface. V_p/V_s ratio can be of interest in a variety of settings for understanding lithology, fluid saturation, fractures, and porosity (Mavko et al., 2009). V_p/V_s estimation have been used to study ice properties in Antarctica ice sheet (Pham and Tkalcic, 2018) and Alpine glaciers (Sergeant et al., 2020). Lin (2020) demonstrates the correlation between of V_p/V_s and fluid injection and extraction at a geothermal field. Near-surface V_p/V_s is associated

with earthquake ground-motion amplification (Yang and Sato, 2000; Berg, 2021) and is thus useful for seismic hazard assessment.

Lastly, we validate our structural reflections and the estimated Vp/Vs ratio with the data available from a nearby drilled and logged well.

3.3 Study area and data

The data used in this study was acquired at the Wellington oil field (southcentral Kansas, US) by a local seismic array deployed by Kansas Geological Survey (network code ZA; Watney, 2014) between July 2014 and March 2018. The array (Figure 1) has a scattered arrangement of 15 Sercel L-22 3C short-period sensors (corner frequency of 2Hz) recording at 200 samples per second. The array covers $\sim 5 \text{ km}^2$ area surrounding an injection well (KGS 2-32) with $\sim 600 \text{ m}$ interstation distance. The objective of the deployment was to monitor injection induced seismicity during secondary (waterflooding) and tertiary (CO₂ injection in 2016) enhanced oil recovery operations (Holubnyak et al., 2017). Well logs from the injection well were also available for benchmarking the body-wave reflectivity and Vp/Vs ratio results.

Although injection-induced seismicity in Oklahoma (Ellsworth, 2013) is a contributor of the body waves recorded at the Wellington array, surface waves from local anthropogenic sources (traffic, oil field machinery, etc.) dominate the ambient

noise data. A large majority of these events have sub-basement hypocenters (mean depth of ~ 5 km). Based on a recently proposed crustal velocity model of Oklahoma (Ratre and Behm, 2021), seismic energy originating from such a sub-basement source propagates as diving waves in the basement and arrives with steep raypath-incidence angle ($< 30^\circ$) at epicentral distances > 100 km (Dangwal and Behm, 2021).

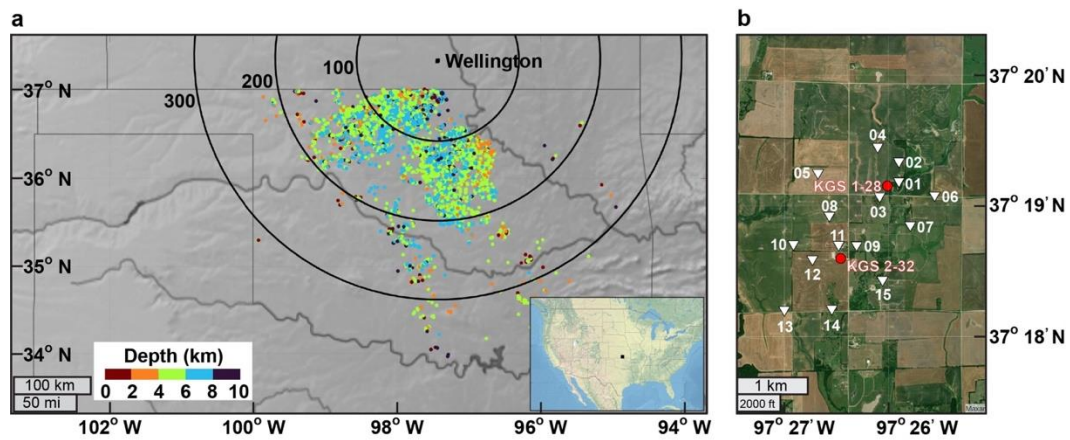


Figure 3.1. (a) Map of Oklahoma showing earthquake events (colored by hypocentral depth) from a regional seismic catalog for the recording period (2014 – 2018). Concentric circles represent distance in kilometers from the Wellington oil field. (b) Map of with the local seismic stations (white triangles) used in this study and drilled wells KGS 2-32 and KG 1-28 (red circles).

3.4 Methods

AC processing of vertically incident wavefield recordings can retrieve the zero-offset reflection response of the subsurface structure. However, the presence of surface waves and non-vertically incident arrivals can lead to spurious signals in the AC reflectivity response rendering it difficult to interpret. AC can also be considered as single-station interferometry with the aim to extract surface-related multiples from the ambient noise field, and thus is also applicable to retrieve shear wave reflectivity from S-wave fields. This study aims to improve shear-wave reflectivity retrieval from AC by selecting near-vertical incident S-waves from the continuous long-term recordings.

3.4.1 S-wave preselection using polarization filtering

Polarization analysis of the 3C seismic data can be used to evaluate the state of particle motion induced by the seismic waves at the receiver (Jurkevics, 1988; Baillard et al. 2014, Behm et al. 2020). Body waves are linearly polarized with particle motion along a single direction (P-waves – longitudinal, S-waves – transverse), whereas surface Rayleigh waves are planar polarized. The polarization parameter ‘linearity’ quantifies the degree of linearity of the seismic energy. Another parameter ‘polarization-incidence’ is the dip angle of the dominant particle motion direction measured from the vertical. This is different from ‘raypath-

incidence' which is the dip angle of the ray arriving at the receiver. It is noted that for the linearly polarized P-waves both these terms denote the same quantity.

Dangwal and Behm (2021) proposed a polarization filter to identify steeply incident P-wave energy in passive recordings using linearity and polarization-incidence. Here, we develop a similar approach for extracting S-waves. Although S-waves are linearly polarized, the calculated linearity value is generally not a clear indicator of S-wave arrival because of: (1) low signal to noise ratio (SNR) of the horizontal component recordings, and (2) superposition with P-wave coda, near-surface scattering, and phase conversions. Moreover, it is difficult to differentiate between steeply incident S-waves and ambient surface waves solely based on polarization-incidence criterion. Both these phases have dominant particle motion in the horizontal plane and therefore have similar polarization-incidence angles. To overcome this problem, we develop a more robust metric to differentiate S-wave from P-waves and ambient surface waves.

A covariance matrix

$$C(t) = \frac{1}{K} \begin{pmatrix} \sum_{i=1}^K N_i N_i & \sum_{i=1}^K N_i E_i & \sum_{i=1}^K N_i Z_i \\ \sum_{i=1}^K E_i N_i & \sum_{i=1}^K E_i E_i & \sum_{i=1}^K E_i Z_i \\ \sum_{i=1}^K Z_i N_i & \sum_{i=1}^K Z_i E_i & \sum_{i=1}^K Z_i Z_i \end{pmatrix} \quad (1)$$

is calculated for a 5-s sliding window of the 3C data centered at time t . In equation 1, K is the number of data samples in the 5-s window. Z, N, E are the waveform amplitude recorded on the vertical (Z) and the two horizontal components (N, E).

Eigenvectors ($\mathbf{V}_1(t), \mathbf{V}_2(t), \mathbf{V}_3(t)$) of the covariance matrix $C(t)$ represent the three orthogonal directions of particle motion. \mathbf{V}_1 corresponds to the direction of maximum polarization while \mathbf{V}_3 corresponds to the direction of minimum polarization. Polarization-incidence of \mathbf{V}_1 is defined as,

$$\theta(t) = 90^\circ - \tan^{-1} \left(\frac{V_{1,Z}(t)}{\sqrt{V_{1,E}^2(t) + V_{1,N}^2(t)}} \right), \quad (2)$$

following Vidale (1986). In equation 3, $V_{1,Z}, V_{1,N}, V_{1,E}$ are the components of \mathbf{V}_1 . For a vertically arriving S-wave the dominant polarization direction is in the horizontal plane, hence the polarization-incidence angle is 90° . While for a vertically arriving P-wave, with polarization along the raypath, the polarization-incidence angle is 0° .

In the frequency band of interest (> 1 Hz), S-waves from regional earthquakes have higher amplitudes than surface waves. The S-wave selection metric defined as,

$$S(t) = \left[\frac{\theta(t)}{90} \right]^n \frac{1}{2} \sum_{i=N,E} f_i(t) \cdot A_i(t), \quad (3)$$

combines three different parameters - incidence angle, frequency, and amplitude. In equation 3, $\theta(t)$ is the polarization-incidence angle of the V_1 eigenvector, $f_i(t)$ is the instantaneous peak frequency for the i -th component in a 5-s window centered at time t , A_i is the RMS amplitude of the i -th component calculated over a 5-s window centered at time t .

Figure 2 shows the S-wave pre-selection for a seismic data recorded during a regional earthquake. The P-wave first arrival is marked by low incidence angle for the V_1 eigenvector, implying near-vertical arrival. The high incidence angles for V_1 and V_2 eigenvectors correspond to the S-wave arrivals and the following surface waves imply dominant particle motion polarization in the horizontal plane. The bottom panel shows the S-wave metric calculated using the V_1 incidence angle, frequency, and amplitude. We identify the S-wave window using STA/LTA applied to the S-wave metric time-series. To further ensure selection of steeply incident S-waves we impose a cut-off of 65° (equivalent to 25° raypath incidence) on the incidence angle. After polarization filtering 1900 S-wave events with steep arrivals were selected from the continuous ambient noise dataset. These events are referred to as ‘S-wave preselection dataset’.

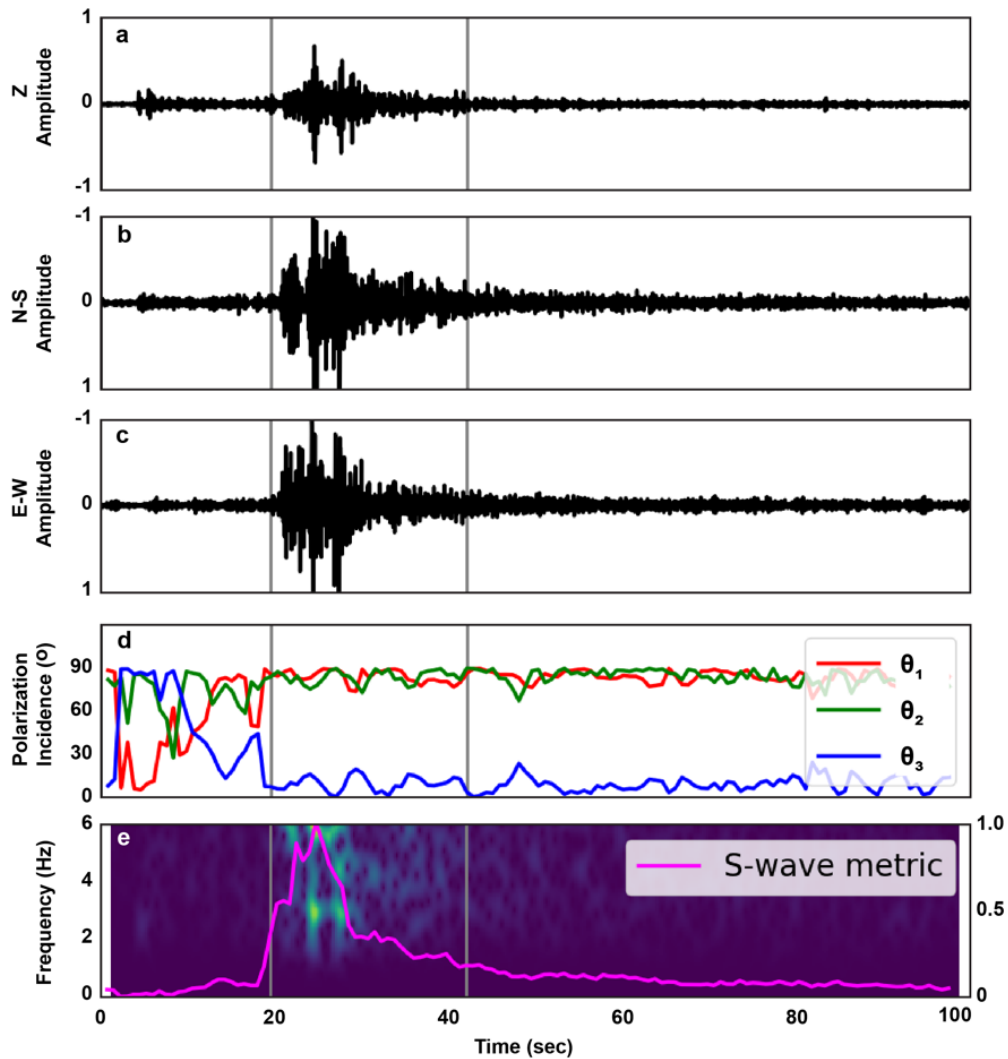


Figure 3.2. An example of S-wave polarization filtering applied to (a – c) 3C recordings. (d) Calculated polarization-incidence angles for the three eigen vectors. (e) Spectrogram of the seismic recording overlaid with the computed S-wave metric parameter discussed in Method section. Gray lines represent the time window selected by STA/LTA applied to the S-wave metric.

3.4.2 Preprocessing and autocorrelation (AC)

Before autocorrelating both the complete and the pre-selection datasets are preprocessed following the workflow described by Dangwal and Behm (2021). (1) Downsampling – Both the datasets are downsampled from 200 Hz to 100 Hz sampling frequency. (2) Segmentation – continuous ambient noise data is segmented into 6-hour long events. (3) Detrend and demean. (4) 5 Hz lowpass filtering to emphasize the frequency band dominated by shear waves. (5) Amplitude normalization using 0.2 s window automatic gain control.

We calculate the average AC response for the entire recording period by stacking the individual AC response for each segment in a dataset. AC is calculated with the objective of retrieving the free-surface multiples of the near-vertically transmitted body waves.

3.5 Results and discussions

3.5.1 Polarity of S-wave reflections retrieved by AC

Understanding the polarity of the retrieved reflection is essential for correctly interpreting the AC stack. AC derived reflection consists of peaks that result from the correlation of direct arrivals (P, S) and free surface multiples (PbP, SbS, etc.; Figure 3). Consequently, the polarity of the AC derived reflection is the

phase difference between the direct arrival and its free surface multiple. A free-surface multiple represents an arrival that undergoes two reflections – (i) at the free surface and (ii) at the impedance boundary. Thus, its phase is the sum of the phase rotation induced by the two reflections.

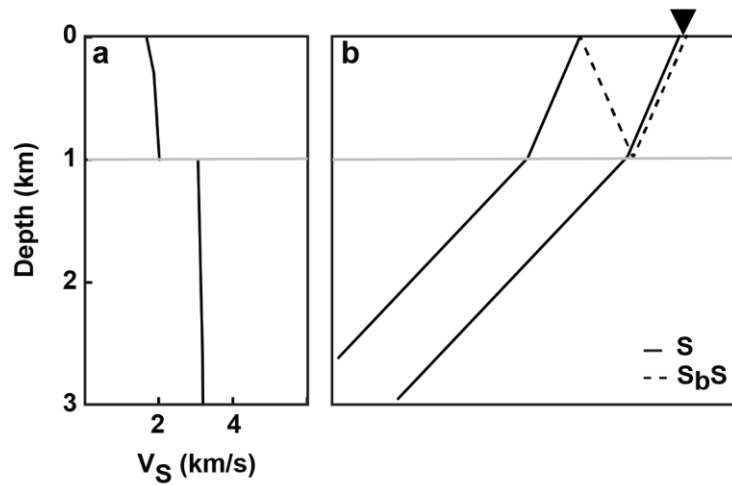


Figure 3.3. (a) A two layer V_S model with an impedance boundary at 1 km depth. S-wave raypaths showing direct arriving (S) and free surface reflection (S_bS) phases.

In case of P-wave AC, the reflection is interpreted as a negative amplitude peak (Saygin et al., 2017, Pham and Takalci, 2018; Dangwal and Behm, 2021) due to the fact the P-waves undergo a phase reversal at the free surface reflection and no rotation at the impedance boundary reflection. However, the phase of the S-wave reflection is dependent on the raypath-incidence angle and only a few studies analyze the polarity of S-wave reflections derived from AC. Pham and Tkalcic

(2018) autocorrelate vertically incident teleseismic coda waves to retrieve P- and S-wave reflections in the Antarctic icesheet. They postulate that both S-wave reflections and P-wave reflections have a negative polarity. Tibuleac and von Seggern (2012) interpret that the SmS (S Moho reflection) as a positive phase and the PmP (P Moho reflection) as a negative phase retrieved by ambient seismic AC.

To analyze the polarity and phase of S-wave reflections in our AC stack, we consider a two-layer velocity model (Figure 3a). Layer-1 represents an average velocity of the sedimentary column observed in the well log data. Layer-2 represents the basement and is based on a positive and smooth vertical gradient crustal velocity model of Oklahoma (Ratre and Behm, 2021; Figure 4a). First, we estimate the raypath-incidence angles of S-wave arrivals at the surface stations from a sub-basement (5 km depth) source. Sub-basement source depth is chosen to approximate the mean hypocentral depth of regional seismicity in Oklahoma which is the major source of body waves in our dataset. We then use ANRAY (Gaejwski and Psencik, 1987) to propagate rays in the velocity model and estimate the arrival raypath-incidence angle. The model predicts raypath-incidence angles in the range of $20^{\circ} - 30^{\circ}$ at epicentral distance of 100 – 300 km (Figure 4b, c). Next, we use a Zoeppritz solver (Aki and Rickards, 1980) to calculate the complex reflection coefficients for the S-wave reflection at the free-surface and at the impedance boundary over the predicted raypath-incidence angle range (Figure 5). In this range the S-waves, unlike P-waves, do not reverse polarity during the free-surface

reflection as is indicated by the 0 phase of the complex reflection coefficient. In the same raypath-incidence angle range, the impedance boundary reflections accounts for a phase rotation ($0^\circ - 45^\circ$) but not a phase reversal. Hence, for the interpretation we assume that the AC-retrieved S-wave reflection has a positive phase.

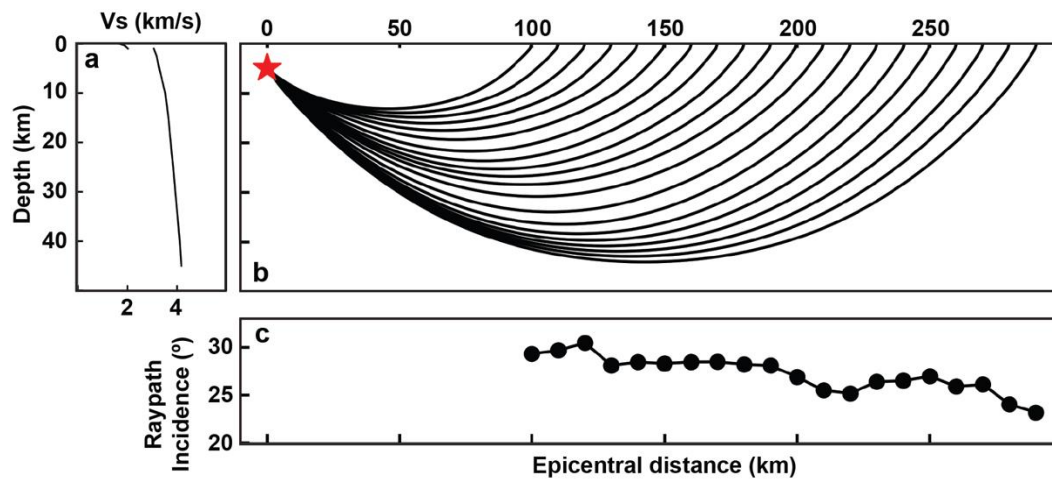


Figure 3.4. (a) The two layer V_s model shown in Figure 3 down to 50 km depth. (b) Direct S-wave raypaths emanating from a sub-basement source (red star). (c) Calculated raypath incidence angles for the direct S-wave arrivals at epicentral distances 100 – 290 km.

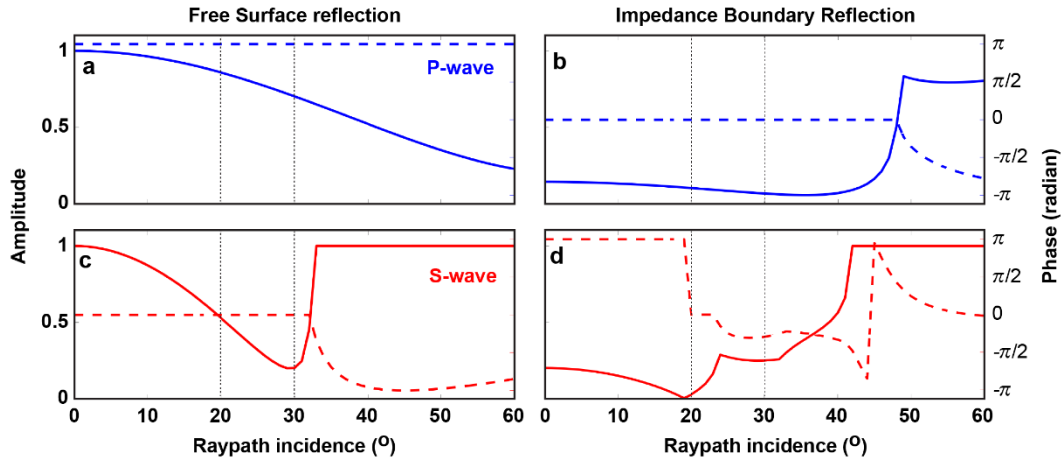


Figure 3.5. Complex reflectivity computed from Zoeppritz equations for a P-wave reflection at (a) the free surface and at (b) an impedance boundary in a 2-layer model. Similarly for an S-wave at (a) the free surface and at (b) an impedance boundary. Solid lines (blue, red) represent the magnitude (modulus) of the complex reflection coefficient. Dashed lines (blue, red) represent the phase of the complex reflection coefficient.

3.5.2 Interpretation of structural reflections

We compare the AC stacks of the two datasets (ambient noise dataset, S-wave preselection dataset) after band pass filtering in the 1 – 5 Hz range (Figure 6). To suppress the influence of the zero-lag peak, the AC stacks are top-muted at 0.2 s. For the ambient noise dataset, the horizontal component AC stacks (Figure 6 b, c) are incoherent, while the vertical component AC stack (Figure 6a) shows coherent phases in the 0.2 s – 0.6 s interval. Although the prominent negative phase

at 0.45 s may be a P-wave reflection, we refrain from interpreting the ambient noise AC stack due to dominance of surface waves in the dataset.

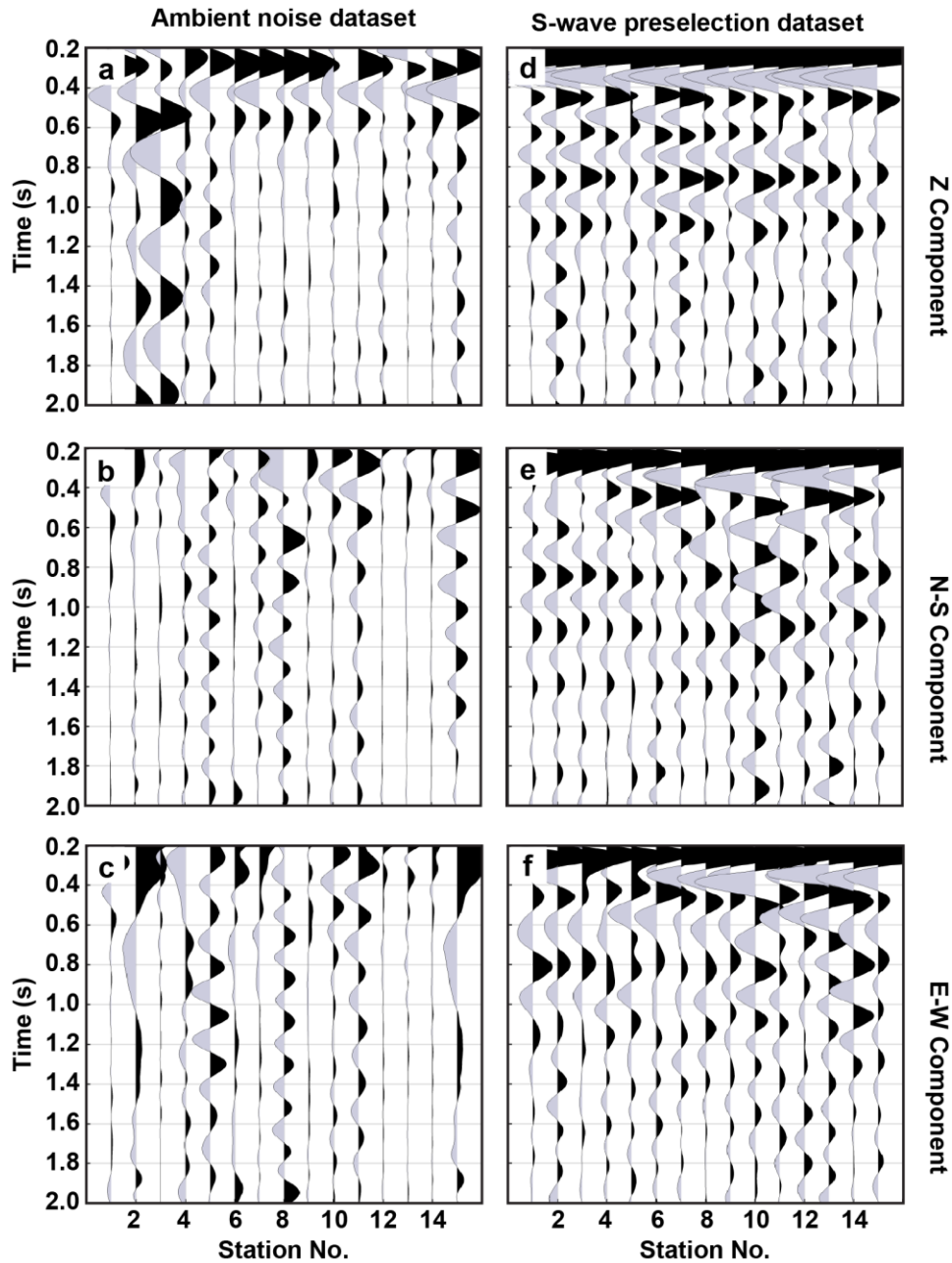


Figure 3.6. Comparison of the AC stacks computed from the (a – c) complete dataset and the (d – f) preselection dataset at all three components

Forward modeling discussed in the previous section suggests the presence of sub-vertical arrivals in the S-wave preselection dataset. This implies that the direct S- waves amplitudes and their free surface multiples are also projected on to the vertical component. We therefore expect S-wave reflection on all 3 components as is observed on the AC stacks (Figure 6 d-f). The horizontal component AC stacks show a lower signal-to-noise ratio (SNR) and lateral coherency, likely due to the high sensitivity of the horizontal components to the surface waves from local noise sources. Nonetheless, the S-wave preselection AC stacks shows several coherent phases in the 0.2 s – 1.2 s interval. With the objective of interpreting the S-wave structural reflections, we focus only on the positive phases in this interval. Particularly those are the coherent phases at approximately 0.85 s and 1.1 s which are observed on all components. Another consequence of the sub-vertically incident S-waves is the S-to-P phase conversion at impedance boundaries in the subsurface. A phase at ~0.35 s appears on all 3 components of the S-wave AC stack with different levels of coherency. The fact that this phase is clearer and more coherent on the vertical component further suggests the existence of S-to-P conversions. The likely influence of phase conversions and their reflections in the AC stack prevents us from interpreting the very shallow (< 0.6 s) reflectivity structure.

To further validate the presence of structural reflections in the S-wave preselection dataset, we compare the AC stacks with well logs from KGS 1-32 well. To facilitate the comparison in time domain, we convert the logs from depth-to-

time using the shear velocity log. We also compute an elastic impedance log to justify the retrieval for reflections from high-impedance interfaces. Before comparison with the logs, S-wave preselection AC stacks are post-processed to enhance the lateral continuity and strength of reflection phases. Eigenimage reconstruction (Freire and Ulrych, 1988) is used to improve the lateral continuity of the perceived reflectors. Since our seismic network has a small spatial spread ($\sim 5 \text{ km}^2$), minor temporal variations in the retrieved reflectivity are likely due to local site effects (e.g., surface noise sources in the vicinity of individual sensors) unrelated to the subsurface structure. To enhance the amplitudes of the deeper reflections, the retrieved amplitudes are scaled using an AGC filter.

Comparison with the well data suggests that AC retrieves reflections from two high impedance contrast interfaces. The 0.85 s and 1.1 s phases correspond to the LeCompton top and Kansas City top reflectors. However, the low SNR of the east-component results in poor retrieval of the shallower LeCompton reflector. A positive phase in 1.3 s – 1.5 s interval that emerged after postprocessing aligns with the Arbuckle top reflector. We do not attempt to interpret it as a reflection as this phase is not discernable in the raw AC stacks and lacks lateral continuity.

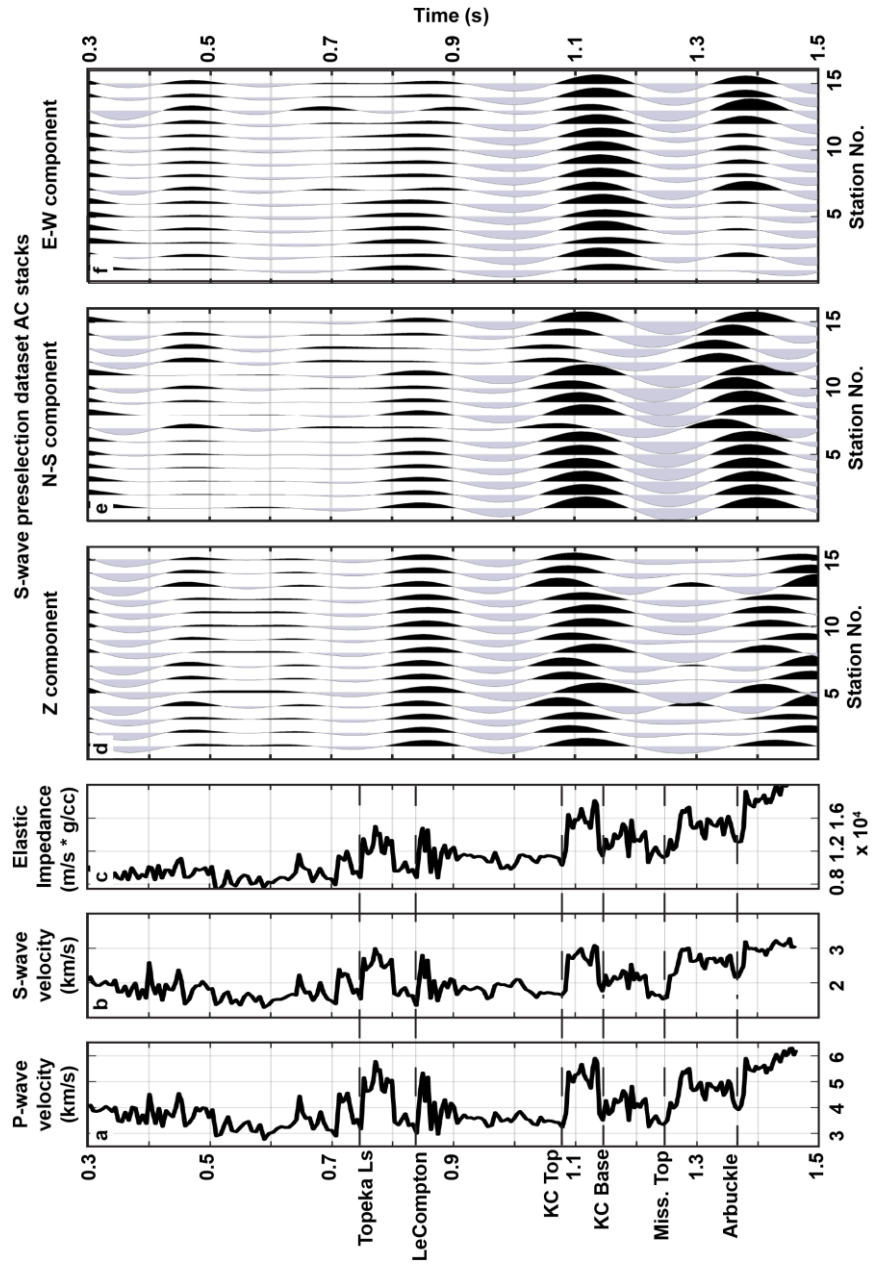


Figure 3.7. (a) sonic log, (b) shear-wave log, (c) computed elastic impedance log from KGS 1-32 well. Well logs are compared with AC stacks computed from S-wave preselection dataset. AC stacks are band passed in 1 – 5 Hz and eigenimage reconstructed to enhance lateral continuity of retrieved phases on (d) vertical component, (e) north-south component, (f) east-west component.

3.5.3 P-reflectivity and Vp/Vs estimation

Estimation of Vp/Vs ratio in the shallow subsurface requires P-reflectivity in addition to the S-reflectivity retrieved in the previous sections. A previous study (Dangwal and Behm, 2021) performed on the same dataset extracted near-vertical P-wave arrivals using a polarization filter. The study also retrieved P-wave reflections in the 5 – 10 Hz frequency band using vertical (Z) component AC. It is noted that the P-wave reflection time for the Vp/Vs calculations in the following discussion are based on the Z-component P-wave AC stack reported by Dangwal and Behm (2021). The S-wave reflection time are picked on the S-wave preselection AC stacks (Z-, N-, E-components). Due to the sub-vertical nature of the retrieved S-waves, reflection picking is done on all three components. The retrieved S-wave AC traces are rotated by 45° to compensate for the reflection-induced phase rotation of the sub-vertical arrivals.

Assuming homogeneity, the Vp/Vs ratio in the medium is estimated as the ratio of S- and P-waves reflection times from an underlying interface as,

$$\frac{V_p}{V_s} = \frac{TWT_S}{TWT_P}, \quad (4)$$

where TWT is the two-way travel time for reflected body-waves. However, the low frequency band of the retrieved reflections (1-5 Hz for S-waves, 5-10 Hz for P-waves) limits the temporal resolution and leads to uncertainties in the reflection

time picks. The accuracy of the Vp/Vs estimation is constrained by the uncertainty in reflection time as follows,

$$\delta_{V_p/V_s} = TWT_S \cdot \delta_{TWT_P} + TWT_P \cdot \delta_{TWT_S}. \quad (5)$$

where δ_{V_p/V_s} , δ_{TWT_P} , δ_{TWT_S} denote the error bounds (or uncertainty) of Vp/Vs, TWT_p and TWT_s. Vp/Vs ratio is calculated at all the stations using TWT_s for the KC-top reflector picked on all three components (Figure 8 a – c). The mean Vp/Vs over all the stations is estimated as ~1.9 from the Z- and N-component TWT_s. A slightly larger estimate of ~1.96 on the E-component is due to the time delay in the KC-top TWT_s (Figure 7). Similarly, the outlier values estimated at a few stations (e.g., station 4) can be attributed to the TWT_s picks on the corresponding AC stacks. Overall, the estimated Vp/Vs of ~1.9 and the minimum and maximum error bounds are consistent with the well log derived Vp/Vs (Figure 8d).

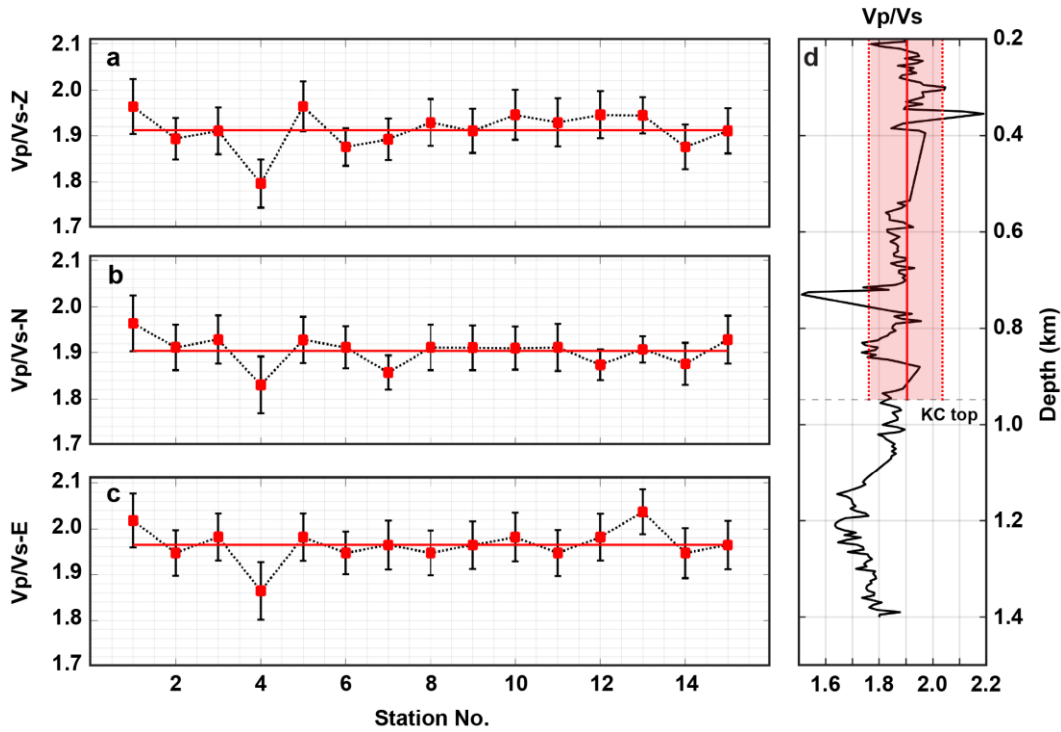


Figure 3.8. V_p/V_s estimated at all station using the KC-top using the S-wave reflection time retrieved on (a) Z-component, (b) N-component, (c) E-component AC stacks. Uncertainties in the V_p/V_s estimates are shown by error bars. Solid red line represents the average V_p/V_s for all stations. (d) Comparison of well log derived V_p/V_s ratio (black) and the average V_p/V_s ratio estimated on the N-component (red). Dotted red lines represent the minimum and maximum error bounds of the estimate.

3.6 Conclusions

Polarization filtering applied to 3C sensor data can be used to extract body waves from continuous ambient noise recordings. Here, we develop an S-wave filter using the polarization-incidence angle to select near-vertical arrivals at a

sparse local seismic network. Considering the modeled raypaths from regional seismicity in the area, we expect the selected S-wave arrivals in the $20^{\circ} - 30^{\circ}$ raypath-incidence angle range. The selected S-wave dataset is autocorrelated to retrieved structural reflections in the shallow subsurface. To our knowledge, no studies have discussed the phase of the S-wave reflections retrieved in ambient noise ACs. To correctly interpret the S-wave reflections we model the phase rotation for the S-wave free surface multiples using Zoeppritz equations. Although the resolution of S-wave reflections retrieved in this study are limited by the narrow frequency band (1 – 5 Hz) of the S-wave dataset, we are still able to image two structural reflectors in the shallow sedimentary layers (< 1km depth). Previous studies have relied on teleseismic or local seismic catalogues to retrieve body-wave reflections, but such catalogs are not always available. Our methodology extracts S-waves directly from ambient noise recordings and is applicable in areas where an earthquake catalog may not be available. Sensitivity of the V_p/V_s ratio to pore fluids in the subsurface makes combined S- and P-wave reflectivity a useful indicator for monitoring fluid injection and extraction operations in hydrocarbon and geothermal reservoirs.

Bibliography

Abe, S., Kurashimo, E., Sato, H., Hirata, N., Iwasaki, T., & Kawanaka, T. (2007). Interferometric seismic imaging of crustal structure using scattered teleseismic waves. *Geophysical Research Letters*, 34(19). <https://doi.org/10.1029/2007GL030633>

Allam, A. A., & Ben-Zion, Y. (2012). Seismic velocity structures in the southern California plate-boundary environment from double-difference tomography. *Geophysical Journal International*, 190(2), 1181–1196. <https://doi.org/10.1111/j.1365-246X.2012.05544.x>

Allam, A. A., Ben-Zion, Y., Kurzon, I., & Vernon, F. (2014). Seismic velocity structure in the Hot Springs and Trifurcation areas of the San Jacinto fault zone, California, from double-difference tomography. *Geophysical Journal International*, 198(2), 978–999. <https://doi.org/10.1093/gji/ggu176>

Baillard, C., Crawford, W. C., Ballu, V., Hibert, C., & Mangeney, A. (2014). An automatic kurtosis-based P-and S-phase picker designed for local seismic networks. *Bulletin of the Seismological Society of America*, 104(1), 394–409. <https://doi.org/10.1785/0120120347>

Behm, M., Leahy, G. M., & Snieder, R. (2014). Retrieval of local surface wave velocities from traffic noise - an example from the La Barge basin (Wyoming). *Geophysical Prospecting*, 62(2), 223–243. <https://doi.org/10.1111/1365-2478.12080>

Behm, M., Walter, J. I., Binder, D., Cheng, F., Citterio, M., Kulesa, B., Langley, K., Limpach, P., Mertl, S., Schöner, W., Tamstorf, M., & Weyss, G. (2020). Seismic characterization of a rapidly rising jökulhlaup cycle at the A.P. Olsen Ice Cap, NE-Greenland. *Journal of Glaciology*, 66(256), 329–347. <https://doi.org/10.1017/jog.2020.9>

Bensen, G. D., Ritzwoller, M. H., Barmin, M. P., Levshin, A. L., Lin, F., Moschetti, M. P., Shapiro, N. M., & Yang, Y. (2007). Processing seismic ambient noise data to obtain reliable broad-band surface wave dispersion measurements. *Geophysical Journal International*, 169(3), 1239–1260. <https://doi.org/10.1111/j.1365-246X.2007.03374.x>

Berg, E. M., Lin, F. C., Schulte-Pelkum, V., Allam, A., Qiu, H., & Gkogkas, K. (2021). Shallow Crustal Shear Velocity and V_p/V_s Across Southern California: Joint Inversion of Short-Period Rayleigh Wave Ellipticity, Phase Velocity, and Teleseismic Receiver Functions. *Geophysical Research Letters*, 48(15). <https://doi.org/10.1029/2021GL092626>

Boué, P., Roux, P., Campillo, M., & de Cacqueray, B. (2013). Double beamforming processing in a seismic prospecting context. *Geophysics*, 78(3), V101–V108. <https://doi.org/10.1190/GEO2012-0364.1>

Chang, J. P., de Ridder, S. A. L., & Biondi, B. L. (2016). High-frequency Rayleigh-wave tomography using traffic noise from Long Beach, California. *Geophysics*, 81(2), B1–B11. <https://doi.org/10.1190/GEO2015-0415.1>

Claerbout, J. F. (1968). Synthesis of a layered medium from its acoustic transmission response. *Geophysics*, 33(2), 264–269. <https://doi.org/10.1190/1.1439927>

Dangwal, D., & Behm, M. (2021). Interferometric body-wave retrieval from ambient noise after polarization filtering: Application to shallow reflectivity imaging. *Geophysics*, 86(6). <https://doi.org/10.1190/geo2020-0768.1>

Draganov, D., Campman, X., Thorbecke, J., Verdel, A., & Wapenaar, K. (2009). Reflection images from ambient seismic noise. *Geophysics*, 74(5). <https://doi.org/10.1190/1.3193529>

Ekström, G. (2014). Love and Rayleigh phase-velocity maps, 5–40 s of the western and central USA from USArray data. *Earth and Planetary Science Letters*, 402(C), 42–49. <https://doi.org/10.1016/j.epsl.2013.11.022>

Ellsworth, W. L. (2013). Injection-induced earthquakes. *Science*, *341*(6142). <https://doi.org/10.1126/science.1225942>

Freire, S. L. M., & Ulrych, T. J. (1988). Application of singular value decomposition to vertical seismic profiling. *Geophysics*, *53*(6), 778–785. <https://doi.org/10.1190/1.1442513>

Graves, R., Jordan, T. H., Callaghan, S., Deelman, E., Field, E., Juve, G., Kesselman, C., Maechling, P., Mehta, G., Milner, K., Okaya, D., Small, P., & Vahi, K. (2011). CyberShake: A Physics-Based Seismic Hazard Model for Southern California. *Pure and Applied Geophysics*, *168*(3–4), 367–381. <https://doi.org/10.1007/s00024-010-0161-6>

Haned, A., Stutzmann, E., Schimmel, M., Kiselev, S., Davaille, A., & Yelles-Chaouche, A. (2016). Global tomography using seismic hum. *Geophysical Journal International*, *204*(2), 1222–1236. <https://doi.org/10.1093/gji/ggv516>

Holubnyak, Y., Watney, W., Rush, J., Fazelalavi, M., & Wreath, D. (2017). Pilot Scale CO₂ EOR in Mississippian Carbonate Reservoir at Wellington Field in South-central Kansas. *Energy Procedia*, *114*, 6989–6996. <https://doi.org/10.1016/j.egypro.2017.03.1840>

Jia, Z., & Clayton, R. W. (2021). Determination of Near Surface Shear-Wave Velocities in the Central Los Angeles Basin with Dense Arrays. *Journal of Geophysical Research: Solid Earth*, 126(5). <https://doi.org/10.1029/2020JB021369>

Kennett, B. L. N. (2015). Lithosphere-asthenosphere P-wave reflectivity across Australia. *Earth and Planetary Science Letters*, 431, 225–235. <https://doi.org/10.1016/j.epsl.2015.09.039>

Lin, F. C., Moschetti, M. P., & Ritzwoller, M. H. (2008). Surface wave tomography of the western United States from ambient seismic noise: Rayleigh and Love wave phase velocity maps. *Geophysical Journal International*, 173(1), 281–298. <https://doi.org/10.1111/j.1365-246X.2008.03720.x>

Lin, F. C., Tsai, V. C., Schmandt, B., Duputel, Z., & Zhan, Z. (2013). Extracting seismic core phases with array interferometry. *Geophysical Research Letters*, 40(6), 1049–1053. <https://doi.org/10.1002/grl.50237>

Martins, J. E., Ruigrok, E., Draganov, D., Hooper, A., Hanssen, R. F., White, R. S., & Soosalu, H. (2019). Imaging Torfajökull's Magmatic Plumbing System with Seismic Interferometry and Phase Velocity Surface Wave Tomography. *Journal of Geophysical Research: Solid Earth*, 124(3), 2920–2940. <https://doi.org/10.1029/2018JB016002>

Nakata, N., Chang, J. P., Lawrence, J. F., & Boué, P. (2015). Body wave extraction and tomography at Long Beach, California, with ambient-noise interferometry. *Journal of Geophysical Research: Solid Earth*, *120*(2), 1159–1173. <https://doi.org/10.1002/2015JB011870>

Phạm, T. S., & Tkalčić, H. (2018). Antarctic Ice Properties Revealed From Teleseismic P Wave Coda Autocorrelation. *Journal of Geophysical Research: Solid Earth*, *123*(9), 7896–7912. <https://doi.org/10.1029/2018JB016115>

Polychronopoulou, K., Lois, A., & Draganov, D. (2020). Body-wave passive seismic interferometry revisited: mining exploration using the body waves of local microearthquakes. *Geophysical Prospecting*, *68*(1), 232–253. <https://doi.org/10.1111/1365-2478.12884>

Ratre, P., & Behm, M. (2021). Imaging the Deep Crustal Structure of Central Oklahoma Using Stacking and Inversion of Local Earthquake Waveforms. *Journal of Geophysical Research: Solid Earth*, *126*(5). <https://doi.org/10.1029/2020JB021368>

Romero, P., & Schimmel, M. (2018). Mapping the Basement of the Ebro Basin in Spain With Seismic Ambient Noise Autocorrelations. *Journal of Geophysical Research: Solid Earth*, *123*(6), 5052–5067. <https://doi.org/10.1029/2018JB015498>

Ruigrok, E. (2014). Receiver-pair seismic interferometry applied to body-wave USArray data. *Geophysical Journal International*, 198(2), 895–905. <https://doi.org/10.1093/gji/ggu168>

Saygin, E., Cummins, P. R., & Lumley, D. (2017). Retrieval of the P wave reflectivity response from autocorrelation of seismic noise: Jakarta Basin, Indonesia. *Geophysical Research Letters*, 44(2), 792–799. <https://doi.org/10.1002/2016GL071363>

Sergeant, A., Chmiel, M., Lindner, F., Walter, F., Roux, P., Chaput, J., Gimbert, F., & Mordret, A. (2020). On the Green's function emergence from interferometry of seismic wave fields generated in high-melt glaciers: Implications for passive imaging and monitoring. *Cryosphere*, 14(3), 1139–1171. <https://doi.org/10.5194/tc-14-1139-2020>

Shapiro, N. M., & Campillo, M. (2004). Emergence of broadband Rayleigh waves from correlations of the ambient seismic noise. *Geophysical Research Letters*, 31(7). <https://doi.org/10.1029/2004GL019491>

Tibuleac, I. M., & von Seggern, D. (2012). Crust-mantle boundary reflectors in Nevada from ambient seismic noise autocorrelations. *Geophysical Journal International*, 189(1), 493–500. <https://doi.org/10.1111/j.1365-246X.2011.05336.x>

Vidale, J. E. (1986). Complex polarization analysis of particle motion. *Bulletin of the Seismological Society of America*, 76(5), 1393–1405.

Wang, C., Tauzin, B., Pham, T. S., & Tkalčić, H. (2020). On The Efficiency of P-Wave Coda Autocorrelation in Recovering Crustal Structure: Examples from Dense Arrays in the Eastern United States. *Journal of Geophysical Research: Solid Earth*, 125(12). <https://doi.org/10.1029/2020JB020270>

Wu, S. M., Lin, F. C., Farrell, J., Keller, W. E., White, E. B., & Hungerford, J. D. G. (2021). Imaging the Subsurface Plumbing Complex of Steamboat Geyser and Cistern Spring with Hydrothermal Tremor Migration Using Seismic Interferometry. *Journal of Geophysical Research: Solid Earth*, 126(4). <https://doi.org/10.1029/2020JB021128>

Yang, J., & Sato, T. (2000). Interpretation of Seismic Vertical Amplification Observed at an Array Site. *Bulletin of the Seismological Society of America*, 90.

Chapter 4

Imaging a paleovalley with passive seismic methods: Evidence for glacial carving of Unaweep Canyon (Colorado, US)

4.1 Abstract

High-resolution passive seismic imaging of shallow subsurface structures is often challenged by the scarcity of coherent body-wave energy in ambient noise recorded at surface stations. We show that autocorrelation (AC) of teleseismic P-wave coda extracted from just 1-month of continuous recording at 5 Hz geophones can overcome this limitation. We apply this method to investigate the longitudinal subsurface structure of Unaweep Canyon, a paleovalley in western Colorado (US) with complex evolution. Both fluvial and glacial processes have been proposed to explain the canyon's genesis and morphology. The teleseismic P-wave coda AC retrieves zero-offset reflections from the shallow (200 – 500 m depth) basement interface at 120 stations along a 5 km long profile. Additionally, we invert interferometrically retrieved surface wave dispersion for the shear-wave structure

of the sedimentary fill. Combined interpretation of these results and other geophysical and well data suggests an overdeepened basement geometry due to glacial processes.

4.2 Introduction

Ambient noise seismic interferometry (SI) is a well-established technique for shear wave velocity imaging at continental scale (Shapiro & Campillo, 2004; Bensen et al., 2007, Lin et al., 2008, Ekstrom et al., 2009), basin scale (Wang et al., 2019; Jia & Clayton, 2021; Cheng et al., 2021; Fu et al., 2022), and sub-kilometer scale (Hannemann et al., 2014; Sergeant et al., 2020; Wu et al., 2021). To directly image seismic impedance contrasts (reflectors) from ambient noise, autocorrelation (AC) has been applied for illuminating deep crustal structures (Tibuleac & Seggern, 2012; Kennet, 2015; Becker & Knapmeyer-Endrun, 2019). However, due to lack of well-defined and steeply incident body waves, only a few studies have used ambient noise AC for shallow targets (e.g., Saygin et al., 2017; Heath et al. 2018). Other studies have applied preprocessing of ambient noise to select body-waves from local seismicity (Dangwal & Behm, 2021) and local micro-earthquakes (Polychronopoulou et al., 2020) to improve shallow reflectivity retrieval from AC. An alternate approach uses teleseismic signals with near-vertical incidence to image deep crustal (Abe et al., 2007; Ruigrok & Wapenaar, 2012; Wang et al., 2020) and shallow structures (Pham & Tkalcic, 2017, 2018; Viens et al., 2022).

In this study, we apply passive seismic methods to image the sediment fill and the basement geometry along a 5 km long longitudinal section of an alpine valley. We take advantage of steeply incident teleseismic waveforms to extract shallow (< 500 m depth) basement reflections using AC, resulting in zero-offset P-wave reflectivity section along the profile. Furthermore, we use ambient noise SI to retrieve surface wave propagation in the same depth range. We then invert the frequency-velocity dispersion trends of these surface waves to obtain a 2D shear-wave velocity model. These results are interpreted in context with the existing well data and the crossing active seismic section.

4.3 Geologic setting

Unaweep Canyon is a ~ 70 km long, NE-SW-trending gorge that bisects the Uncompahgre Plateau of Colorado. A high-altitude divide (2142 m) within the canyon is the source of two underfit creeks – East Creek flowing northeast (towards Whitewater), where it joins the Gunnison River, and West Creek flowing southwest (towards Gateway) where it joins the Dolores River (Figure 4.1a). The canyon cuts through the Mesozoic strata and into Precambrian crystalline basement and hosts sedimentary fill of Quaternary and inferred pre-Quaternary provenance. Boreholes in the canyon have indicated at least 365 m thick sedimentary fill (Soreghan et al., 2007; Soreghan et al., 2022).

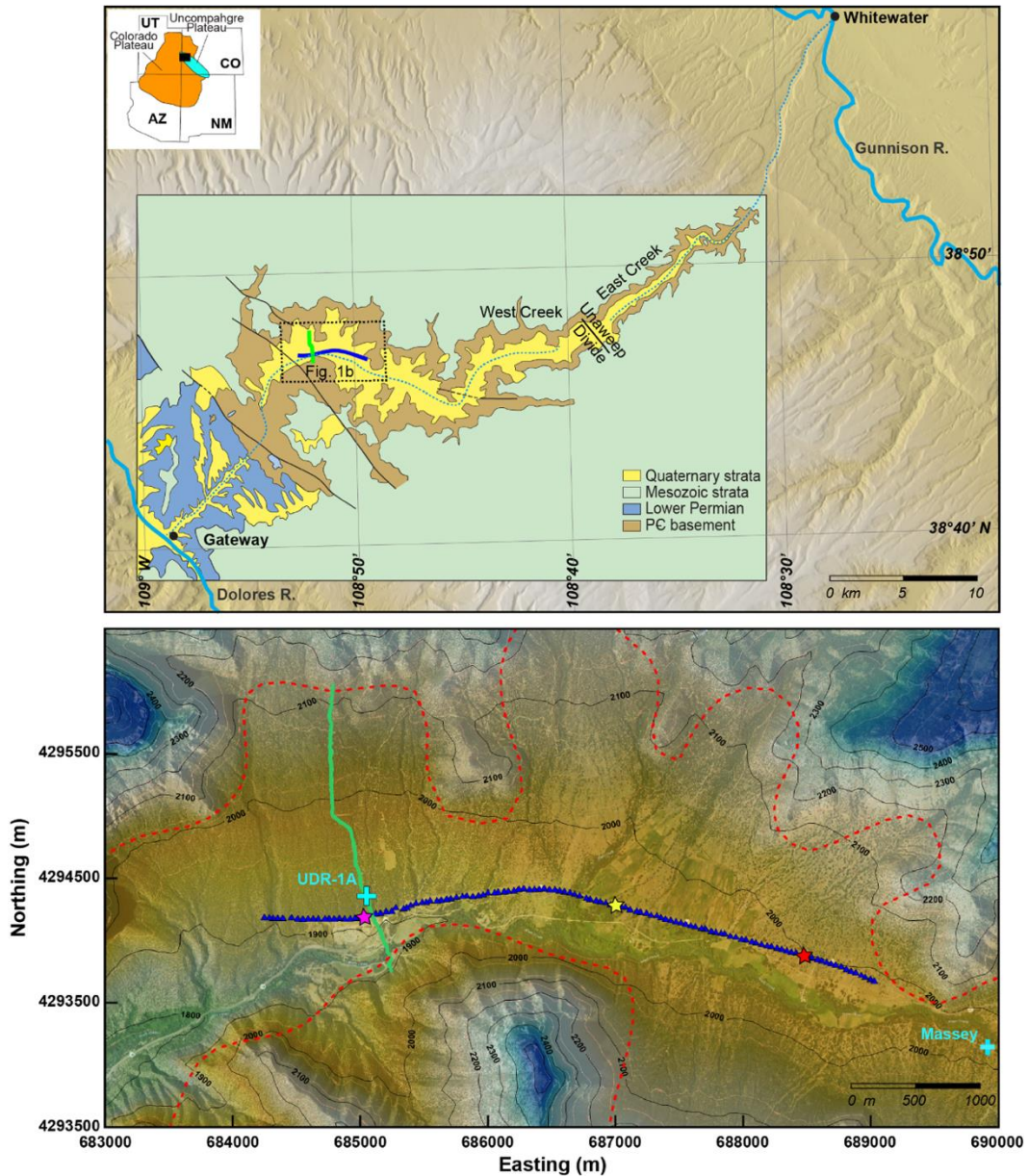


Figure 4.1: (a) Digital elevation model of Unaweep Canyon with overlaid geological map. Inset on the top-right shows the location of Unaweep Canyon on the Uncompahgre Plateau and Colorado Plateau. Box with dotted edges shows the location of Figure 4.1b. (b) Satellite map of the study area with elevation contours. Green line indicates the active seismic profile (2017). Blue line indicates the passive seismic profile (2020). Cyan crosses mark the location of wells - UDR-1A (2022), Massey (2004 – 2006). Red dashed line is the approximately mapped

interface of the basement outcrop and the sedimentary fill. The three stars along the passive profile give the location of the virtual source gathers shown in Figure 4.3.

The competing hypotheses for the formation of Unaweep Canyon are: (1) Cenozoic fluvial incision, (2) Cenozoic glacial incision, (3) late Paleozoic glacial incision and burial followed by Cenozoic fluvial exhumation. The widely accepted fluvial hypothesis proposes incision by the ancestral Gunnison River and/or ancestral Colorado River (e.g., Gannett, 1882; Lohman, 1961; Cater, 1966). However, many geomorphological attributes of the canyon are difficult to explain by an entirely fluvial genesis. A U-shaped cross-section is typically associated with glacial processes, while V-shaped cross-sections are linked to fluvial processes. In the context of Unaweep Canyon, the presence of the U-shapes in amphitheater-like side valleys along with hanging valleys and truncated spurs have been cited as evidence for recent (Quaternary) glacial origin (Cole & Young, 1983). However, the absence of Quaternary glacial deposits in the canyon and low elevations confound this claim. The third hypothesis positing formation by Paleozoic glaciation (Soreghan et al., 2007, 2008, 2014, 2015) is challenged by the fact that the Uncompahgre uplift of the ancestral Rocky Mountains (ARM) was situated in the equatorial zone during the late Paleozoic ice age (LPIA). Although Soreghan et al. (2008, 2014) suggested upland glaciation in low latitudes, climate models struggle to reproduce even this level of cooling (Soreghan et al., 2008).

Given the importance of determining the shape of the canyon for understanding its origin, several studies have attempted to assess the basement geometry using geophysical methods. Soreghan et al. (2008) demonstrated that a U-shaped basement cross-section best matches the gravity observations across the canyon relative to a V-shaped cross-section. PSTM imaging along a 2.5 km long transverse seismic reflection profile has revealed a U-shape buried valley floor (Patterson et al., 2021; Figure S4.5). More recently, a drilling expedition in February 2022 (well UDR-1A; Soreghan et al., 2022) struck basement at 365m depth.

4.4 Deployment and Data

A 5 km long section of highway CO-141 traversing Unaweep Canyon was chosen to deploy the passive seismic profile (Figure 4.1). This section lies in the western canyon, approximately 15 km east of Gateway (near the western mouth of the canyon). The section was chosen because (1) it intersects the previously mentioned active seismic profile acquired in 2017, (2) three drilled and partly cored wells are located nearby, and (3) a gravel quarry near the western end of the section as well as the highway itself act as a source of surface wave energy. 120 Fairfield MagSeis ZLand 3C nodes (5 Hz corner frequency) were deployed along this section with 40 m spacing. The nodes recorded continuously for a period of 35-days from 21st August to 25th September 2020 with a sampling rate of 250 Hz. The recorded

ambient noise is dominated by high-frequency (1-10 Hz) surface waves from traffic and quarry operations. Although this area and the Colorado Plateau in general are seismically quiet, induced seismicity caused by brine disposal injection operations at the Bureau of Reclamation's Paradox Valley Unit well (Block et al., 2021) is a potential source of body waves. However, most of the induced event detected by the Paradox Valley Seismic Network are low magnitude (< 1 Mw) with insufficient signal strength to be detected in our data (~ 54 km away). In addition to the ambient noise, 10 teleseismic earthquakes (magnitude > 6 ; Figure S4.6) with high signal-to-noise ratio are also present in our dataset.

4.5 Methods

The objective of this study has two complimentary aspects: (1) delineating the geometry of the buried basement interface, and (2) imaging the depth and velocity of the sedimentary fill. We use teleseismic coda wave AC for the first aspect. For the second aspect, we use ambient noise seismic interferometry (SI) to reconstruct dispersive surface waves travelling between the receivers, which are subsequently inverted for a 2D shear-wave velocity profile. The methods described in this section are applied to the vertical component data.

4.5.1 Teleseismic AC

Autocorrelation of the transmission response of a 1-D layered earth recorded at a surface receiver can be used to estimate the zero-offset reflection response (Claerbout, 1968). This has been established for vertically incident energy propagating from a deep source below the receiver. However, in the absence of a local source of vertically incident seismic energy, teleseismic waves from distant earthquakes can be used to achieve the same goal (Abe et al., 2007; Ruigrok & Wapenaar, 2012; Pham & Tkalcic, 2018; Viens et al., 2022). In order to minimize the influence of source-side multiples and complex source signatures of these strong events, we use the P-wave coda for AC processing. The presence of multiple receiver-side reflections in the scattered P-wave coda favors the retrieval of shallow reflectivity structure (Pham & Tkalcic, 2017).

To ensure validity of the near-vertical incidence assumption, we shortlist 10 teleseismic events in the epicentral distance range of $60^\circ - 95^\circ$ from a global catalog of large magnitude events (>6 magnitude) that occurred during the study period (August 2020 – September 2020; Figure S4.6). The P-wave first arrival times of these events at the Unaweep array are predicted using the IASP91 reference model (Kennet & Engdahl, 1991). We then define the P-wave coda for these events as a 50 s long time window starting 100 s after the first P arrival estimated by the reference model.

Preprocessing of the teleseismic coda waves includes: (1) Downsampling from 250 Hz recording rate to 50 Hz. (2) Detrend and demean. (3) 5 Hz low pass filtering to emphasize the frequency band dominated by the teleseismic coda while suppressing the local high frequency surface waves. (4) Automatic gain control (AGC) using a 0.1 s window length to normalize amplitudes from varying source strength. Spectral whitening is not applied during preprocessing because it results in a strong zero-lag peak in the AC response that masks the shallow reflectivity response. We calculate the average reflectivity response at a station by first autocorrelating each teleseismic coda wave event recorded at that station and then stacking the AC responses of each event (Figure 4.2). Similarity between the AC responses of individual teleseismic coda wave events suggests that the method retrieves the receiver-side structural reflections and is not related to the source signature. Moreover, any source-side multiples that may be present in the teleseismic coda waves are suppressed by the stacking process. The retrieved reflections have a negative phase due to the negative reflectivity coefficient (-1) for P-wave at the free surface. We, therefore, reverse the polarity of the AC response before interpreting it as a reflection.

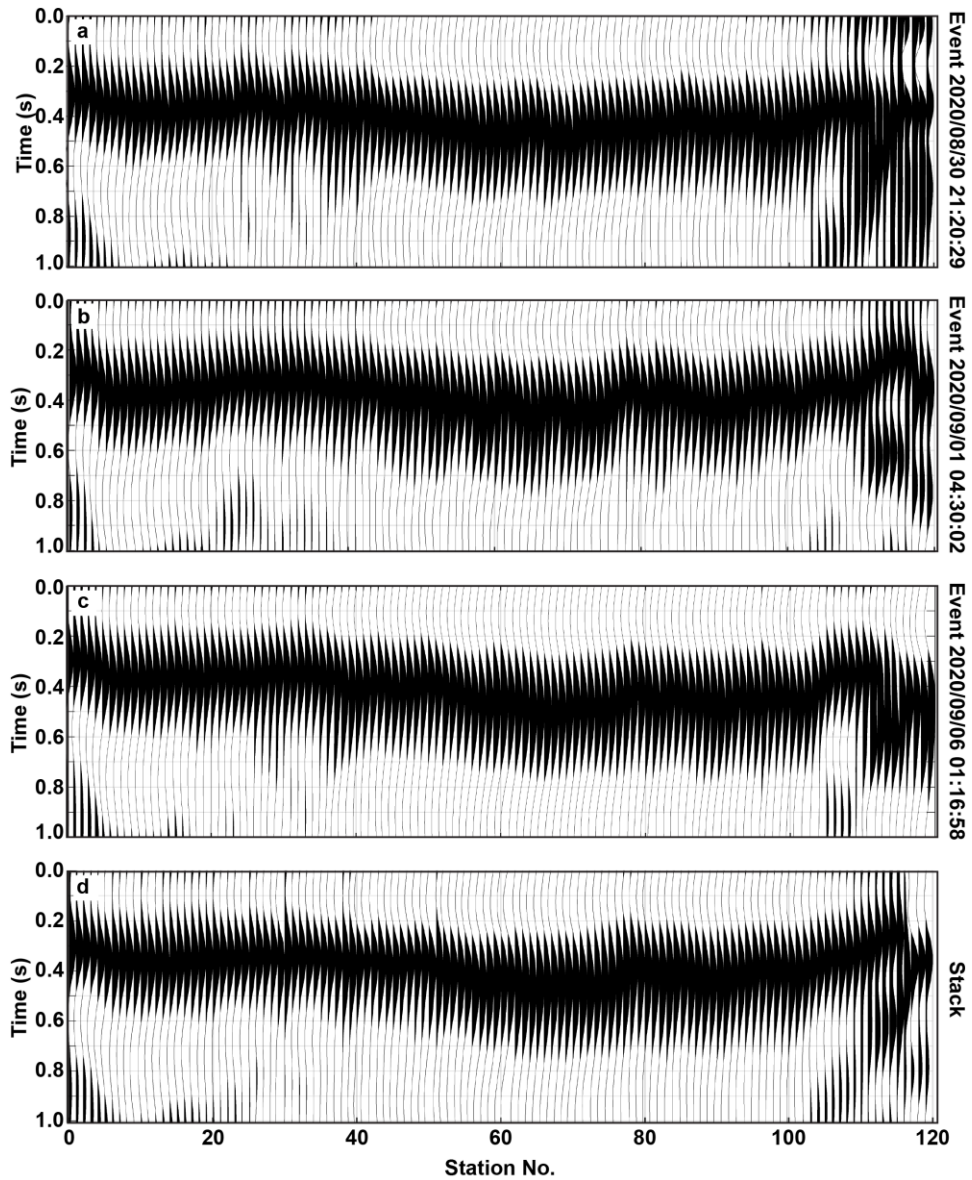


Figure 4.2: (a-c) Individual AC response of 3 teleseismic events. (d) Stacked AC response of 10-teleseismic events used in the study. No post-AC signal processing has been applied.

To strengthen the confidence in our AC-derived shallow basement reflectivity response, we also attempt to retrieve the Moho reflection. For this

purpose, AC is applied to the ballistic (first arrival) teleseismic phases. The results show a laterally coherent, strong phase at a TWT of ca. 15.5 s, which we interpret as the Moho reflection (Figure S4.7). This hypothesis is supported by analysis of COCORP active source reflection data in this part of the Colorado Plateau where the Moho reflection and corresponding depth were interpreted at 16 s TWT and 50 km, respectively (Hauser & Lundy, 1989).

4.5.2 Ambient noise seismic interferometry (SI) and 2D Vs Inversion

SI entails the cross-correlation of the seismic recordings at two receivers to estimate the virtual response recorded at one of the receivers due to a virtual source at the other receiver location (Wapenaar et al., 2010a). The retrieved virtual response (or interferogram) is thus an approximation of the medium's response to wave propagation between the receivers.

The continuously recorded data is segmented into 1-hour long windows before applying the preprocessing steps listed in the previous section. It is noted that here the surface waves in the < 5 Hz band are desirable for imaging the sedimentary fill down to approximately 500 m depth. We therefore low pass the ambient noise segments at 5 Hz. The cross-coherence method (Aki, 1957; Prieto et al., 2009; Wapenaar et al., 2010b) is used to calculate the interferograms. As this

method already includes spectral whitening, separate pre-whitening is not required. For a station pair, an interferogram is calculated for each 1-hour time segment. These interferograms are then phase-weighted stacked (Schimmel & Paulssen, 1997) to obtain an average interferogram for the station pair. Finally, all the station pair interferograms are sorted into 120 virtual source gathers (VSGs; Figure S4.8). A VSG emulates the seismic shot gather obtained from an active (explosive) source experiment conducted at a receiver location.

Due to strong contribution of ambient noise from local surface sources (traffic, machinery, etc.) and the application of a 5 Hz low pass filter, the VSGs are dominated by surface waves in the 1 – 5 Hz frequency band. Visual analysis of the VSGs indicates high signal-to-noise ratio in offset ranges up to 1000 m. We therefore limit the VSGs to 1000 m offset for further processing. Next, the VSGs are FK-filtered to suppress the zero-lag peak and the apparent low-velocity surface-wave reflections from the canyon walls. To derive a 2D S-wave velocity model along the profile, the pre-processed VSGs (Figure 4.3 a-c) are then subjected to a workflow similar to Socco et al. (2009). This approach is based on the MASW (multi-channel analysis of surface waves) technique and takes advantage of 2D multi-fold data, e.g., where the source-receiver geometry has a high degree of overlap. This is usually the case for ambient noise data collected along profiles where each receiver is turned into a virtual source. The processing steps include receiver-sorting and binning, dispersion image calculation via the SFK method

(Serdyukov et al., 2019), stacking of all dispersion images within each bin (Figure 4.3 d-f), semi-automatic extraction of Rayleigh-wave dispersion curves for each bin, and a joint and laterally constrained inversion of all dispersion curves. This more sophisticated procedure has been found to provide structurally similar but more detailed and robust results when compared to conventional methods such as phase-shift dispersion image calculation of individual VSGs and their spatially non-constrained linearized inversion (Xia et al., 1999) as well as application of the hybrid neighborhood inversion algorithm (Geopsy; Wathelet et al. 2004). The final result is a 2D shear-wave velocity model along the profile (Figure 4.4 a).

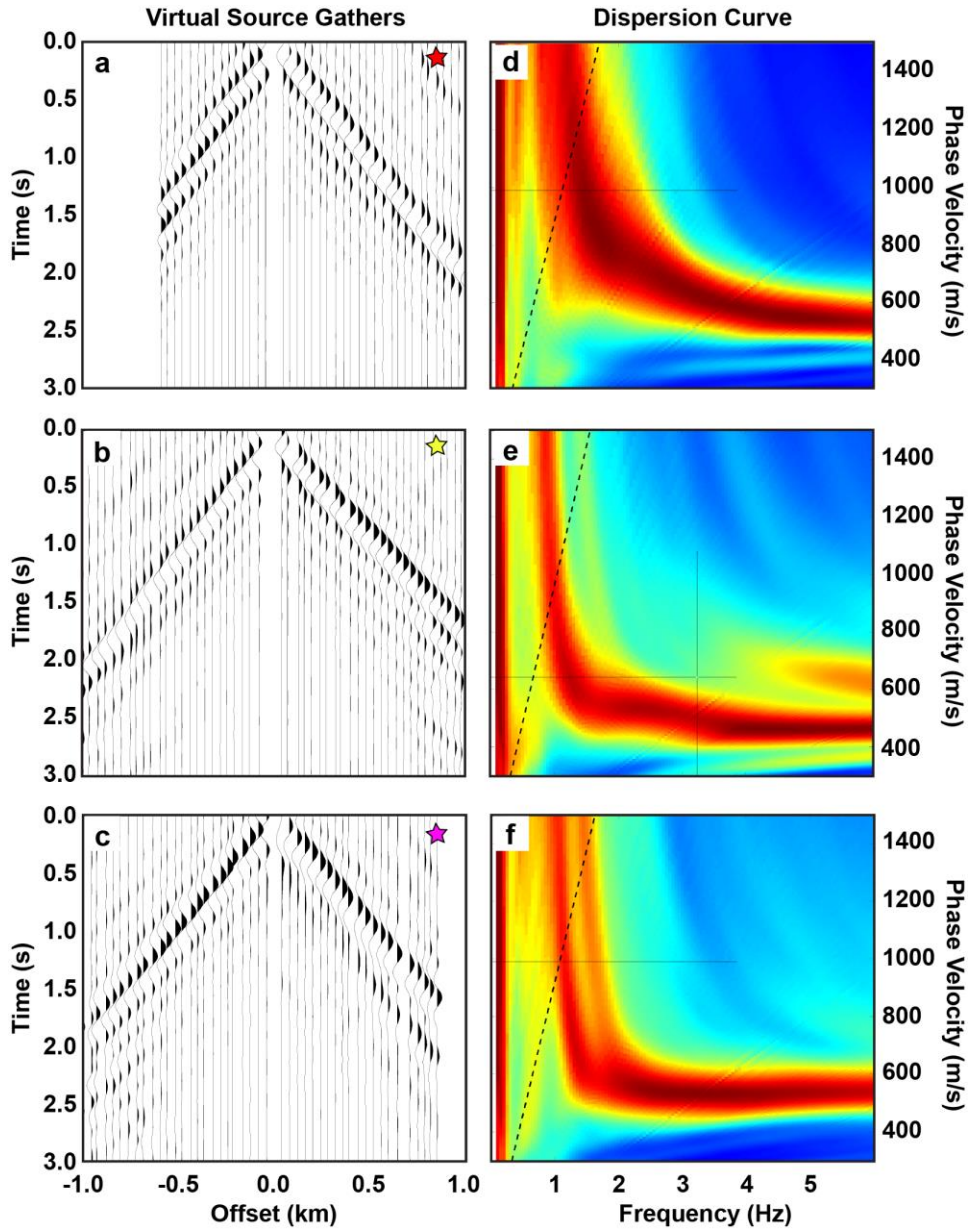


Figure 4.3: (a-c) F-K filtered VSGs with virtual sources located at 3 receiver locations marked with the same-colored stars in Figure 4.1b. (d-f) Stacked Rayleigh wave dispersion curves for bin locations corresponding to the same 3 receiver locations.

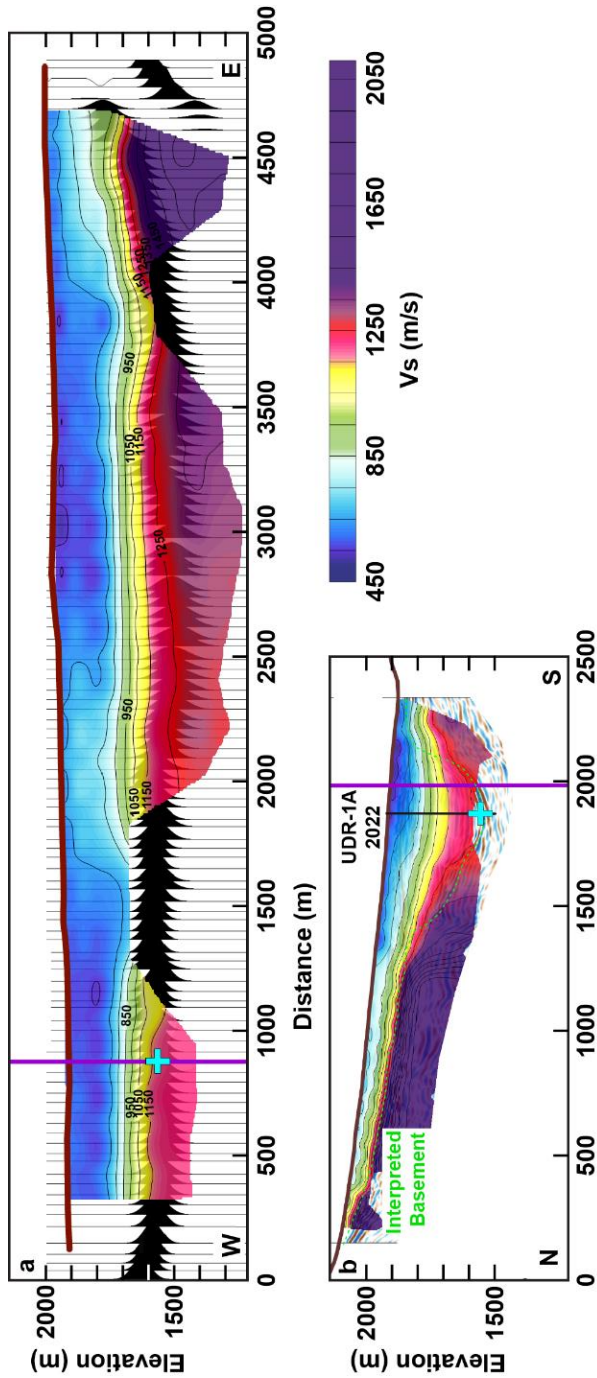


Figure 4.4: (a) Time-to-depth converted AC stack overlaid with V_s model obtained from inversion of Rayleigh wave dispersion curves. (b) Time-to-depth converted PSTM active seismic stack overlaid with V_s model inverted from Rayleigh waves

recorded during active seismic acquisition. Dashed green line: Interpreted sedimentary-basement interface. Solid black line: Trajectory of UDR-1A well. Solid purple line: Intersection of the N-S active profile and the W-E passive profile. Cyan cross: Elevation at which basement interface is interpreted from UDR-1A cores and logs.

4.6 Results and Discussion

The teleseismic coda wave AC stack (Figure 4.2 d) retrieves a laterally coherent phase between 0.2 – 0.6 s, which is interpreted as zero-offset reflection from the high-impedance contrast at the sedimentary-basement interface in the subsurface. With 3 Hz dominant frequency, the AC reflection has a lateral resolution (radius of first Fresnel zone) of ~250 m at 0.2 s TWT and ~400 m at 0.5 s TWT. For a complex 3-dimensional subsurface geometry, this implies superposition of reflections from different subsurface points. This effect likely plays a role at the eastern end where the profile approaches the basement outcrop (Figure 1b), and later reflections appear. However, the clear and unambiguous appearance of the reflection along all other parts of the profile suggest a wide transverse extent of the valley floor as also interpreted in the PSTM image of the active source line (Patterson et al., 2021; Figure S4.5).

The study of Patterson et al. (2021) was conducted prior to the recently drilled well UDR-1A, and in the absence of well information the PSTM was depth-

converted using the smoothed PSTM velocity model. However, the sonic log in the well showed significantly lower interval velocities and subsequently a shallower basement. We therefore re-evaluate the PSTM time-to-depth conversion using the sonic log from the well (Figure S4.5) and also use these velocities to depth-convert the AC stack. This yields a good match in the basement depths (~360 m) estimated at the intersection point of the AC stack and PSTM stack (Figure 4.4). Along the 5 km long passive seismic profile, the depth-converted AC reveals that the deepest basement interface is approximately 500 m (at 2500 m profile distance) below the modern surface and shallows to a depth of nearly 200 m near the eastern end. We note that potential lateral velocity variations in the sediments are not considered in our depth-conversion. Given the limited range of V_s -velocities (see below) and the overall similarity of cores and sonic logs in wells UDR-1A and Massey, we however assume that significant depth changes of the AC stack are not to be expected.

Next, we analyze the 2D V_s inversion along the passive profile (Figure 4a; referred to as 'passive V_s model'). The model indicates a layer of $V_s < 650$ m/s extending from the modern surface down to ~200 m. In the same depth range, moderate lateral velocity variations ($650 \text{ m/s} < V_s < 700 \text{ m/s}$) are observed between profile distances 1700 – 2500 m and 4000 – 4700 m. These velocity variations could be the result of the influence of increased basement debris exposures on the shallow surface wave propagation. These low velocities result in V_p/V_s ratios ranging from

3 to 4 when compared to active source travel time tomography (Behm et al., 2019) and well log data. Similar V_p/V_s ratios were also reported by Behm et. al (2019) for the sediment fill on the active line.

At depths below 200 – 250 m, the low velocity zone, V_s transitions from ca. 800 m/s to > 1250 m/s within a depth interval of ~200 m. We refrain from interpreting this transition zone as a geological unit, as this is most likely an artifact of the V_s inversion process when applied to an abrupt velocity change at the sedimentary-basement interface. This assumption is supported by the well logs which show a rather homogenous lithology (lacustrine sediments) for the deeper section.

Combined interpretation of the passive V_s model and the depth-converted AC stack (Figure 4.4 a) shows that the 1250 m/s V_s contour coincides with the basement interface reflection in the left and central parts of the profile. The low V_s for the gneissic basement may suggest strong weathering and fracturing, which is also observed in the well cores. However, the velocity is still significantly low when compared to the basement sonic log (V_p ~4500 m/s) and would imply an unrealistic high basement V_p/V_s ratio >3. Further, the velocity increases as the basement shallows near the eastern end (profile distance 4000 – 4700 m). We therefore attribute the low basement velocity in the western and central part to the reduced sensitivity of the 1 – 5 Hz surface waves to the deep layers.

Behm et al. (2019) applied surface wave analysis of the active source data with a traditional MASW approach (Xia et al., 1999) using phase-shift dispersion imaging. To compare to the passive Vs model, we reprocess this data set with the workflow and identical parameters as outlined in section 4.2. The result (Figure 4.4 b) indicates realistic Vs up to 2000 m/s for the gneiss basement where it is shallow (< 200 m), but also lacks to correctly image the deep part where it crosses the passive line. We again attribute this to the lack of low frequencies in the data, reducing the sensitivity to the deeper layers.

The proximity of the eastern part of the passive profile to the northern basement outcrops suggests that these stations image the northern (shallow) slope of the buried valley. Stations in the western part (profile distances ca. 1000 – 1800 m) were deployed close to the southern slope. The geometry thus implies that the passive profile traverses the canyon diagonally. Consequently, the central part of the profile, where the basement appears deepest (~500 m below surface; profile distance ca. 2200 m – 3200 m), should cross the valley floor. Comparing the elevation of the deepest point on the passive profile (~1470 m; profile distance ~2600 m) with outcropped basement on the valley floor 35 km to the east (~1900 m; Soreghan et al., 2015) and the deepest point (~1560 m) in the PSTM image ca. 2 km to the west, we interpret the overall structure as an overdeepened valley. Given the lack of evidence for faults with sufficient vertical offset in both surface geology (William, 1964) and the images from active and passive seismic data, we

suggest that overdeepening occurred through glacial carving of the bedrock. As quaternary glaciation of this part of the Colorado Plateau is highly unlikely (Soreghan et al., 2007), Figure 4.4a is interpreted to represent Paleozoic or even earlier along-axis alpine glacial carving - a process which to our knowledge has not been imaged yet.

4.7 Conclusions

We have successfully applied teleseismic P-wave coda AC to image the geometry of the buried basement interface along a 5 km longitudinal section of a paleovalley from 10 large magnitude teleseismic events. We also estimate the longitudinal shear-wave structure of the sedimentary fill in the valley using SI applied to high frequency (1-8 Hz) surface waves from highway traffic and local quarry operations. In our case, passive seismic imaging from short-duration deployments (1 month) allows imaging of shallow-targets (< 500 m depth) with sufficient resolution and significantly reduced effort and costs compared to active source acquisition.

Our results show an undulating valley floor in depths ranging from 200 to 500 m and are validated by recently acquired active seismic and well data. In the context of the debate on the evolution of Unaweep Canyon, our findings support glacial carving of the bedrock. An integrated interpretation and discussion of

further geodynamical implications will benefit from the UDR-1A core analysis which is currently ongoing.

4.8 Supplementary materials

4.8.1 Introduction

The supporting information contains:

(1) Time-to-depth conversion of a previously processed PSTM stack along an active seismic profile acquired across the Unaweep Canyon in 2017. We use the sonic log from a recently drilled well (UDR-1A, 2022) for the time-to-depth conversion.

(2) Moho reflection derived from teleseismic autocorrelations (AC). Our Moho reflection time agrees with other previous studies, thereby validating the teleseismic AC methodology.

(3) Intermediate processing product - raw interferometric virtual source gathers. That are F-K filtered before further processing.

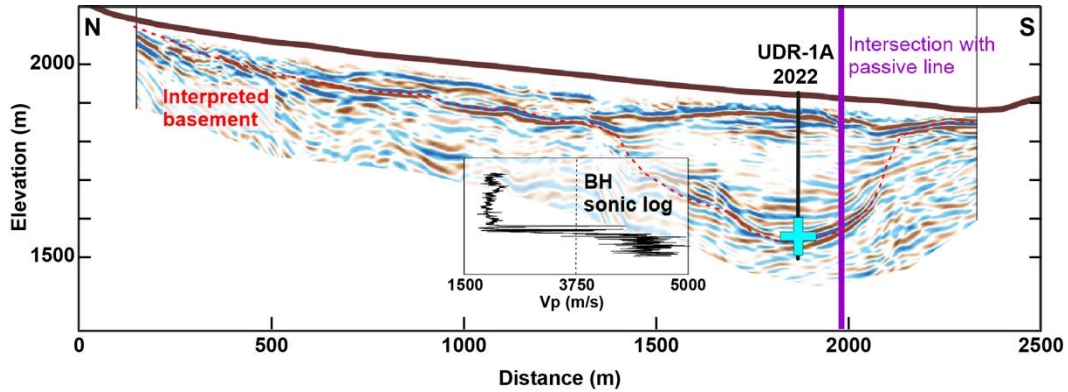


Figure S4.5: Time-to-depth converted PSTM stack of active seismic profile acquired in 2017 (Patterson et al., 2021). Inset shows the depth-aligned borehole P-wave sonic log from well UDR-1A well that is integrated into the velocity model used for time-to-depth conversion. Above the start of the log (elevation 1715 m), the velocity model is based on geologic well information and tomographic velocity models (Behm et al. 2019). Red dashed line: Interpreted basement interface. Solid black line: Well trajectory. Cyan cross: basement top elevation interpreted from well cores and logs. Purple line: Intersection of the active and passive seismic profiles.

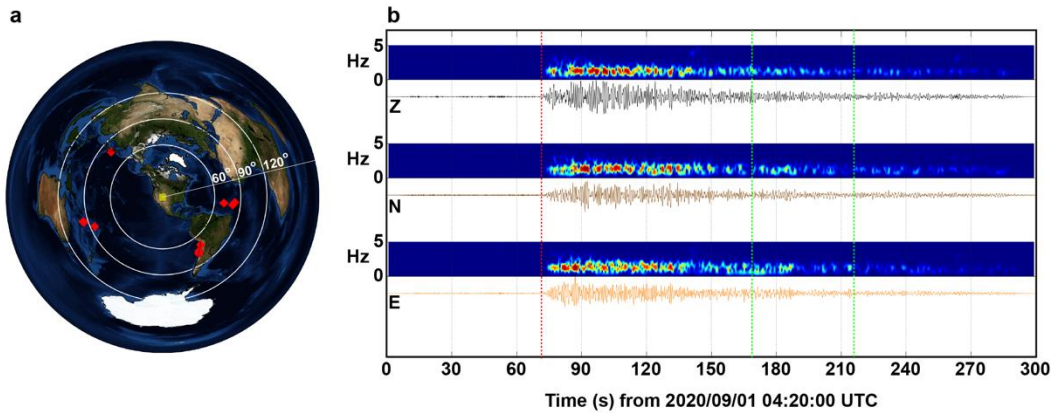


Figure S4.6: (a) Location of 10 teleseismic events used in this study. (b) 3-component spectrograms and waveforms for a 6.8 magnitude event. Origin time 2020/09/01 04:09:28 UTC. Latitude: 27.97 S; Longitude: 71.30 W. Red dashed line: P-wave first arrival time. Green dashed line: 50 s time segments selected for coda wave autocorrelation.

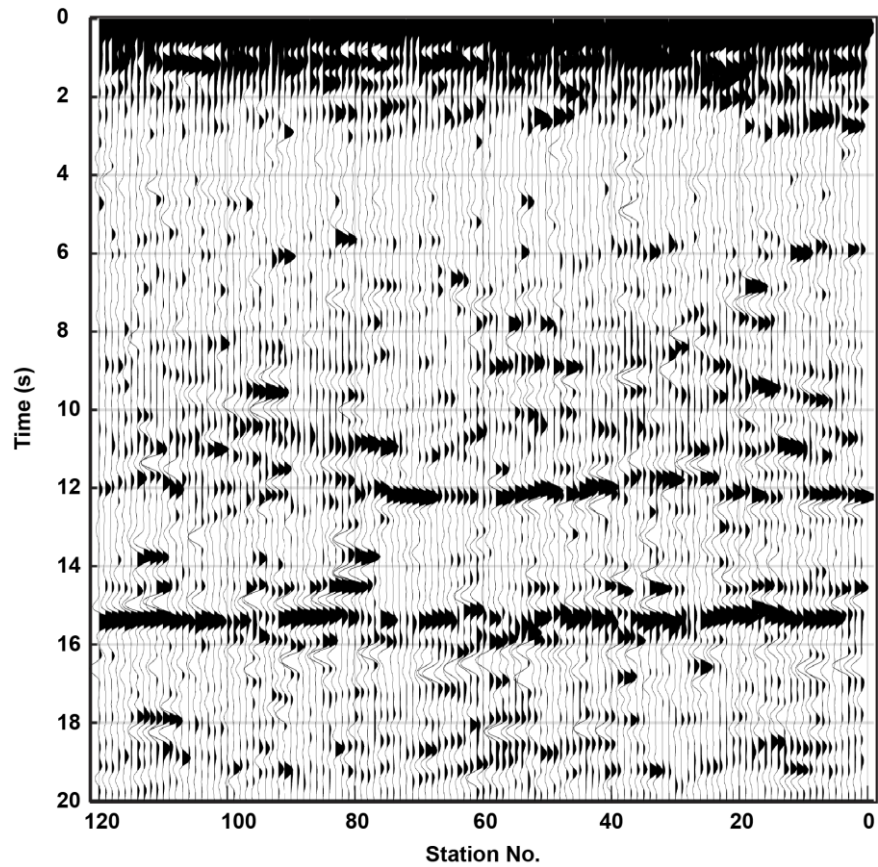


Figure S4.7: AC stack of ballistic teleseismic P-waves. The stack has been low passed at 2 Hz and is normalized for display.

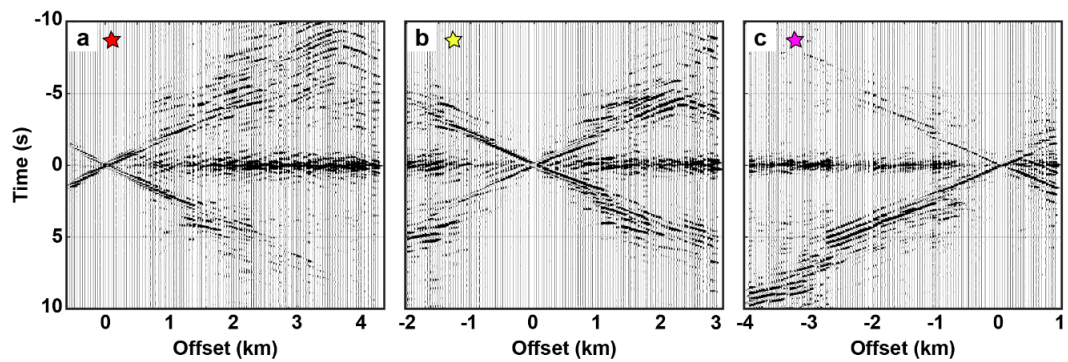


Figure S4.8: (a-c) Raw full-offset virtual source gathers at 3 receiver locations marked with the same-colored stars in Figure 4.1b.

Bibliography

Abe, S., Kurashimo, E., Sato, H., Hirata, N., Iwasaki, T., & Kawanaka, T. (2007). Interferometric seismic imaging of crustal structure using scattered teleseismic waves. *Geophysical Research Letters*, *34*(19), L19305. <https://doi.org/10.1029/2007GL030633>

Aki, K. (1957). Space and time spectra of stationary stochastic waves, with special reference to microtremors. *Bulletin of the Earthquake Research Institute*, *35*, 415–457.

Becker, G., & Knapmeyer-Endrun, B. (2019). Crustal thickness from horizontal component seismic noise auto- and cross-correlations for stations in Central and Eastern Europe. *Geophysical Journal International*, *218*(1), 429–445. <https://doi.org/10.1093/gji/ggz164>

Behm, M., Cheng, F., Patterson, A., & Soreghan, G. S. (2019). Passive processing of active nodal seismic data: estimation of V_P/V_S ratios to characterize structure and hydrology of an alpine valley infill. *Solid Earth*, *10*, 1337-1354. <https://doi.org/10.5194/se-10-1337-2019>

Bensen, G. D., Ritzwoller, M. H., Barmin, M. P., Levshin, A. L., Lin, F., Moschetti, M. P., Shapiro, N. M., & Yang, Y. (2007). Processing seismic ambient

noise data to obtain reliable broad-band surface wave dispersion measurements. *Geophysical Journal International*, 169(3), 1239–1260. <https://doi.org/10.1111/j.1365-246X.2007.03374.x>

Block, L., Wood, C. K., Besana-Ostman, G., Schwarzer, J., Ball, J., & Kang, J. B. (2021). 2020 Annual Report, Paradox Valley Seismic Network, Paradox Valley Unit, Colorado: Technical Memorandum No. 86-68330-2021-7, Bureau of Reclamation, Denver, Colorado.

Cater, F.W., Jr. (1966). Age of the Uncompahgre Uplift and Unaweep Canyon, west-central Colorado. U.S. Geological Survey Professional Paper 550-C, C86–C92.

Cheng, F., Xia, J., Ajo-Franklin, J. B., Behm, M., Zhou, C., Dai, T., Xi, C., Pang, J., & Zhou, C. (2021). High-Resolution Ambient Noise Imaging of Geothermal Reservoir Using 3C Dense Seismic Nodal Array and Ultra-Short Observation. *Journal of Geophysical Research: Solid Earth*, 126(8). <https://doi.org/10.1029/2021JB021827>

Claerbout, J. F. (1968). Synthesis of a layered medium from its acoustic transmission response. *Geophysics*, 33(2), 264–269. <https://doi.org/10.1190/1.1439927>

Cole, R.D., & Young, R.G., (1983). Evidence for glaciation in Unaweep Canyon, Mesa County, Colorado. In W.R. Averett (Ed.), *Northern Paradox Basin-Uncompahgre Uplift, Grand Junction Geological Society Field Trip Guidebook 1983* (pp. 73-80). Grand Junction, Colorado: Grand Junction Geological Society.

Dangwal, D., & Behm, M. (2021). Interferometric body-wave retrieval from ambient noise after polarization filtering: Application to shallow reflectivity imaging. *Geophysics*, *86*(6), Q47-Q58. <https://doi.org/10.1190/geo2020-0768.1>

Ekström, G., Abers, G. A., & Webb, S. C. (2009). Determination of surface-wave phase velocities across USArray from noise and Aki's spectral formulation. *Geophysical Research Letters*, *36*(18). <https://doi.org/10.1029/2009GL039131>

Fu, L., Pan, L., Li, Z., Dong, S., Ma, Q., & Chen, X. (2022). Improved high-resolution 3D Vs model of long beach, CA: Inversion of multimodal dispersion curves from ambient noise of a dense array. *Geophysical Research Letters*, *49*(4). <https://doi.org/10.1029/2021GL097619>

Gannett, H. (1882). The Unaweep Canyon (Colorado). *Popular Science Monthly*, *20*, 781–786.

Hannemann, K., Papazachos, C., Ohrnberger, M., Savvaidis, A., Anthymidis, M., & Lontsi, A. M. (2014). Three-dimensional shallow structure from high-frequency ambient noise tomography: New results for the Mygdonia basin-

Euroseistest area, northern Greece. *Journal of Geophysical Research: Solid Earth*, 119(6), 4979–4999. <https://doi.org/10.1002/2013JB010914>

Hauser, E. C., & Lundy, J. (1989). COCORP deep reflections: Moho at 50 km (16 s) beneath the Colorado Plateau. *Journal of Geophysical Research*, 94(86), 7071-7081.

Heath, B. A., Hooft, E. E. E., & Toomey, D. R. (2018). Autocorrelation of the Seismic Wavefield at Newberry Volcano: Reflections From the Magmatic and Geothermal Systems. *Geophysical Research Letters*, 45(5), 2311–2318. <https://doi.org/10.1002/2017GL076706>

Jia, Z., & Clayton, R. W. (2021). Determination of Near Surface Shear-Wave Velocities in the Central Los Angeles Basin with Dense Arrays. *Journal of Geophysical Research: Solid Earth*, 126(5). <https://doi.org/10.1029/2020JB021369>

Kennet, B. L. N. (2015). Lithosphere-asthenosphere P-wave reflectivity across Australia. *Earth and Planetary Science Letters*, 431, 225-235.

Kennett, B. L. N., & Engdahl, E. R. (1991). Traveltimes for global earthquake location and phase identification. *Geophysical Journal International*, 105(2), 429–465. <https://doi.org/10.1111/j.1365-246X.1991.tb06724.x>

Lin, F. C., Moschetti, M. P., & Ritzwoller, M. H. (2008). Surface wave tomography of the western United States from ambient seismic noise: Rayleigh and

Love wave phase velocity maps. *Geophysical Journal International*, 173(1), 281–298. <https://doi.org/10.1111/j.1365-246X.2008.03720.x>

Lohman, S. W. (1961). Abandonment of Unaweep Canyon, Mesa County, Colorado, by capture of the Colorado and Gunnison Rivers. U.S. Geological Survey Professional Papers, 424-B, B144–B146.

Patterson, A., Behm, M., Chwatal, W., Flores-Orozco, A., Wang, Y., & Soreghan, G. S. (2021). Seismic Reflection and Electrical Resistivity Imaging Support Pre-Quaternary Glaciation in the Rocky Mountains (Unaweep Canyon, Colorado). *Geophysical Research Letters*, 48(18). <https://doi.org/10.1029/2021GL094706>

Phạm, T. S., & Tkalčić, H. (2017). On the feasibility and use of teleseismic P wave coda autocorrelation for mapping shallow seismic discontinuities. *Journal of Geophysical Research: Solid Earth*, 122(5), 3776–3791. <https://doi.org/10.1002/2017JB013975>

Phạm, T. S., & Tkalčić, H. (2018). Antarctic ice properties revealed from teleseismic P wave coda autocorrelation. *Journal of Geophysical Research: Solid Earth*, 123(9), 7896–7912. <https://doi.org/10.1029/2018JB016115>

Polychronopoulou, K., Lois, A., & Draganov, D. (2020). Body-wave passive seismic interferometry revisited: Mining exploration using the body waves

of local microearthquakes. *Geophysical Prospecting*, 68, 232–253.
doi:10.1111/1365-2478.12884

Prieto, G. A., Lawrence, J. F., & Beroza, G. C. (2009). Anelastic Earth structure from the coherency of the ambient seismic field. *Journal of Geophysical Research: Solid Earth*, 114(7). <https://doi.org/10.1029/2008JB006067>

Ruigrok, E., & Wapenaar, K. (2012). Global-phase seismic interferometry unveils P-wave reflectivity below the Himalayas and Tibet. *Geophysical Research Letters*, 39(11). <https://doi.org/10.1029/2012GL051672>

Saygin, E., Cummins, P. R., & Lumley, D. (2017). Retrieval of the P wave reflectivity response from autocorrelation of seismic noise: Jakarta Basin, Indonesia. *Geophysical Research Letters*, 44(2), 792–799. <https://doi.org/10.1002/2016GL071363>

Schimmel, M., & Paulssen, H. (1997). Noise reduction and detection of weak, coherent signals through phase-weighted stacks. *Geophysical Journal International*, 130(2), 497–505. <https://doi.org/10.1111/j.1365-246X.1997.tb05664.x>

Serdyukov, A. S., Yablokov, A. v., Duchkov, A. A., Azarov, A. A., & Baranov, V. D. (2019). Slant f-k transform of multichannel seismic surface wave data. *Geophysics*, 84(1), A19–A24. <https://doi.org/10.1190/geo2018-0430.1>

Sergeant, A., Chmiel, M., Lindner, F., Walter, F., Roux, P., Chaput, J., Gimbert, F., & Mordret, A. (2020). On the Green's function emergence from interferometry of seismic wave fields generated in high-melt glaciers: Implications for passive imaging and monitoring. *Cryosphere*, *14*(3), 1139–1171. <https://doi.org/10.5194/tc-14-1139-2020>

Shapiro, N. M., & Campillo, M. (2004). Emergence of broadband Rayleigh waves from correlations of the ambient seismic noise. *Geophysical Research Letters*, *31*(7). <https://doi.org/10.1029/2004GL019491>

Socco, L. V., Boiero, D., Foti, S., & Wisén, R. (2009). Laterally constrained inversion of ground roll from seismic reflection records. *Geophysics*, *74*(6). <https://doi.org/10.1190/1.3223636>

Soreghan, G. S., Soreghan, M. J., Poulsen, C. J., Young, R. A., Eble, C. F., Sweet, D. E., & Davogustto, O. C. (2008). Anomalous cold in the Pangaeian tropics. *Geology*, *36*(8), 659–662. <https://doi.org/10.1130/G24822A.1>

Soreghan, G. S., Sweet, D. E., & Heavens, N. G. (2014). Upland glaciation in tropical pangaea: Geologic evidence and implications for late paleozoic climate modeling. *Journal of Geology*, *122*(2), 137–163. <https://doi.org/10.1086/675255>

Soreghan, G. S., Sweet, D. E., Marra, K. R., Eble, C. F., Soreghan, M. J., Douglas Elmore, R., Kaplan, S. A., & Blum, M. D. (2007). An Exhumed Late Paleozoic Canyon in the Rocky Mountains. *Journal of Geology*, 115, 473-481.

Soreghan, G. S., Sweet, D. E., Thomson, S. N., Kaplan, S. A., Marra, K. R., Balco, G., & Eccles, T. M. (2015). Geology of Unaweep Canyon and its role in the drainage evolution of the northern Colorado Plateau. *Geosphere*, 11(2), 320–341. <https://doi.org/10.1130/GES01112.1>

Soreghan, G. S., Dulin, S., Behm, M., Harris, B., Dangwal, D., Stephenson, M., & Valles, K.S. (2022). UDR_public [WWW Document]. <https://doi.org/10.17605/OSF.IO/5UHCK>

Tibuleac, I. M., & von Seggern, D. (2012). Crust-mantle boundary reflectors in Nevada from ambient seismic noise autocorrelations. *Geophysical Journal International*, 189(1), 493–500. <https://doi.org/10.1111/j.1365-246X.2011.05336.x>

Viens, L., Jiang, C., & Denolle, M. A. (2022). Imaging the Kanto Basin seismic basement with earthquake and noise autocorrelation functions. *Geophysical Journal International*, 230(2), 1080–1091. <https://doi.org/10.1093/gji/ggac101>

Wang, C., Tauzin, B., Pham, T. S., & Tkalčić, H. (2020). On the efficiency of P-wave coda autocorrelation in recovering crustal structure: Examples from dense arrays in the eastern United States. *Journal of Geophysical Research: Solid Earth*, 125(12). <https://doi.org/10.1029/2020JB020270>

Wang, Y., Lin, F. C., & Ward, K. M. (2019). Ambient noise tomography across the Cascadia subduction zone using dense linear seismic arrays and double beamforming. *Geophysical Journal International*, 217(3), 1668–1680. <https://doi.org/10.1093/gji/ggz109>

Wapenaar, K., Draganov, D., Snieder, R., Campman, X., & Verdel, A. (2010). Tutorial on seismic interferometry: Part 1 – Basic principles and applications. *Geophysics*, 75(5). <https://doi.org/10.1190/1.3457445>

Wapenaar, K., Slob, E., Snieder, R., & Curtis, A. (2010). Tutorial on seismic interferometry: Part 2 - Underlying theory and new advances. *Geophysics*, 75(5). <https://doi.org/10.1190/1.3463440>

Wathelet, M., Jongmans, D., & Ohrnberger, M. (2004). Surface-wave inversion using a direct search algorithm and its application to ambient vibration measurements. *Near Surface Geophysics*, 2(4), 211-221.

Williams, P. L. (1964). Geology, structure, and uranium deposits of the Moab quadrangle, Colorado and Utah. *U.S. Geological Survey*, Map I-360.

Wu, S. M., Lin, F. C., Farrell, J., Keller, W. E., White, E. B., & Hungerford, J. D. G. (2021). Imaging the subsurface plumbing complex of Steamboat Geyser and Cistern Spring with hydrothermal tremor migration using seismic interferometry. *Journal of Geophysical Research: Solid Earth*, 126(4). <https://doi.org/10.1029/2020JB021128>

Xia, J., Miller, R. D., & Park, C. B. (1999). Estimation of near-surface shear-wave velocity by inversion of Rayleigh waves. *Geophysics*, 64(3), 691-700.

Chapter 5

High-resolution imaging of the shallow subsurface and relationship with site responses using co-located Nodal and DAS arrays near Enid, Oklahoma

5.1 Abstract

Lateral variations in the near-surface structures can cause to spatial variations in observed ground shaking during earthquakes. Consequently, high-resolution studies of the near-surface are important in the context of urban seismic hazard assessment. Such information is usually lacking in a state like Oklahoma where sharp increase in seismicity has been observed in the last decade due to increased wastewater injections. We deploy a co-located distributed acoustic sensing (DAS) and nodal seismic array along a state highway near Enid, Oklahoma. The array observed lateral variations in recorded amplitudes for a local M2.7 earthquake. We utilize the continuously recorded seismic noise from local ambient

sources to image the near-surface shear velocity. Additionally, we also use ambient noise H/V (Horizontal-to-vertical) spectral ratio to constrain the shallow bedrock structure. Our results show significant correlation between the shallow velocity structures and the observed ground motion.

5.2 Introduction

During the last decade an increase in the rate and volume of wastewater injections for hydrocarbon recovery in Oklahoma has been linked to a surge in seismicity (Ellsworth, 2013; Keranen et al., 2014). Although the rate of seismicity has now reduced due to regulations in the scale of wastewater injections, several major earthquakes (2011 Mw5.7 Prague; 2016 Mw5.1 Fairview; 2016 Mw5.8 Pawnee) in the last decade have attracted the attention of the seismology community. Many of these induced events occur on previously unmapped faults or extensions of known faults in the OGS (Oklahoma Geological Survey) database (Schoenball and Ellsworth, 2017a; Qin et al., 2019). Attempts to develop regional 3D crustal velocity models (Zhu, 2018; Chai et al., 2021; Ratre and Behm, 2021) leads to improvements in the quality of hypocenter relocations and have benefited the efforts to map the fault network in Oklahoma. However, these regional models have a limited applicability for urban seismic hazard assessment at sub-kilometer scale due to their low lateral and vertical resolution. Conventionally, active-source seismic experiments have been used for high-resolution local imaging. But

considering the logistical challenge of conducting such experiments in an urban environment, passive seismic methods are a more suitable alternative.

Following the initial development of passive seismic interferometry for continental scale imaging (Campillo and Paul, 2003; Shapiro and Campillo, 2004; Bensen et al., 2008) it has been used for high-resolution imaging at local scales including urban environments (Nakata et al., 2015; Chang et al., 2016; Fu et al., 2022). Such applications usually require dense and large arrays to achieve high lateral resolutions. The development of distributed acoustic sensing (DAS) technology, which offers the capability of using telecommunication optical-fiber cables as seismic sensors, is now emerging as an alternative to dense local deployments. Recent applications of DAS interferometry (e.g., Ajo-Franklin et al., 2019; Spica et al., 2020; Rodríguez Tribaldos et al., 2021; Yang et al., 2022) in urban and sub-urban environments have successfully retrieved the near-surface structure.

A few studies (e.g., He et al., 2021; Li et al., 2021) have imaged the Oklahoma crust at a local scale by using passive seismic methods. However, to our knowledge, no studies have been conducted in urban settings in Oklahoma. In this study, we acquire 25 days of passive seismic recordings on a DAS and nodal geophone array to the east of Enid in Oklahoma. The telecom optical fiber used for DAS acquisition is deployed in a duct running parallel to a busy highway (US 412).

Strong influence of traffic-induced strain and ineffective coupling with the subsurface makes interferometric retrieval of surface and body wave challenging. Nonetheless, local earthquake events are retrieved with high fidelity and lateral resolution on the DAS array. One such event (M2.3 on 2021/05/02) is used to measure the relative lateral variations in ground motion along the deployment.

Near-surface layers of unconsolidated material having low shear-velocity can trap seismic waves resulting in amplification of earthquake ground motion (Graves et al., 2011; Berg et al., 2021; Yang et al., 2022). Earthquakes are known to show spatial variations in ground motion intensity (e.g., Hough et al., 2010; Rajaure et al., 2017). Thus, seismic hazard assessment, especially in urban environments, requires near-surface models at high lateral resolutions. We apply two independent passive imaging methods on the nodal data to constrain the shallow (< 600 m) subsurface structure – (i) ambient noise interferometry, (ii) H/V spectral ratio (HVSR) analysis. We compare our interferometrically derived V_{s30} (shear-velocity in the upper 30-meter layer) model with the site amplification profile derived from the DAS data and observe significant correlation. Further, the agreement between the fundamental frequencies of ambient noise HVSR and the shallow shear-velocity (V_s) model lends confidence to our structural interpretation.

Our results highlight the capability of passive seismic methods for high resolution Vs imaging, which can then be used for identifying zones of high seismic risk and assist in urban planning.

5.3 Data

In the summer of 2021, we acquired a DAS and nodal seismic dataset near Enid, Oklahoma (Figure 5.1a). The data was recorded in two phases (Figure 5.1b). The eastern segment was acquired between April 2021 and May 2021, and the western segment between July 2021 and August 2021. An array of Fairfield MagSeis Zland 3C nodes (5 Hz corner frequency) are deployed at ~500m spacing and record at 250 samples per second. For the DAS recording we connect a telecom optical fiber cable to a Silixa iDAS interrogator (Parker et al., 2014) recording at 1000 samples per second. Here, we process 25-days of data from the eastern segment along a 20 km stretch of US 412 state highway. This segment (Figure 5.2a) consists of co-located DAS and 39 nodal sensors.

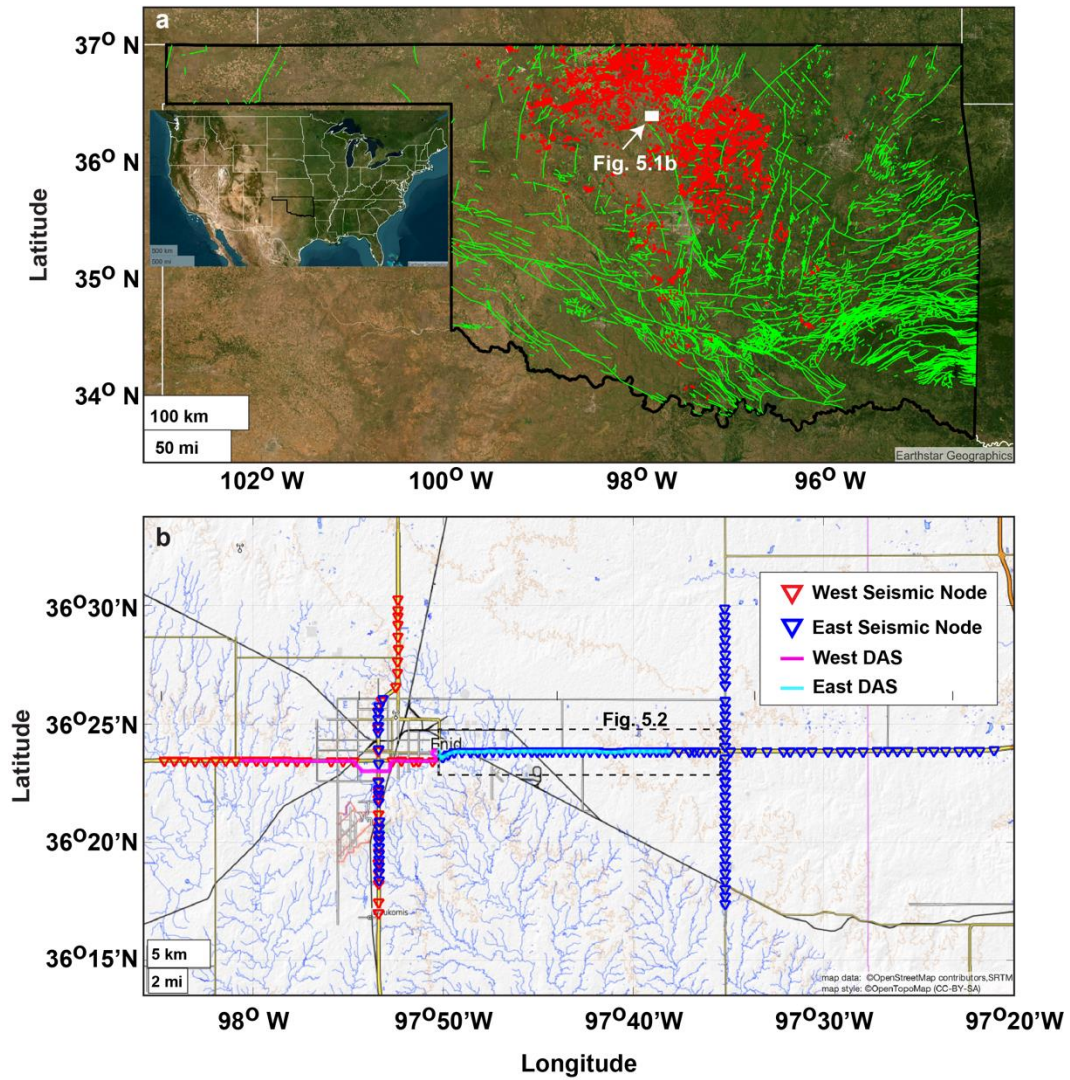


Figure 5.1. (a) Map of Oklahoma showing earthquake epicenters (red) and faults (green). Inset shows the location of Oklahoma (black edges) in the continental United States. White box indicates the location on Figure 5.1b. (b) Map showing the Enid deployment consisting of nodes (red and blue triangles) and DAS optical fiber (magenta and cyan lines).

The DAS setup records the along-fiber strain at ~9000 channels with 2m channel spacing resulting in ~1.5 GB of data per minute. For ease of handling such large data volumes, we decimate the DAS data both spatially and temporally. The channel spacing is increased to 20 m and the temporal sampling is reduced to 50 Hz. We intend to use the DAS data for interferometric processing and relative estimation of amplitude variation along the profile. Therefore, information about absolute ground motion is not required. Hence, we do not convert the DAS recorded strain to velocity or acceleration. However, minimal preprocessing is applied to the DAS recordings to suppress high-velocity artifacts. These are amplitude spikes which appear on all channels at a given time. We use a spatial filter which subtracts the median of all traces at a given time sample from each trace (Tribaldos et al., 2021). We then validated the DAS data by comparing local earthquake arrivals that are detected on both the node and DAS recordings (Figure 5.2). S-wave arrivals are recorded at a much higher lateral resolution on the DAS channels than on the node horizontal components. Further, the retrieval of reverberations (likely multiples from a high-impedance subsurface interface) on the DAS channels also validates the capability of DAS for detecting seismic signals. In the following sections, we apply passive seismic imaging methods to retrieve the near-surface structure.

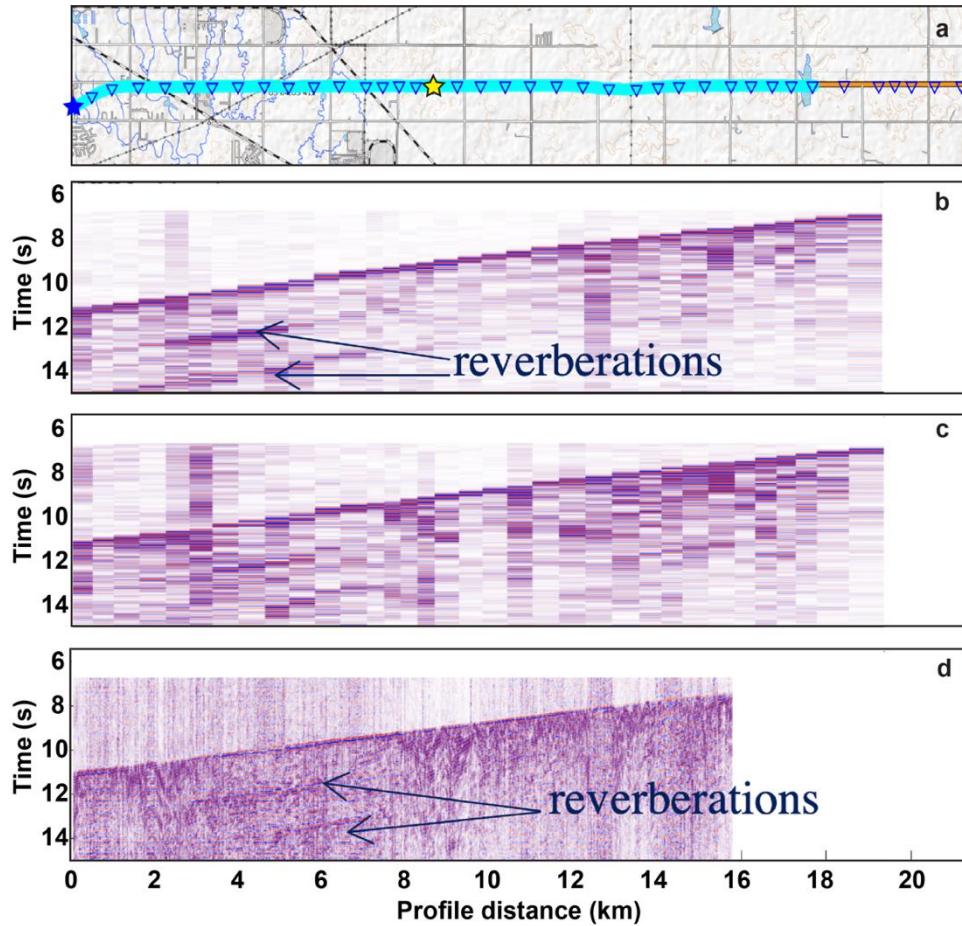


Figure 5.2. (a) Map view of the overlapping eastern node and DAS deployments. Blue and yellow star indicates the location of node 4001 and 4017 respectively. Comparison of (b) north component, (c) east component node recordings and (d) DAS recordings for the M2.3 local earthquake.

5.4 Methods

5.4.1 Ambient noise interferometry

Ambient noise interferometry involves the retrieval of the empirical Green's function response between a pair of receivers by cross-correlating the continuous recorded noise at the two locations (Wapenaar et al., 2010a). We follow a conventional methodology similar to Bensen et al. (2007) to calculate cross-correlations for all receiver pairs of the nodal and DAS arrays. The same processing workflow is applied to both the node and DAS datasets.

The continuously recorded data is split into 1-hour segments and preprocessed. Preprocessing includes - (i) down-sampling to 50Hz, (ii) linear detrending, (iii) 4 Hz low pass filtering, and (iv) automatic gain control (AGC) normalization. Spectral whitening is not performed during preprocessing because cross-coherency interferometry (e.g., Aki, 1957; Prieto et al., 2009; Wapenaar et al., 2010b) includes spectral whitening. Two railway tracks cross the array and act like high-frequency (> 5 Hz) persistent noise sources. The 4 Hz low pass filter prevents spurious arrivals on the interferograms resulting from these sources. The interferograms calculated for each 1-hour segment are then stacked (phase weighted stacking; Schimmel and Paulssen, 1997) over the recording period. Finally, the resultant interferograms from all station pairs are spatially sorted into virtual source gathers (VSG; Figure 5.3).

Figure 5.3 compares the node and DAS VSGs for two locations on the array. Note that only positive offset VSGs are shown here. Due to the presence of high-

frequency local anthropogenic noise sources (e.g., traffic), the node VSGs retrieve a surface wave packet in the 1 – 5 Hz frequency band. However, another dominant surface wave phase is retrieved in the <1 Hz band. Beamforming analysis reveals that this energy is propagating from a low frequency source oriented at 60° back-azimuth (~ N60°E) with respect to the array. The back-azimuth also explains the apparently high velocity retrieved on the east-west oriented node array. DAS VSGs (Figure 5.3 c, d) on the other hand, do not clearly retrieve surface waves. The few DAS VSGs that retrieve coherent surface wave moveouts are limited in offset extent (< 1 km). A coherent low-velocity moveout (15 – 30 m/s) corresponding to traffic speeds is observed on all DAS VSGs. This further indicates a strong sensitivity of the DAS fiber, particularly when deployed in highway ducts, to traffic-induced strain. Thus, in the following sections, we focus on the node data and only use the DAS data for calculating the site amplification.

We take advantage of the linear geometry of the nodal array by implementing a MASW (multi-channel analysis of surface waves; Xia et al., 1999) to estimate a 2D shear-velocity model. We split each VSG into four sub-gathers based on time (causal and acausal) and offset (positive and negative) ranges. The absolute offset range of the sub-gathers is truncated to 5 km in order to minimize excessive lateral smoothing of the resultant velocity structure. The MASW workflow is then applied to each sub-gather and the resulting shear-velocity model is spatially assigned to the mid-point of the sub-array. The MASW workflow

involves – (i) Rayleigh wave phase velocity dispersion analysis, (ii) manual picking of dispersion curves, followed by (iii) shear-velocity inversion using a hybrid neighborhood inversion algorithm (Geopsy; Wathelet et al., 2004).

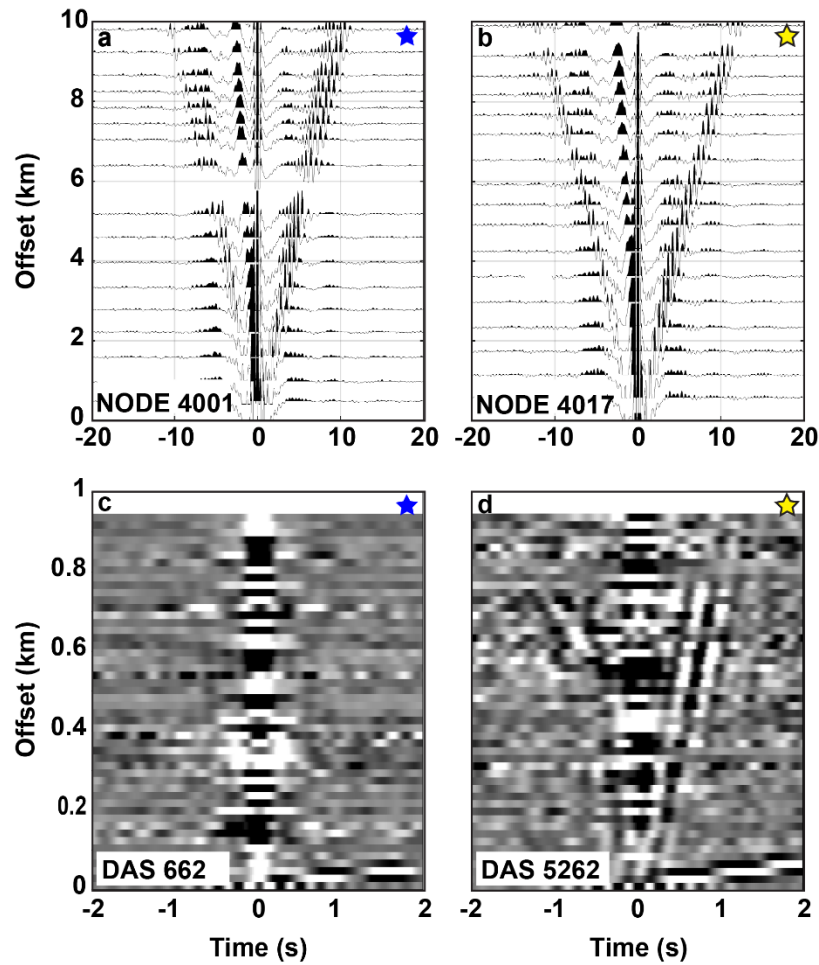


Figure 5.3. Comparison of (a, b) node and (c, d) DAS VSGs for virtual sources at (a) node 4001 and co-located (c) DAS channel 662. Similarly (b) node 4017 and co-located (d) DAS channel 5262. The locations are indicated with blue and yellow stars in Figure 5.2.

5.4.2 H/V spectral analysis

Besides interferometrically retrieving the surface wave propagation, we also utilize the 3C node dataset to estimate the relative amplification of the horizontal component. This is based on the horizontal-to-vertical spectral ratio (HVSr; Nakamura, 1989) which is dependent on the natural frequency of the near-surface layers and has been widely used for site effect characterization (e.g., Garcia-Jerez et al., 2016; Stanko et al., 2017; Spica et al., 2018, 2020). The HVSr is directly sensitive to the impedance boundaries in the near-surface structure.

We follow the formulation of Arai and Tokimatsu (2004),

$$\frac{H}{V}(x, f) = \sqrt{\frac{E(x, f) + N(x, f)}{Z(x, f)}}, \quad (1)$$

Where E , N and Z are the spectral amplitudes of the east, north and vertical components; x is the receiver location; f is the frequency. The average HVSr function at a receiver location (Figure 5.4) is calculated as the average HVSr for all the 1-hour data segments.

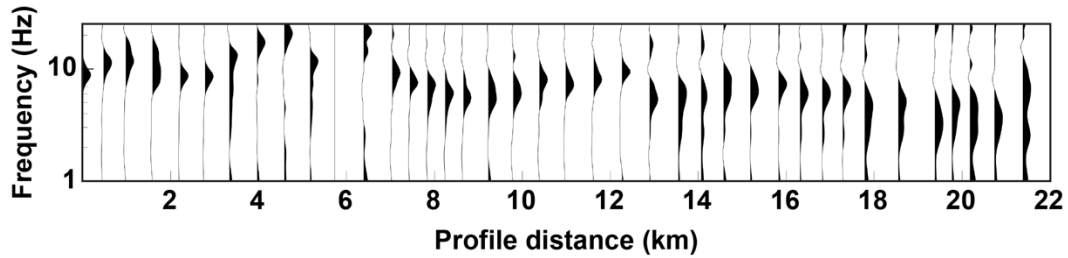


Figure 5.4. Horizontal-to-vertical spectral ratio (HVSr) calculated for the nodal array.

5.5 Results and discussions

5.5.1 Near-surface structural model

Ambient noise recordings in urban environments, especially along highways are dominated by high-frequency anthropogenic noise. Considering the sensitivity of Rayleigh wave to the shear-velocities at depths equivalent to one-third of the wavelength (Haney and Tsai, 2015), we recover the V_s structure at depths of 330 m (Figure 5a). This is based on the maximum Rayleigh wave phase velocity of 1000 m/s at 1 Hz (figure 5.3). The V_s model shows a near-surface layers with velocities as low as 600 m/s and depth variation between 20 – 60 m from west to east. Below this layer is an approximately 250 m deep micro-basin structure flanked by high velocities (~ 1500 m/s) in the west.

The near-surface structure is also constrained by the HVSr measurements. We interpret the HVSr peak frequency in the 1 – 20 Hz range as a sedimentary

layer of depth (h) using the relationship (Castellaro and Mulargia, 2009; Cheng et al., 2021),

$$f_0(x) = \frac{V_s(x)}{4h(x)}, \quad (2)$$

where $f_0(x)$ is the peak frequency and $V_s(x)$ is the average shear-velocity of the shallow (< 60 m) sedimentary layer at node location x . The resultant depth-converted HVSR (Figure 5.5b) shows a structurally deepening trend from west to east and likely represents the near-surface low-velocity layer (LVL). This interpretation is further corroborated by the eastward dipping LVL ($V_s < 800$ m/s) in the inverted V_s model (Figure 5.5b). It is noted that the laterally unconstrained inversion scheme employed here estimates each 1D V_s independently along the profile, which results in abrupt lateral variations in the overall 2D V_s model. Nevertheless, the near-surface V_s model of the upper 30 m (Figure 5.5c) shows a consistent decrease in velocity from west to east direction along the profile.

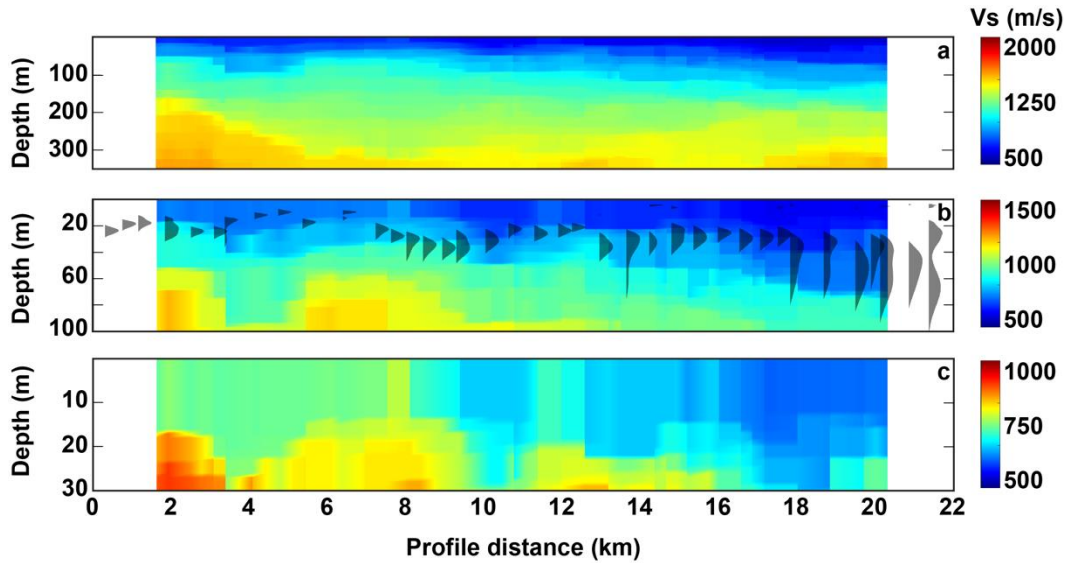


Figure 5.5. V_s model obtained from inversion of Rayleigh wave dispersion curves. The same V_s model showing the (a) upper 100 m and (b) upper 30 m. In Figure 5.5b, the wiggle plot is the depth-converted HVSR.

5.5.2 Site amplification correlated with subsurface structure

The application of two independent passive seismic methods helps us to robustly estimate the near-surface structure both in terms of V_{s30} and the depth of LVL (Figure 5.6b; V_{s30} – red, depth of LVL – black,). The near-surface structure is well correlated with the surface geology information (Figure 5.6a). Higher velocities (750 – 800 m/s) in the west (0 – 8 km profile distance) coincide with the Quaternary Terrace deposits (Qt), while the lower velocities (600 – 750 m/s) in the central and eastern sections are associated with Permian formations. Similar

correlation is also observed for the depth of LVL. The LVL is shallower (< 25 m) in the western profile (0 – 6 km) coinciding with the Qt deposits, and generally deepens (20 – 60 m) below the Permian deposits.

Apart from demonstrating the feasibility of shallow passive seismic imaging, these results are also relevant from an engineering perspective due to their influence on ground motion. Ground Motion Models (GMMs) generally rely on Vs30 measurements to characterize the subsurface (Douglas, 2014). However, ground motion has also been linked to structure (velocity and thickness) of layers deeper than 30 m (e.g., Chiou and Youngs, 2008; Campbell and Bozorgnia, 2014). Since DAS imaging provides detailed information of the near-surface structure and velocity beyond Vs30, it can be useful tool for site characterization. To evaluate the relation between near-surface structure and ground-motion, we first compute the DAS spectral amplitude variation along the profile for the M2.3 earthquake. At each DAS channel, the data is integrated to strain and band-passed in the 0.5 – 4 Hz range to suppress local high energy noise (e.g., vibrations from railway tracks). The spectral amplitude variation is measured in frequency domain with a multi-taper algorithm (Prieto et al., 2009). To compensate geometric spreading effect, a scale factor based on source-receiver distance to the M2.3 earthquake is applied. The spectral amplitude is used as an approximation for site-amplification and informs the relative variation of ground-motion along the profile.

Figure 5.6b (blue) shows a generally increasing trend of site amplification from west to east. The near-surface model derived from node data has a lateral resolution (~ 500 m node spacing) one order of magnitude lower than the site amplification derived from DAS data (~ 20 m channel spacing). Despite the differences in lateral resolution, a clear anticorrelation is visible between the near-surface model and site amplification. Although the site amplification profile has an increasing trend from west to east, deviations (e.g., 7 – 10 km, 12 – 14 km) cannot be explained by the near-surface structure alone. Recently, some researchers (e.g., Chiou and Youngs, 2008; Campbell and Bozorgnia, 2014) have built empirical GMMs using $Z_{1.0}$ (depth of <1 km/s layer) and $Z_{2.5}$ (depth of <2.5 km/s layer). Thus, it is possible that the site amplification peak between 7 – 10 km may be related to the micro-basin at ~ 300 m depth and/or other deeper structures. It is difficult to delineate the structural cause of the site amplification between 12 – 14 km, which may be related to local faults that are not illuminated in our Vs model.

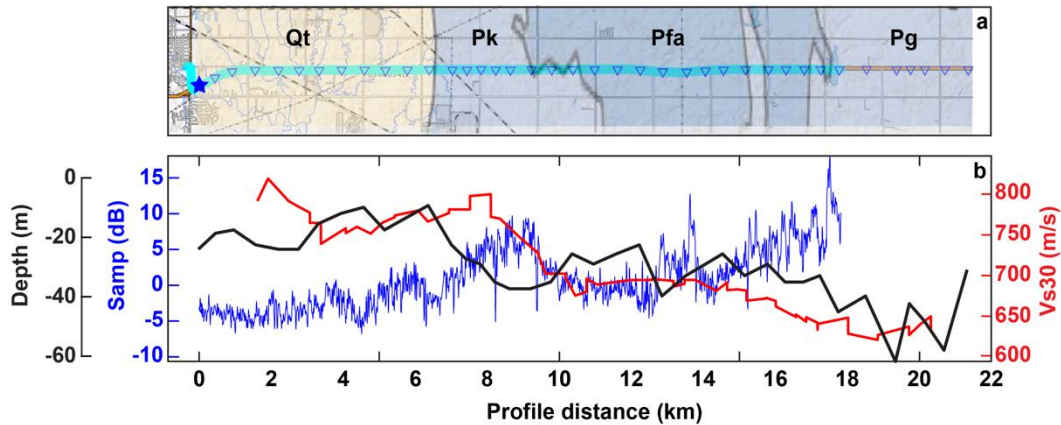


Figure 5.6. (a) Map view of the deployments (refer Figure 5.2a) overlaid with surface geology map (USGS; Heran et al., 2003). Qt: Quaternary Terrace Deposits; Pk: Permian Kingsman Siltstone; Pfa: Permian Fairmont Shale; Pg: Permian Garber Sandstone. (b) Plot showing the variation of Vs30 (red), frequency-to-depth converted HVSR peak (black), and DAS site amplification (blue) along the profile.

5.6 Conclusions

In this study we present the application of passive seismic interferometry to image the near-surface structure along a 20 km segment of an urban highway with the objective of assessing the local site response. We demonstrate the efficacy of short duration recordings on geophone nodes for shallow (~300 m depth) subsurface imaging using local ambient noise in the 1 – 5 Hz band. The high frequencies enable us to retrieve the near-surface LVL structure of 20 – 60 m thickness. The LVL structure is also corroborated by ambient noise HVSR analysis, thereby giving more confidence in our interpretation of the near-surface structure.

Our methodology captures the lateral and vertical variations in the near-surface shear-velocities and is thus more informative than a V_{s30} which is usually reported by other site response studies. We also estimate the relative variations in site amplification using a DAS recording along the same profile. Although, we do not propose a mathematical model linking the site amplification to the near-surface structure, we are able to demonstrate clear correlation between the two. Our results are particularly useful of urban seismic risk assessment and town planning at a sub-kilometer scale.

Bibliography

Ajo-Franklin, J. B., Dou, S., Lindsey, N. J., Monga, I., Tracy, C., Robertson, M., Rodriguez Tribaldos, V., Ulrich, C., Freifeld, B., Daley, T., & Li, X. (2019). Distributed Acoustic Sensing Using Dark Fiber for Near-Surface Characterization and Broadband Seismic Event Detection. *Scientific Reports*, 9(1). <https://doi.org/10.1038/s41598-018-36675-8>

Aki, K. (1957). Space and Time Spectra of Stationary Stochastic Waves, with Special Reference to Microtremors. *Bulletin of the Earthquake Research Institute*, 35, 415–457.

Arai, H., & Tokimatsu, K. (2004). S-Wave Velocity Profiling by Inversion of Microtremor H/V Spectrum. *Bulletin of the Seismological Society of America*, 94(1).

Bensen, G. D., Ritzwoller, M. H., Barmin, M. P., Levshin, A. L., Lin, F., Moschetti, M. P., Shapiro, N. M., & Yang, Y. (2007). Processing seismic ambient noise data to obtain reliable broad-band surface wave dispersion measurements. *Geophysical Journal International*, 169(3), 1239–1260. <https://doi.org/10.1111/j.1365-246X.2007.03374.x>

Bensen, G. D., Ritzwoller, M. H., & Shapiro, N. M. (2008). Broadband ambient noise surface wave tomography across the United States. *Journal of Geophysical Research: Solid Earth*, 113(5). <https://doi.org/10.1029/2007JB005248>

Berg, E. M., Lin, F. C., Schulte-Pelkum, V., Allam, A., Qiu, H., & Gkogkas, K. (2021). Shallow Crustal Shear Velocity and V_p/V_s Across Southern California: Joint Inversion of Short-Period Rayleigh Wave Ellipticity, Phase Velocity, and Teleseismic Receiver Functions. *Geophysical Research Letters*, 48(15). <https://doi.org/10.1029/2021GL092626>

Campbell, K. W., & Bozorgnia, Y. (2014). NGA-West2 ground motion model for the average horizontal components of PGA, PGV, and 5% damped linear acceleration response spectra. *Earthquake Spectra*, 30(3), 1087–1114. <https://doi.org/10.1193/062913EQS175M>

Campillo, M., & Paul, A. (2003). Long range correlations in the diffuse seismic coda. *Science*, 299(5606), 547–549. <https://doi.org/10.1126/science.1078551>

Castellaro, S., & Mulargia, F. (2009). VS30 estimates using constrained H/V measurements. *Bulletin of the Seismological Society of America*, 99(2 A), 761–773. <https://doi.org/10.1785/0120080179>

Chai, C., Delorey, A. A., Maceira, M., Levandowski, W., Guyer, R. A., Zhang, H., Coblenz, D., & Johnson, P. A. (2021). A 3D Full Stress Tensor Model for Oklahoma. *Journal of Geophysical Research: Solid Earth*, 126(4). <https://doi.org/10.1029/2020JB021113>

Chang, J. P., de Ridder, S. A. L., & Biondi, B. L. (2016). High-frequency Rayleigh-wave tomography using traffic noise from Long Beach, California. *Geophysics*, 81(2), B1–B11. <https://doi.org/10.1190/GEO2015-0415.1>

Cheng, F., Xia, J., Ajo-Franklin, J. B., Behm, M., Zhou, C., Dai, T., Xi, C., Pang, J., & Zhou, C. (2021). High-Resolution Ambient Noise Imaging of Geothermal Reservoir Using 3C Dense Seismic Nodal Array and Ultra-Short Observation. *Journal of Geophysical Research: Solid Earth*, 126(8). <https://doi.org/10.1029/2021JB021827>

Chiou, B. S. J., & Youngs, R. R. (2008). An NGA model for the average horizontal component of peak ground motion and response spectra. *Earthquake Spectra*, 24(1), 173–215. <https://doi.org/10.1193/1.2894832>

Douglas, J. (2014). Ground motion prediction equations 1964 – 2014. PEER Report 2011, 102.

Ellsworth, W. L. (2013). Injection-induced earthquakes. *Science*, 341(6142). <https://doi.org/10.1126/science.1225942>

Fu, L., Pan, L., Li, Z., Dong, S., Ma, Q., & Chen, X. (2022). Improved High-Resolution 3D Vs Model of Long Beach, CA: Inversion of Multimodal Dispersion Curves From Ambient Noise of a Dense Array. *Geophysical Research Letters*, *49*(4). <https://doi.org/10.1029/2021GL097619>

García-Jerez, A., Piña-Flores, J., Sánchez-Sesma, F. J., Luzón, F., & Perton, M. (2016). A computer code for forward calculation and inversion of the H/V spectral ratio under the diffuse field assumption. *Computers and Geosciences*, *97*, 67–78. <https://doi.org/10.1016/j.cageo.2016.06.016>

Graves, R., Jordan, T. H., Callaghan, S., Deelman, E., Field, E., Juve, G., Kesselman, C., Maechling, P., Mehta, G., Milner, K., Okaya, D., Small, P., & Vahi, K. (2011). CyberShake: A Physics-Based Seismic Hazard Model for Southern California. *Pure and Applied Geophysics*, *168*(3–4), 367–381. <https://doi.org/10.1007/s00024-010-0161-6>

Haney, M. M., & Tsai, V. C. (2015). Nonperturbational surface-wave inversion: A Dix-type relation for surface waves. *Geophysics*, *80*(6), EN167–EN177. <https://doi.org/10.1190/GEO2014-0612.1>

He, L., Wu, Q., Chen, X., Sun, X., Guo, Z., & Chen, Y. J. (2021). Detailed 3D Seismic Velocity Structure of the Prague, Oklahoma Fault Zone and the

Implications for Induced Seismicity. *Geophysical Research Letters*, 48(24).
<https://doi.org/10.1029/2021GL096137>

Heran, W. D., Green, G. & Stoesser, D. B. (2003). A Digital Geologic Map Database of Oklahoma. *U. S. G. S. Open File Report*, 03-247

Hough, S. E., Altidor, J. R., Anglade, D., Given, D., Janvier, M. G., Maharrey, J. Z., Meremonte, M., Mildor, B. S. L., Prepetit, C., & Yong, A. (2010). Localized damage caused by topographic amplification during the 2010 M7.0 Haiti earthquake. *Nature Geoscience*, 3(11), 778–782. <https://doi.org/10.1038/ngeo988>

Keranen, K. M., Weingarten, M., Abers, G. A., Bekins, B. A., & Ge, S. (2014). Sharp increase in central Oklahoma seismicity since 2008 induced by massive wastewater injection. *New Series*, 345(6195), 448–451. <https://doi.org/10.1126/science.1252000>

Li, Z., Shi, C., Ren, H., & Chen, X. (2022). Multiple Leaking Mode Dispersion Observations and Applications from Ambient Noise Cross-Correlation in Oklahoma. In *Geophysical Research Letters*, 49(1). <https://doi.org/10.1029/2021GL096032>

Nakata, N., Chang, J. P., Lawrence, J. F., & Boué, P. (2015). Body wave extraction and tomography at Long Beach, California, with ambient-noise

interferometry. *Journal of Geophysical Research: Solid Earth*, 120(2), 1159–1173.
<https://doi.org/10.1002/2015JB011870>

Prieto, G. A., Lawrence, J. F., & Beroza, G. C. (2009). Anelastic Earth structure from the coherency of the ambient seismic field. *Journal of Geophysical Research: Solid Earth*, 114(7). <https://doi.org/10.1029/2008JB006067>

Parker, T., Shatalin, S. V., Farhadiroushan, M., Kamil, Y. I., Gillies, A., Finfer, D., & Estathopoulos, G. (2014). Distributed acoustic sensing - A new tool for seismic applications. *First Break*, 32, 6–10.

Qin, Y., Chen, X., Walter, J. I., Haffener, J., Trugman, D. T., Carpenter, B. M., Weingarten, M., & Kolawole, F. (2019). Deciphering the Stress State of Seismogenic Faults in Oklahoma and Southern Kansas Based on an Improved Stress Map. *Journal of Geophysical Research: Solid Earth*, 124(12), 12920–12934.
<https://doi.org/10.1029/2019JB018377>

Rajaure, S., Asimaki, D., Thompson, E. M., Hough, S., Martin, S., Ampuero, J. P., Dhital, M. R., Inbal, A., Takai, N., Shigefuji, M., Bijukchhen, S., Ichiyanagi, M., Sasatani, T., & Paudel, L. (2017). Characterizing the Kathmandu Valley sediment response through strong motion recordings of the 2015 Gorkha earthquake sequence. *Tectonophysics*, 714–715, 146–157.
<https://doi.org/10.1016/j.tecto.2016.09.030>

Ratre, P., & Behm, M. (2021). Imaging the Deep Crustal Structure of Central Oklahoma Using Stacking and Inversion of Local Earthquake Waveforms. *Journal of Geophysical Research: Solid Earth*, 126(5). <https://doi.org/10.1029/2020JB021368>

Rodríguez Tribaldos, V., & Ajo-Franklin, J. B. (2021). Aquifer Monitoring Using Ambient Seismic Noise Recorded with Distributed Acoustic Sensing (DAS) Deployed on Dark Fiber. *Journal of Geophysical Research: Solid Earth*, 126(4). <https://doi.org/10.1029/2020JB021004>

Schimmel, M., & Paulssen, H. (1997). Noise reduction and detection of weak, coherent signals through phase-weighted stacks. *Geophysical Journal International*, 130(2), 497–505. <https://doi.org/10.1111/j.1365-246X.1997.tb05664.x>

Schoenball, M., & Ellsworth, W. L. (2017). Waveform-relocated earthquake catalog for Oklahoma and southern Kansas illuminates the regional fault network. *Seismological Research Letters*, 88(5), 1252–1258. <https://doi.org/10.1785/0220170083>

Shapiro, N. M., & Campillo, M. (2004). Emergence of broadband Rayleigh waves from correlations of the ambient seismic noise. *Geophysical Research Letters*, 31(7). <https://doi.org/10.1029/2004GL019491>

Spica, Z. J., Perton, M., Martin, E. R., Beroza, G. C., & Biondi, B. (2020). Urban Seismic Site Characterization by Fiber-Optic Seismology. *Journal of Geophysical Research: Solid Earth*, 125(3). <https://doi.org/10.1029/2019JB018656>

Spica, Z. J., Perton, M., Nakata, N., Liu, X., & Beroza, G. C. (2018). Site characterization at Groningen gas field area through joint surface-borehole H/V analysis. *Geophysical Journal International*, 212(1), 412–421. <https://doi.org/10.1093/gji/ggx426>

Stanko, D., Markušić, S., Strelec, S., & Gazdek, M. (2017). HVSR analysis of seismic site effects and soil-structure resonance in Varaždin city (North Croatia). *Soil Dynamics and Earthquake Engineering*, 92, 666–677. <https://doi.org/10.1016/j.soildyn.2016.10.022>

Wapenaar, K., Draganov, D., Snieder, R., Campman, X., & Verdel, A. (2010). Tutorial on seismic interferometry: Part 1 - Basic principles and applications. *Geophysics*, 75(5). <https://doi.org/10.1190/1.3457445>

Wapenaar, K., Slob, E., Snieder, R., & Curtis, A. (2010). Tutorial on seismic interferometry: Part 2 - Underlying theory and new advances. *Geophysics*, 75(5). <https://doi.org/10.1190/1.3463440>

Wathelet, M., Jongmans, D., & Ohrnberger, M. (2004). Surface-wave inversion using a direct search algorithm and its application to ambient vibration measurements. *Near Surface Geophysics*, 2(4), 211-221.

Xia, J., Miller, R. D., & Park, C. B. (1999). Estimation of near-surface shear-wave velocity by inversion of Rayleigh waves. *Geophysics*, 64(3), 691-700.

Yang, Y., Atterholt, J. W., Shen, Z., Muir, J. B., Williams, E. F., & Zhan, Z. (2022). Sub-Kilometer Correlation Between Near-Surface Structure and Ground Motion Measured with Distributed Acoustic Sensing. *Geophysical Research Letters*, 49(1). <https://doi.org/10.1029/2021GL096503>

Zhu, H. (2018). Crustal wave speed structure of North Texas and Oklahoma based on ambient noise cross-correlation functions and adjoint tomography. *Geophysical Journal International*, 214(1), 716–730. <https://doi.org/10.1093/gji/ggy169>.

Chapter 6

Conclusions

Passive seismic methods do not require a spatially and temporally localized source and are thus a tempting alternative to conventional (active source) seismic methods. This is particularly true, in logistically challenging terrains ranging from urban centers to Antarctic icesheet and exo-planets. However, limitations like scarcity of high-frequency ambient noise and heterogeneous noise source distribution, make shallow scale applications challenging. In this dissertation, I attempt to overcome these challenges and demonstrate the feasibility of local scale interferometry for high-resolution imaging of the shallow subsurface. The strategies used for this purpose can be broadly categorized as – (i) pre-selecting steeply incident seismic energy that satisfies the stationary phase assumption; (ii) planning the deployment to ensure the stationarity of the known noise sources. Further, the study areas explored here have unique geologies and research objectives. Example – (i) reflectivity imaging in an oil and gas reservoir, (ii) basement structural imaging in an alpine canyon, (iii) site characterization for an urban seismic hazard assessment. Such diverse environments suggest a wide scope for passive interferometric applications. In two of the studies presented here, the passive interferometry results are jointly interpreted with conventional data (e.g.,

well logs and active-source images). Thereby indicating the usefulness of passive seismic interferometry as a complementary and cost-effective approach to conventional imaging. The key results and conclusions from each study area are enumerated in the following section.

6.1 Summary of results

Some of the key results are as follows:

- (i) I develop polarization filters to automatically select steeply-incident body waves (P- and S-waves) from continuously recorded ambient noise at the Wellington oil field (Kansas, US). The body-wave rich dataset is then used to interferometrically retrieve the structural reflectivity in the shallow subsurface ($< 1\text{km}$ depth). In addition to imaging the P-wave reflections, I am also able to image the S-wave reflections which are reported by only a few passive studies. An important result from this study is the estimation of near-surface seismic speed ratio (V_p/V_s) which is an important petrophysical parameter for reservoir monitoring.
- (ii) In the Unaweep Canyon (Colorado, US) study, I image the longitudinal structure of the buried basement and the overlying sedimentary fill. This is done using two independent passive seismic methods, i.e., teleseismic

coda-wave autocorrelation and ambient seismic interferometry, applied to a short duration (1-month) recording. The results show an undulating sedimentary-basement interface buried below a sedimentary column of 200 – 500 m thickness. The over-deepened basement structure revealed by these results suggests the role of glacial carving in the canyon's origin.

- (iii) In Enid (Oklahoma, US), I image the shallow subsurface (< 300 m depth) structure with emphasis on the lateral variation of shear-velocities. The interferometrically derived near-surface model (< 60 m depth) is further constrained by horizontal-to-vertical spectral ratio analysis. Using distributed acoustic sensing (DAS), I model the site-amplification with high lateral resolution. I demonstrate a clear correlation between the near-surface structure and the site amplification. The results can be used for seismic hazard assessment at a sub-kilometer scale which is desirable for urban planning.

6.2 Future work

The feasibility of passive seismic interferometry for shallow subsurface imaging described here, offer the possibilities of many more interesting applications.

The P- and S-wave selection filters defined in Chapter 2 and 3 can be applied to long-term continuous recording to obtain time-lapse variations in reflectivity and V_p/V_s ratio. This can be developed into a passive seismic tool of hydrological and reservoir monitoring. At shorter time scales, micro-seismic activity generated during injection operations can be used to as a body-wave source to passively monitor such operation with minimal latency.

DAS has now developed into a compelling alternative to geophones in borehole and ocean bottom settings. However, its application in urban environments is still challenged. In Chapter 5, my attempt to use DAS recordings is only partially successful. I retrieve coherent virtual source gathers at only a few DAS channels, making the dataset incapable of interferometric imaging. In future studies advance filtering techniques (e.g., FK filtering) can be tested to suppress traffic induced strain and enhance ambient surface wave detection. Future DAS deployment can also take advantage of localized pseudo-passive sources (e.g., railway tracks) for surface wave retrieval.